Future Development of Contrails: Impacts of Increasing Air Traffic and Climate Change

S. Marquart*, M. Ponater, F. Mager, R. Sausen
DLR-Institut für Physik der Atmosphäre, Oberpfaffenhofen, Germany

Keywords: contrails, radiative forcing, aircraft, general circulation model, ECHAM

ABSTRACT: The future development of contrails is investigated by means of a contrail parameterization developed for the ECHAM general circulation model, considering changes in air traffic, aircraft technology, and climate change. Time slice simulations show an increase in both contrail cover and radiative forcing (RF) by roughly a factor of 4 between 1992 and 2050. The simulated contrail cover for 1992 agrees well with respective observations. Some sensitivities, such as the impact of different air traffic inventories, the effect of systematic errors in the model climate, the uncertainty due to short observation periods, and the impact of the daily cycle of air traffic are discussed.

1 INTRODUCTION

The expected increase in air traffic will certainly contribute to an increase in contrail cover. More efficient engines will lead to a colder exhaust gas and will, therefore, also facilitate contrail formation. These effects have already been studied by means of a diagnostic method based on the thermodynamic theory of contrail formation (Sausen et al., 1998; Gierens et al., 1999). Here, we investigate the future development of contrails in a changing background climate by means of a contrail parameterization developed for a general circulation model (GCM). We consider changes in air traffic and propulsion efficiency as well as increasing greenhouse gas concentrations in the atmosphere for the three time slices 1992, 2015, and 2050.

2 METHOD

The GCM contrail parameterization, which is based on the thermodynamic theory of contrail formation, was developed for the ECHAM4.L39(DLR) model (Ponater et al., 2002). Here, we use this parameterization together with an upgraded version of the ECHAM4 longwave radiation scheme (Räisänen, 1998; Marquart and Mayer, 2002), as was also done by Marquart et al. (2003). In contrast to the diagnostic approach of Sausen et al. (1998) the parameterization allows to estimate online, within a self-consistent framework, coverage and optical properties of the contrails as well as the resulting RF. For the future time slice simulations (2015, 2050), changes in background climate (increasing greenhouse gas concentrations, changing sea surface temperatures) are taken into account. In our reference simulation, we use 3D inventories of fuel consumption as a measure of air traffic for all time slices, neglecting the daily cycle of air traffic density (DLR, NASA inventories). The simulated contrail cover is calibrated to satellite observations of Bakan et al. (1994) in a way suggested by Marquart et al. (2003).

3 RECENT CONDITIONS

Contrail cover is determined in the GCM as fractional coverage within each model grid box. Summing up vertically, the total contrail cover is gained as 2D distribution. As an example, Figure 1

* *Corresponding author:* Susanne Marquart, Deutsches Zentrum für Luft- und Raumfahrt, Institut für Physik der Atmosphäre, Oberpfaffenhofen, D-82234 Wessling, Germany. Email: susanne.marquart@dlr.de

shows the annually averaged total contrail cover for 1992. The global distribution of the simulated stratosphere adjusted RF is shown in Figure 2 for January and July, while globally averaged values are given for different seasons in Table 1. Please note that the RF values presented here differ from those given by Ponater et al. (2002; their Fig. 7 and Table 2), because their values were calculated with the original ECHAM4 longwave radiation scheme (i.e., without the upgrade mentioned above).

Figure 1. Annually averaged total contrail cover for the 1992 time slice. Regions for which satellite based

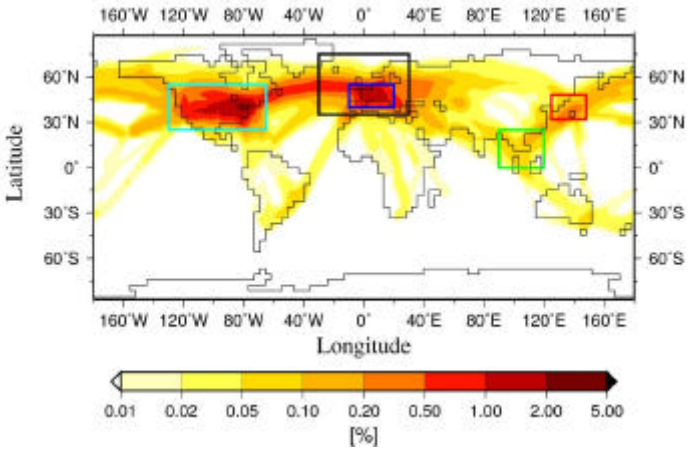

contrail observations exist are marked. Black: Western Europe / East Atlantic (30°W-30°E/35-75°N; Bakan et al., 1994); Dark blue: Western Europe (10°W-20°E/40-55°N; Meyer et al., 2002a); Light blue: USA (130-65°W/25-55°N; Minnis et al., 2000); Red: Japan region (126-148°E/30-48°N; Meyer et al., submitted); Green: Thailand region (90-122°E/0-25°N; Meyer et al., submitted).

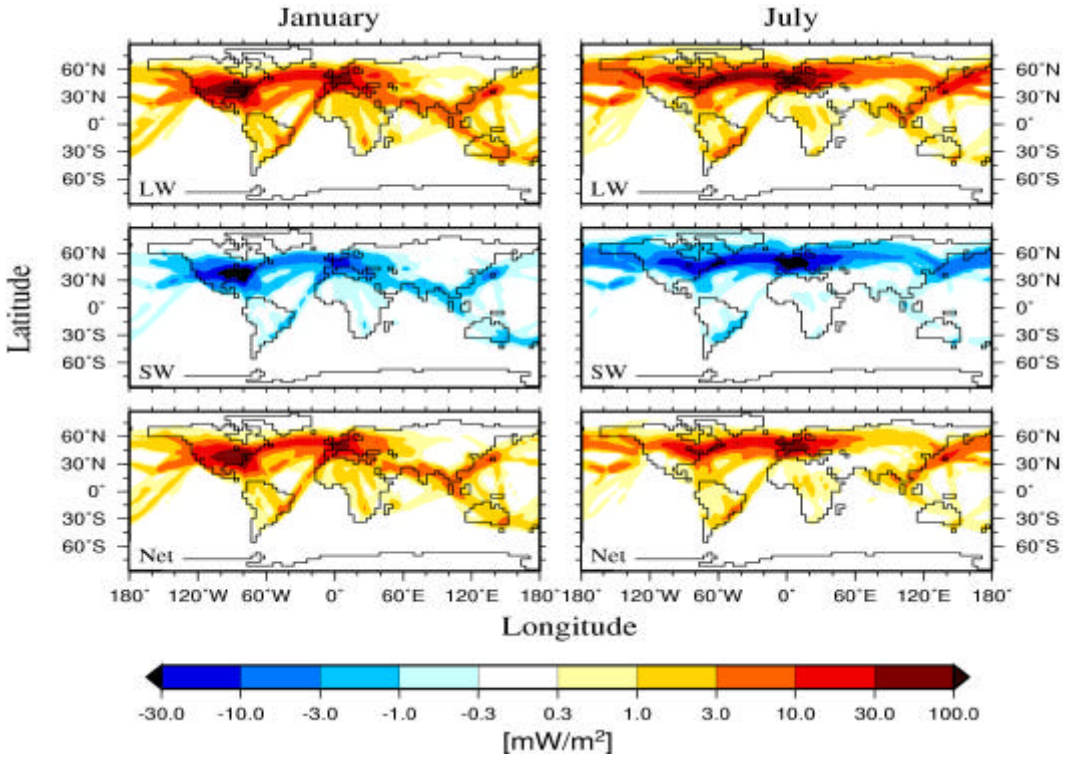

Figure 2. Stratosphere adjusted RF due to contrails for the 1992 time slice.

Table 1. Long term and globally averaged stratosphere adjusted RF due to contrails for 1992. Values in brackets are adjusted by a 25% offset to the longwave contrail RF (see Marquart and Mayer, 2002; Marquart et al., 2003).

RF [mW/m^2]	longwave	shortwave	net
January	3.3 (4.4)	-1.1	2.2 (3.3)
April	4.4 (5.8)	-1.6	2.8 (4.2)
July	2.9 (3.9)	-1.3	1.6 (2.6)
October	4.3 (5.7)	-1-5	2.8 (4.2)
Annual mean	3.7 (4.9)	-1.4	2.3 (3.5)

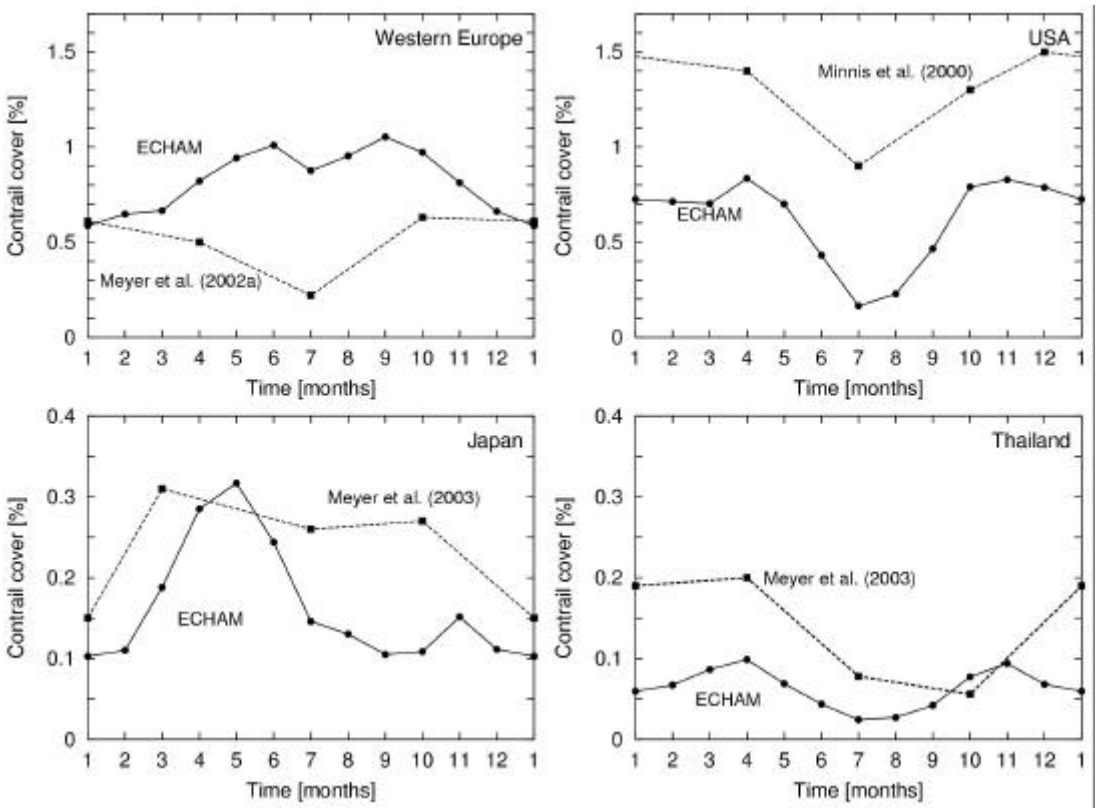

Figure 3. Annual cycle of total contrail cover over different geographical regions according to ECHAM simulations for the time slice 1992 and respective observations.

Figure 3 compares the annual cycle of the simulated total contrail cover to available observations for the geographical regions indicated in Figure 1. For Western Europe, the simulated contrail cover is higher than the observed one, while in the three other areas, the modelled contrail cover is mostly below the observational results. The qualitative annual cycle is quite similar in model and observation over USA and Japan (taking into account that observational data do not exist for all months), whereas in Europe and Thailand, some qualitative discrepancies appear. An obvious reason for the quantitative disagreement is a difference of up to 6 years between simulation and observations (Meyer et al., submitted). Further reasons for the discrepancies, both depending on model uncertainties and on observational deficiencies, are discussed in the next section.

4 SENSITIVITIES

4.1 *Contrail cover*

The regional distribution of contrail cover depends, among others, on the air traffic inventory used. In our 1992 reference case, we use fuel consumption (DLR inventory) as a measure of air traffic, because such inventories are also available for future time slices. The difference (as a ratio) to a simulation using flown distances instead, is shown in Figure 4a: While the contrail cover tends to be

slightly underestimated when using fuel consumption in Europe and USA (where many short-distance flights with small aircraft are performed), it is overestimated in most other regions of the world. The relative overestimation is most pronounced in Southeast Asia. Note, however, that with the recently created TRADEOFF data base, air traffic inventories including flown distances are becoming available also for future time slices (see the contribution of Fichter et al., this issue).

In order to quantify how the contrail cover simulated within the framework of the ECHAM4 GCM is affected by systematic errors in the model climate (e.g., the cold bias in the extra tropical lowermost stratosphere), offline diagnostic calculations using ERA instead of ECHAM4 temperature and humidity data were performed (Marquart et al., 2003). As shown in Figure 4b, the GCM simulated contrail cover tends to be overestimated in high northern latitudes, where the cold bias is most pronounced, whereas it is underestimated in the tropical warm bias regions.

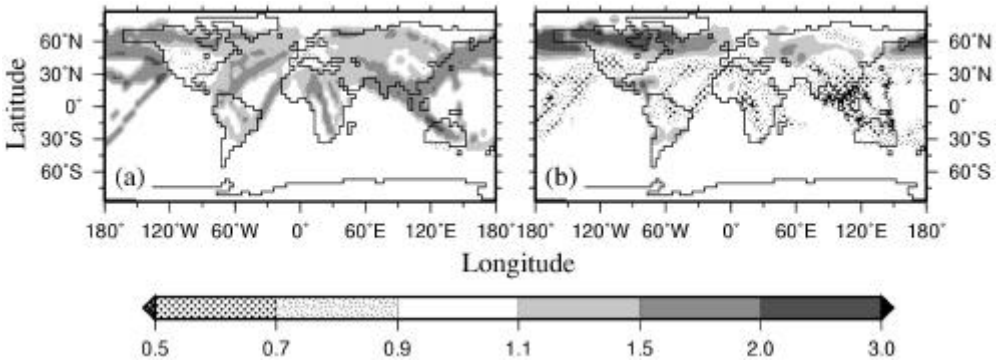

Figure 4. Ratios of total contrail cover between different scenarios for the time slice 1992. (a) Ratio between the reference case and a simulation where flown distances instead of fuel consumption were used; (b) Ratio between the reference case and a calculation where ERA temperature and humidity data instead of ECHAM4 data were used.

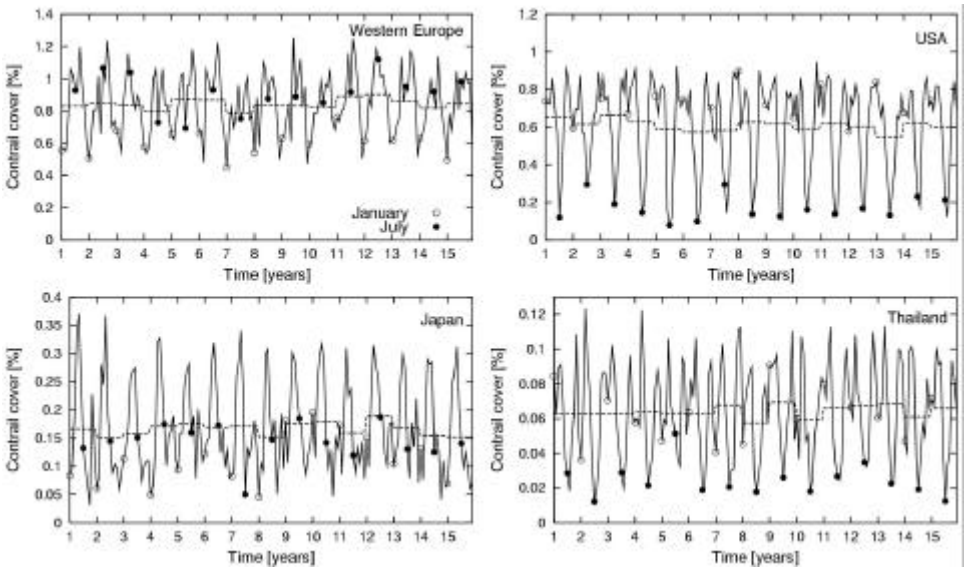

Figure 5. 15-year time series of total contrail cover over different regions according to ECHAM simulations for the time slice 1992. Solid lines: monthly means; dashed lines: annual means; hollow circles: January-means; filled circles: July-means.

The above mentioned contrail observations include maximal 2 years of data (although it has to be mentioned that the observational database for Western Europe was extended to 6 years recently; Meyer et al., 2002b). The mostly insufficient lenght of a 1 or 2 year time span for gaining representative qualitative and quantitative values is indicated in Figure 5, which shows a 15-year

time series of modelled contrail cover. Especially in the Japan and Thailand regions, the simulated year-to-year variability is remarkably large.

4.2 *Radiative forcing*

Although RF shows a number of sensitivities of different kinds, we focus here on the effect of the daily cycle of air traffic density (which is neglected in our reference case) on RF. While the diurnal cycle of longwave RF closely follows the daily cycle of air traffic, the diurnal cycle of shortwave RF additionally depends on the solar zenith angle. If the diurnal cycle is included in a GCM simulation for the 1992 air traffic, the global annual mean net RF decreases by less than 10% compared to our reference simulation. This comparatively small change arises mainly from a qualitatively different behaviour in different regions of the globe (Fig. 6): When the daily cycle is included, the shortwave impact is stronger (and the net RF is, therefore, smaller) in regions with high air traffic density during day, while it is weaker in long-distance flight corridors with the largest part of flights occurring during night. Further sensitivities of the RF results are presented in Marquart et al. (2003).

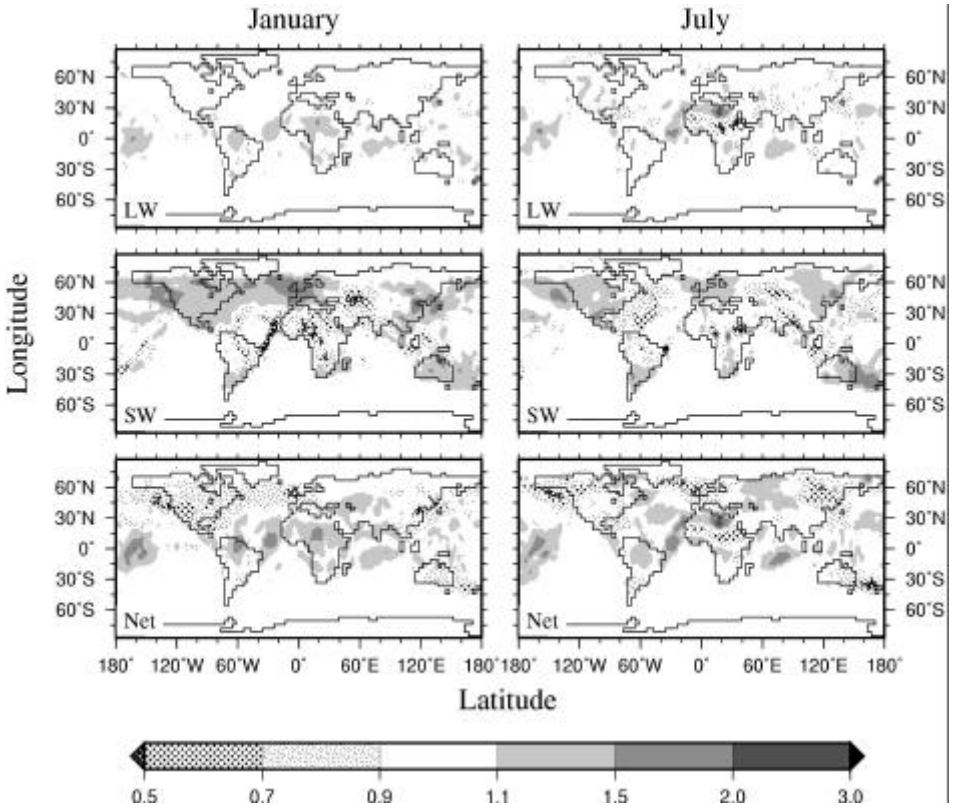

Figure 6. Ratio of longwave, shortwave, and net RF with/without including the daily cycle of air traffic density for the time slice 1992 for January and July.

5 FUTURE PROJECTIONS

The simulated future development of contrails up to the year 2050 is summarized in Table 2 (see also Marquart et al., 2003). Considering changes in air traffic, propulsion efficiency, and climate, contrail net RF increases from 3.5 mW/m^2 in 1992 to 9.4 mW/m^2 in 2015 and 14.8 mW/m^2 in 2050. If only changes in air traffic density are considered, the net RF depends quite linearly on the aviation fuel consumption. Growing propulsion efficiency leads to increases in contrail cover and RF, while climate change tends to reduce them. Optical depth increases slightly in a warmer climate.

Table 2. Annually and globally averaged contrail cover and RF components, as well as global annual fuel consumption in 1992, 2015, and 2050. Values in brackets are adjusted by a 25% offset to the longwave contrail RF (see Marquart and Mayer, 2002; Marquart et al., 2003). Changes in air traffic density, propulsion efficiency (η), and climate change are taken into account.

Year	Fuel [Tg/y]	η	Climate change	Cover [%]	LW RF [mW/m^2]	SW RF [mW/m^2]	Net RF [mW/m^2]
1992	112	**0.3**	-	0.06	3.7 (**4.9**)	**-1.4**	2.3 (**3.5**)
2015	271	0.3	no	0.13	8.6 (11.5)	-3.1	5.5 (8.4)
		0.4	no	0.15	10.1 (13.5)	-3.7	6.4 (9.8)
		0.4	**yes**	**0.14**	9.8 (**13.1**)	**-3.7**	6.1 (**9.4**)
2050	471	0.3	no	0.23	14.7 (19.6)	-5.3	9.4 (14.3)
		0.5	no	0.28	20.2 (26.9)	-7.4	12.8 (19.5)
		0.5	**yes**	**0.22**	15.5 (**20.7**)	**-5.9**	9.6 (**14.8**)

6 CONCLUSIONS

The future development of line-shaped contrails was investigated (as part of the EU project TRADEOFF) considering changes in air traffic, aircraft technology, as well as climate change by means of a contrail parameterization developed for the ECHAM4 GCM. Time slice simulations show an increase in contrail cover and RF by roughly a factor of 4 between 1992 and 2050. The simulated global mean RF is about a factor of 5 lower than the best estimate by IPCC (1999), rendering line-shaped contrails, from a climate change point of view, less important than thought some years ago. Please note, however, that contrail-to-cirrus transition was not included in our investigations. The total effect of air traffic on cirrus coverage will be an important topic in future research.

REFERENCES

Bakan, S., M. Betancor, V. Gayler and H. Graßl, 1994: Contrail frequency over Europe from NOAA-satellite images. *Ann. Geophysicae 12*, 962-968.

Gierens, K. R. Sausen and U. Schumann, 1999: A diagnostic study of the global distribution of contrails, Part II: future air traffic scenarios. *Theor. Appl. Climatol. 63*, 1-9.

IPCC, 1999: *Aviation and the global atmosphere - A special report of IPCC working groups I and III*. Intergovernmental Panel on Climate Change, Cambridge University Press, Cambridge, UK and New York, NY, USA, 365 pp.

Marquart, S. and B. Mayer, 2002: Towards a reliable GCM estimation of contrail radiative forcing. *Geophys. Res. Lett. 29* (8), 1179, DOI 10.1029/2001GL014075.

Marquart, S., M. Ponater, F. Mager and R. Sausen, 2003: Future development of contrail cover, optical depth and radiative forcing: Impacts of increasing air traffic and climate change. *J. Clim. 16*, 2890-2904.

Meyer, R., H. Mannstein, R. Meerkötter, U. Schumann and P. Wendling, 2002a: Regional radiative forcing by line-shaped contrails derived from satellite data. *J. Geophys. Res. 107* (D10), 4104, DOI 10.1029/2001JD000426.

Meyer, R., H. Mannstein, R. Meerkötter and P. Wendling, 2002b: Contrail and cirrus observations over Europe from 6 years of NOAA-AVHRR data, *Proceedings of the Meteorological Satellite Data User's Conference*, EUMETSAT, Dublin, Irland.

Meyer, R., R. Büll, C. Leiter, H. Mannstein, S. Marquart, T. Oki and P. Wendling, 2003: Contrail observations over Southern and Eastern Asia in NOAA/AVHRR data and intercomparison to contrail simulations in a GCM, submitted to *Int. J. Remote Sensing*.

Ponater, M., S. Marquart and R. Sausen, 2002: Contrails in a comprehensive global climate model: parameterisation and radiative forcing results. *J. Geophys. Res. 107* (D13), 4164, DOI 10.1029/2001JD000429.

Räisänen, P., 1998: Effective longwave cloud fraction and maximum-random overlap of clouds: a problem and a solution. *Mon. Wea. Rev. 126*, 3336-3340.

Sausen, R., K. Gierens, M. Ponater and U. Schumann, 1998: A diagnostic study of the global distibution of contrails, Part I: Present day climate. *Theor. Appl. Climatol 61*, 127-141.

A Study of Contrails in a General Circulation Model

A. Guldberg*
Danish Meteorological Institute, Copenhagen, Denmark

Keywords: Contrails, GCM, radiative forcing

ABSTRACT: The IFSHAM model is used for a study of contrails in a general circulation model. The IFSHAM model is a model based on the dynamical core from the ARPEGE-IFS, version 3, model and the physical parameterization package from the ECHAM-5 model. The contrail parameterization scheme of Ponater et al., 2002 has been implemented in the IFSHAM model in order to be able to study contrail formation. The scheme is based on thermodynamic theory and the principles of the models cloud scheme. Results for global contrail cover and radiative forcing are shown and compared with results from the few other model studies that exist and with observed data.

1 INTRODUCTION

In the IPCC special report 'Aviation and the Global Atmosphere', (IPCC, 1999) the estimate of the radiative forcing due to line shaped contrails is 0.02 W m^{-2} for 1992 air traffic conditions. In Ponater et al., 2002 the first parameterization of contrails for use in a general circulation model (GCM) is presented making it possible to estimate the climate impact of contrails from GCM experiments. An advantage of parameterizing contrails in a GCM is that contrail coverage and optical properties are then related to the instantaneous state of the atmosphere. Using this parameterization of contrails in the ECHAM-4 model, (Ponater et al., 2002), together with a modification of the long wave part of the models radiation scheme as described in Marquart and Mayer, 2002, results in an estimate of the radiative forcing due to line shaped contrails being 0.003 W m^{-2} for 1992 air traffic conditions, (Marquart and Mayer, 2002). This estimate is an order of magnitude less than the IPCC, 1999 estimate.

In the present study the contrail parameterization of Ponater et al., 2002 has been implemented in a GCM different from the one used by Ponater et al., 2002 in order to study the model dependency of the scheme. Results for contrail coverage and radiative forcing are shown and compared to the results of Ponater et al., 2002 and Marquart and Mayer, 2002.

2 MODEL AND EXPERIMENTS

The model used in this study is the IFSHAM model developed at the Danish Meteorological Institute by Shuting Yang. The model consists of the dynamical core from the ARPEGE-IFS model, version 3 (a description of an older version of the model can be found in Déqué et al., 1994) – and the physical parameterization package from the ECHAM-5 model (an older version of the model is described in Roeckner et al., 1996)

The IFSHAM model uses semi-lagrangian advection and a two time-level discretization. The cloud scheme is the PCI scheme (Lohmann and Roeckner, 1996), where cloud water and cloud ice are treated as separate prognostic variables. The radiation scheme consists of the Morcrette short wave scheme (Morcrette, 1991) and the RRTM scheme (Mlawer et al., 1997) for the long wave part.

The contrail parameterization scheme of Ponater et al., 2002 has been implemented in the IFSHAM model. Using this parameterization the actual contrail coverage is dependent on the air

* *Corresponding author:* Annette Guldberg, Danish Meteorological Institute, Lyngbyvej 100, DK-2100 Copenhagen, Denmark. Email: ag@dmi.dk

traffic density. The version 2 Deutsches Zentrum für Luft- und Raumfahrt (DLR) aircraft emission data set (Schmitt and Brunner, 1997) represents the air traffic density in the beginning of the 1990s and has been used to calculate the actual contrail coverage from the potential contrail coverage.

The horizontal resolution of the model in the presented experiments is spectral T63 truncation with a linear grid. For the vertical discretization is used hybrid coordinates and 31 vertical levels are used – the same 31 levels as used in the ECMWF Re-analysis Data set ERA-15 (Gibson et al., 1997). The time step used is 30 minutes. The model is run with climatological SST's and the experiments extend 3 annual cycles.

3 RESULTS

Figure 1a shows the geographical distribution of the average total contrail coverage. The global mean is 0.06 % which is somewhat less than the IPCC, 1999 estimate of 0.1 %. The geographical distribution is to a large extend determined by the main flight routes and have large maxima over central Europe and the eastern United States.

Figure 1b shows the contrail coverage at model level 11 corresponding to approximately 250 hPa and figure 1c the contrail coverage at model level 10 corresponding to approximately 220 hPa. It is seen that the contrail coverage over Europe and eastern United States is larger at 250 hPa than at 220 hPa, partly due higher air traffic density.

Figure 2a shows the instantaneous short wave radiative forcing at the top of the atmosphere (TOA) due to contrails averaged over the 3 simulated years. As expected the short wave forcing due to contrails is negative and has the largest values (numerically) over Europe and eastern United States where also the contrail coverage is largest. The geographical distribution and the global mean value of the short wave forcing – -1.4 mW m^{-2} – fits well the results obtained in Ponater et al., 2002.

Figure 2b shows the instantaneous long wave radiative forcing at TOA due to contrails. The long wave forcing is positive everywhere except for areas in the tropics. The geographical distribution is similar (except for the areas with negative values) to the results obtained in Ponater et al., 2002, but the values (as eg. reflected in a global mean of 1.5 mW m^{-2}) are small.

The negative values of the long wave forcing in the tropics are unexpected and an explanation needs to be found. To investigate this an experiment was made where only contrails – no natural clouds – were present in the call to the radiation scheme, meaning that the radiative forcing of contrails with no natural clouds present was determined. In this experiment the negative areas disappeared and the long wave forcing due to contrails were positive everywhere. This suggests that the negative values in figure 2b are due to cloud overlap problems.

Figure 2c shows the instantaneous net radiative forcing at TOA due to contrails. Positive net forcing is seen over the Atlantic and Pacific Oceans, over eastern United States, eastern Asia and Australia , whereas negative net forcing is seen over most of Europe, western United States and in many areas in the tropics. The global mean of the net radiative forcing – 0.09 mW m^{-2} – is small compared to the 3.2 mW m^{-2} estimated by Marquart and Mayer, 2002 and indeed small compared to the IPCC, 1999 estimate of 20 mW m^{-2}.

In the experiment where the radiative forcing due to contrails without natural clouds present is determined is the pattern of the net radiative forcing somewhat different: the areas with negative values in the tropics have disappeared, but now the net radiative forcing is negative almost everywhere on the northern hemisphere and the global mean of the net radiative forcing is negative: -0.7 mW m^{-2}.

A third experiment was performed in which the contrail coverage was increased having a global mean of 0.15 % (as compared to the experiment shown in figure 1a where the global mean is 0.06 %). The values of the short wave forcing and the long wave forcing are increased and the global means are more than doubled. The global mean of the short wave forcing is now -3.7 mW m^{-2} (compared to -1.4 mW m^{-2} in the experiment shown if figure 2a). The global mean of the long wave forcing due to contrails is 3.9 mW m^{-2} in the third experiment (compared to 1.5 mW m^{-2} in the experiment shown in figure 2b). But the net radiative forcing does not change that much: the global mean of the net radiative forcing in the third experiment is 0.14 mW m^{-2} (compared to 0.09 mW m^{-2} in the experiment shown in figure 2c) and the geographical distribution of the net radiative forcing

in the third experiment is almost identical to the geographical distribution of the first experiment, shown in figure 2c.

4 DISCUSSION

The contrail coverage obtained in the first experiment described and shown in figure 1 is in reasonable agreement with the contrail coverage obtained by Ponater et al., 2002, but the net radiative forcing shown in figure 2c is small and the geographical distribution showing areas with relatively large negative values is not in agreement with results obtained in other studies and an explanation needs to be found.

The geographical distribution of the net radiative forcing obtained in Ponater et al., 2002 also contains areas with negative values especially at the northern-most latitudes. But as explained in Marquart and Mayer, 2002 this is due to a problem of the long wave radiation scheme in ECHAM-4. The combination of the effective emissivity approach and the maximum-random cloud overlap assumption leads to a considerable underestimation of the long wave radiative forcing of the optically thin contrails. When modifying the long wave scheme as described in Marquart and Mayer, 2002 the contrail long wave forcing is increased and the net radiative forcing does not contain areas with negative values.

The long wave scheme (the RRTM scheme) used in the IFSHAM model is different from the long wave scheme used in ECHAM-4. The RRTM scheme does not use the effective emissivity approach, but uses true cloud cover and emissivity separately. Therefore the problem described in Marquart and Mayer, 2002 is not present in the IFSHAM model, but there could still be a problem in the way optically thin clouds are treated in the long wave scheme. This remains to be investigated.

Compared to the Ponater et al., 2002 study the contrail effective radii and the ice water path of this study is a smaller and the impact of this has to be determined in future experiments.

ACKNOWLEDGMENT

Many helpful discussions with Michael Ponater and Susanne Marquart are gratefully acknowlegded.

REFERENCES

Déqué, M., C. Dreveton, A. Braun, and D. Cariolle, 1994: The ARPEGE-IFS atmosphere model: a contribution to the French community climate modelling. *Clim. Dyn. 10*, 249-266

Gibson, J. K., P. Kållberg, S. Uppala, A. Hernandez, A. Nomura, and E. Serrano, 1997: ERA-15 Description. *ECMWF Re-analysis Project Report Series, 1*

IPCC, 1999: Aviation and the Global Atmosphere [Penner, J. E. et al. (eds)]. *Cambridge University Press*, Cambridge, New York, USA, 370 pp

Lohmann, U. and E. Roeckner, 1996: Design and performance of a new cloud microphysics scheme developed for the ECHAM general circulation model. *Clim. Dyn. 12*, 557-572

Marquart, S. and B. Mayer, 2002: Towards a reliable estimation of contrail radiative forcing. *Geophys. Res. Lett. 29 (8)*, 1179, doi:10.1029/2001GL014075, 20-1–20-4

Mlawer, E. J., S. J. Taubman, P. D. Brown, M. J. Iacono, and S. A. Clough, 1997: Radiative transfer for inhomogeneous atmospheres: RRTM, a validated correlated-k model for the longwave. *J. Geophys. Res. 102 (D14)*, 16,663-16,682

Morcrette, J-J., 1991: Radiation and cloud radiative properties in the European Centre for Medium Range Weather Forecasts forecasting system. *J. Geophys. Res. 96*, 9121-9132

Ponater, M., S. Marquart, and R. Sausen, 2002: Contrails in a comprehensive global climate model: Parameterization and radiative forcing results. *J. Geophys. Res. 107 (D13)*, 4164, doi:10.1029/2001JD000429, ACL 2-1–2-15

Roeckner, E., K. Arpe, L. Bengtsson, M. Christoph, M. Claussen, L. Dümenil, M. Esch, M. Giorgetta, U. Schlese, and U. Schulzweida, 1996: The atmospheric general circulation model ECHAM-4: Model description and simulation of present-day climate. *Max-Planck-Inst. Meteorol. Rep. 218*, Hamburg, Germany, 90 pp

Schmitt, A. and B. Brunner, 1997: Emissions from aviation and their development over time. In: *Pollutants From Air Traffic – Results of Atmospheric Research 1992-1997* [Schumann, U. et al. (eds)], DLR-Forschungsber. 97-04, Dtsch. Zentrum für Luft- und Raumfahrt, Cologne, Germany, 27-52

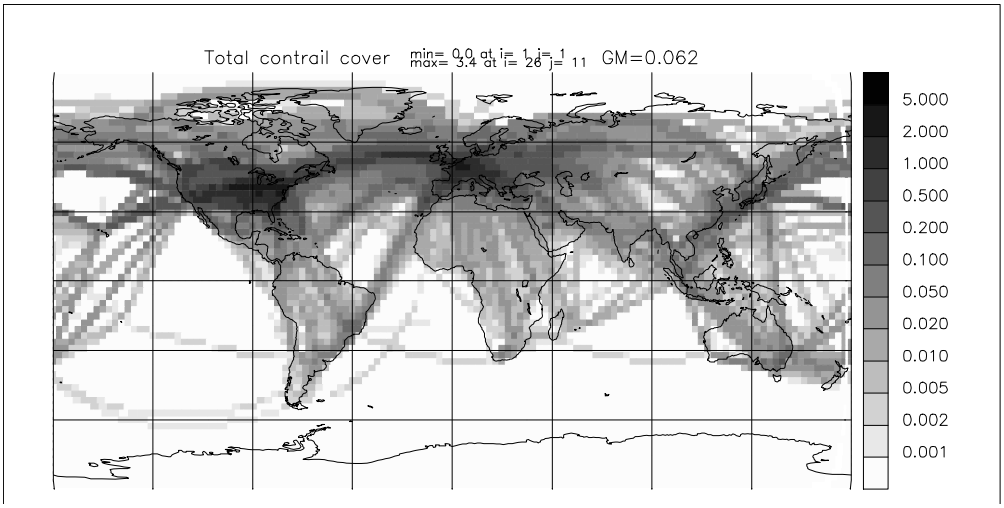

Figure 1a. Total contrail cover. Unit: %. Global mean 0.06 %

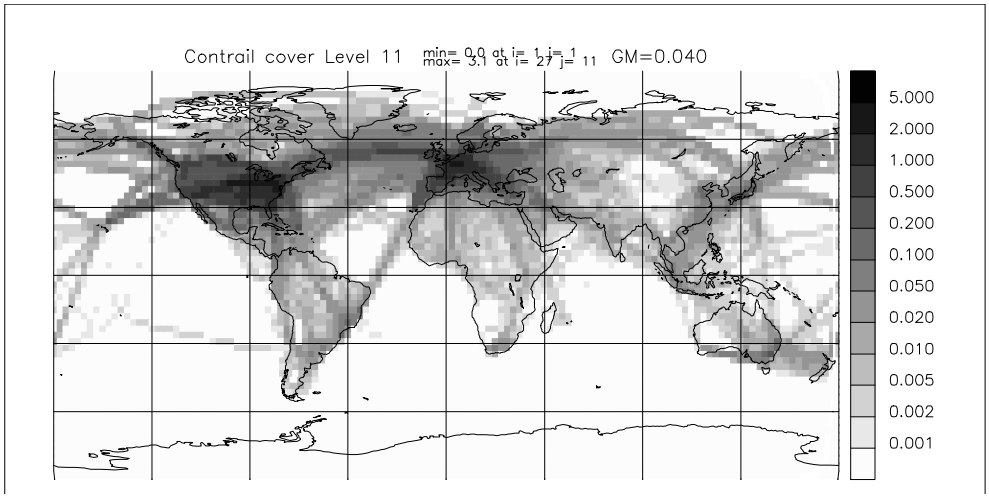

Figure 1b. Contrail cover at model level 11, corresponding to approximately 250 hPa. Unit: %

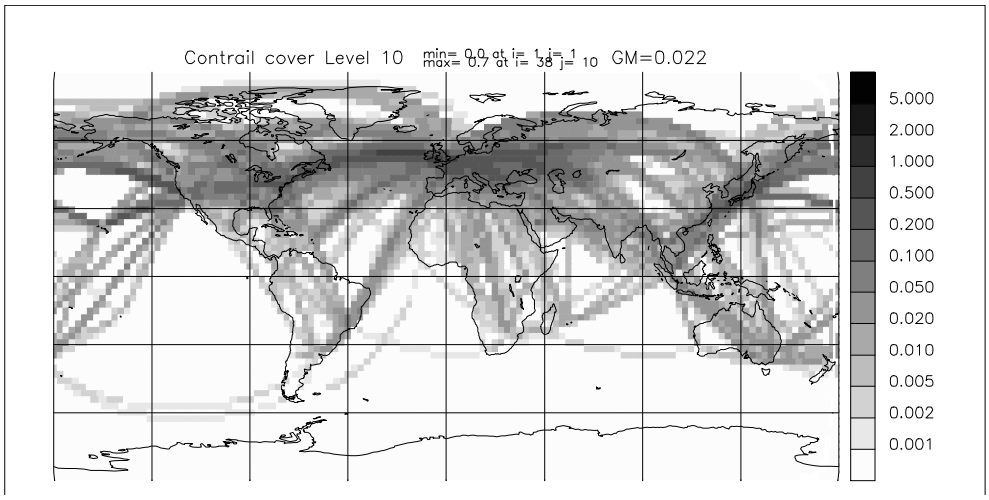

Figure 1c. Contrail cover at model level 10, corresponding to approximately 220 hPa. Unit: %

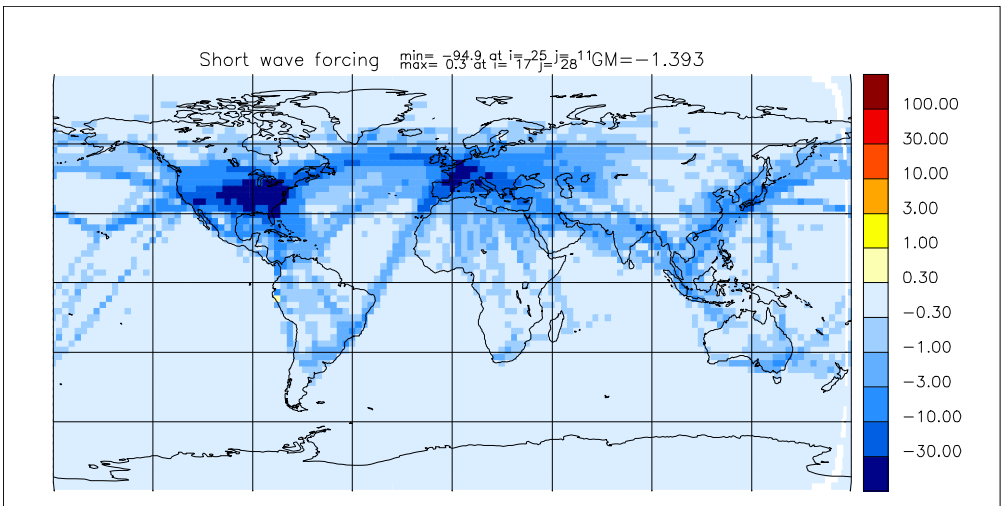

Figure 2a. Instantaneous short wave radiative forcing at TOA due to contrails. Unit: mW m^{-2}

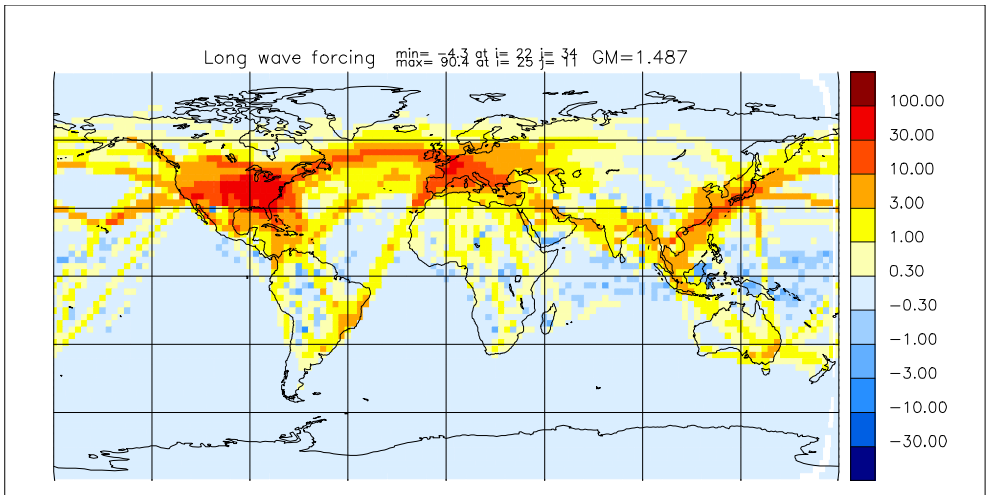

Figure 2b. Instantaneous long wave radiative forcing at TOA due to contrails. Unit: mW m^{-2}

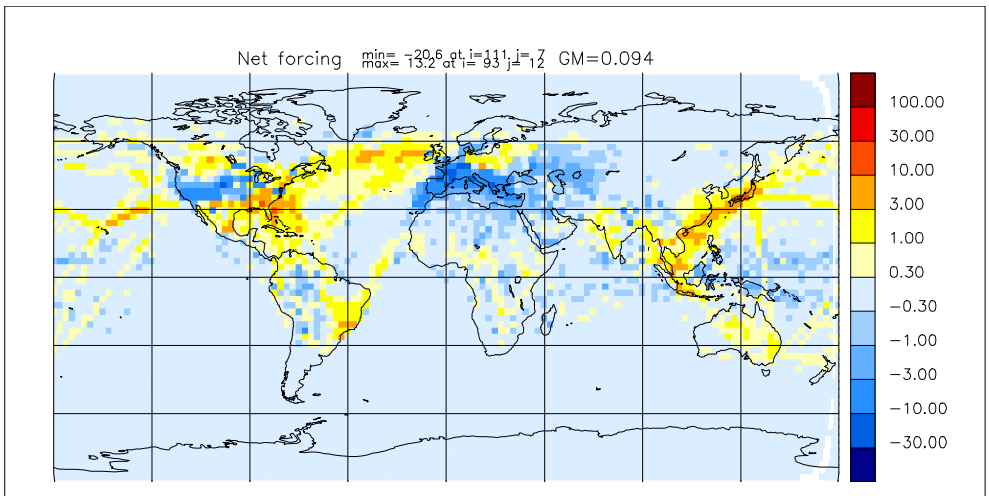

Figure 2c. Instantaneous net radiative forcing at TOA due to contrails. Unit: mW m^{-2}.

Hygroscopicity and wetting of aircraft engine soot and its surrogates: CCN/IN formation in UT

O.B.Popovicheva*, N.M.Persiantseva, E.E. Lukhovitskaya
Institute of Nuclear Physics, Moscow State University, Moscow, Russia

N.K.Shonija, Zubareva N.A.
Chemical Department, Moscow State University, Moscow, Russia

J. Suzanne, D.Ferry, B.Demirdjian
CRMC2-CNRS, Campus de Luminy, Marseille, France

Keywords: engine soot, ice nucleation, contrails, cirrus clouds

ABSTRACT: Aircraft engine soot is characterized in respect to physico – chemical properties responsible for CCN formation. It demonstrates the surprisely high hydrophilicity at the threshold contrail conditions that allows to estimate the water supersaturations needed for the ice nuclei formation in the plume. Sulfur-free aircraft combustor and kerosene flame soots are believed to represent the insoluble surrogates of BC in the UT. Soot agglomerated structure is suggested to amplify the heterogeneous cirrus cloud formation due to the inverse Kelvin effect in the ice-supersaturated regions of the UT.

1 INTRODUCTION

Formation of visible contrails in the UT is the most obvious effect of the aircraft emission into the atmosphere. Aircraft near-field observations confirm that non-volatile aerosols of the jet exhaust consist mainly of black carbon (BC) particles responsible for contrail formation (Petzold et al.,1998; Karcher et al.,1996). But the aircraft exhaust may also impact indirectly on the climate if exhaust particles act as ice nuclei (IN). In this context, antropogeneous ice nucleating aerosols in the UT have a special significance because they may allow ice nucleation at lower supersaturations that those required for homogeneous freezing, resulting in an increase of the area coverage of the cirrus clouds and changing its microphysics properties. Analysis of ice residuals taken in cirrus clouds showed that they are dominated by carbonaceous particles (Chen et al., 1998). However, there is considerable uncertainty regarding the quantitative estimate of the ice-nucleating ability of soot aerosols in the UT because 1) *in situ* measurements of ice nucleation are difficult, 2) laboratory studies of combustion soots show a surprising variation in their nucleation properties (Lamel and Novakov, 1995; Diehl and Mitra, 1998), and 3) the surface physical and chemical requirements for IN are complex and poorly understood.

Incorporation of soot aerosols into cloud particles depends on the wettability of their surface. Literature on wettability of BC yields a consistent picture of hydrophobicity. It means a nonzero water droplet contact angle which is traditionally associated with poor ability to adsorb water and high supersaturation needed for condensation growth. Lack of experimental data about the aircraft – generated soot properties led to assumption about its initial hydrophobicity and necessity for soot activation by sulphuric acid coating (Karcher et al.,1996). However, recent measurements of the water adsorption on soot produced by burning the sulfur – free fuel in the aircraft combustor showed (Popovicheva et al., 2000) that due to the microporous structure and chemical heterogeneity , such soot aerosols can acquire a substantial fraction of a water monolayer at the conditions of the young plume (Popovicheva et al., 2001). Laboratory-made soot surrogates produced by aviation fuel burning contain the reduced amount of soluble (Hallet et al., 1989) but may act as ice nuclei at low temperatures (Diehl and Mitra, 1998; Ferry et al.,2002). Moreover, the hygroscopic behaviour of jet

* *Corresponding author:* Olga B. Popovicheva, Institute of Nuclear Physics, Moscow State University, 119 992, Moscow, Russia. Email: polga@mics. msu.su

engine soot (Hagen et al., 1992; Gysel et al., 2003) allow to assume their significant potential for CCN formation which is commonly attributed to sulphuric acid adsorbed on the soot surface.

This is why the comprehensive laboratory studies of hydration properties of original engine soot and its surrogates are extremely needed with purpose to clarify the mechanism of water adsorption and ice nucleation responsible for the soot – induced contrail and cirrus formation in the UT.

This paper is devoted to hydration and wetting properties of engine soot connected with its composition, solubility, and surface chemistry. Complementary studies of laboratory – made kerosene soots identify the specific features of soot surrogates for atmospheric researches. Knowledge about nature of water/soot interaction allow suggest the possible pathway of CCN/IN formation in the UT.

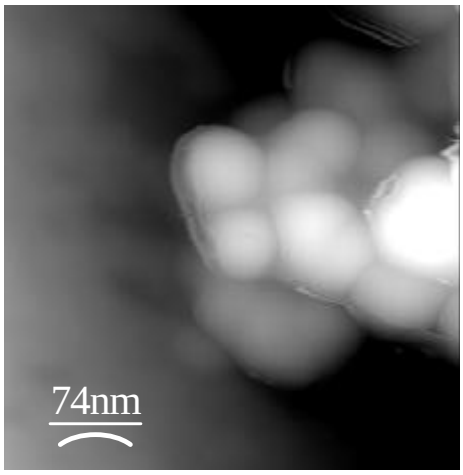

Figure 1. AFM image of engine soot

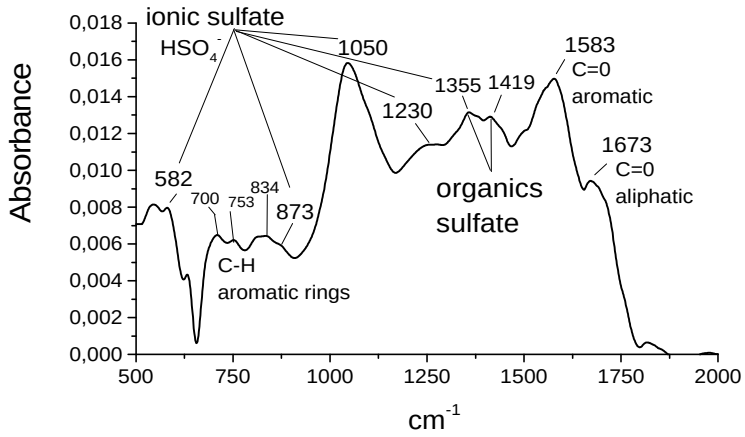

Figure 2. FTIR spectra of engine soot

2 AIRCRAFT ENGINE SOOT. PHYSICO-CHEMICAL PROPERTIES

The combustion chamber of a gas turbine engine D36KU has been used for engine soot production on the background facilities in CIAM, Moscow. The soot samples were collected at the combustor exit at the cruise combustion conditions using aviation kerosene TC1 containing 0.25 wt% of sulfur.

Atomic Force Microscopy (AFM) analysis of engine soot showed that it consists of the roughly spherical primary particles which are fused and well agglomerated (Fig.1). Transmission Electron Microscopy (TEM) analysis coupled by diffraction analysis demonstrated the amorphous microstructure of most part of soot and found well – crystallised particles accosiated either with graphite or chemical impurities. Particles with a mean diameters of 30 and 100 nm were found. Probably, the fused particles of the small micro and mesoporosity provide a low surface area which was obtained by a single point BET techniques in the range from 9 to 30 m^2/g.

X-ray energy analysis (XREDS) coupled to TEM was used to examined the chemical composition of amorphous soot particles which was found to consist mainly of from carbon C~98 wt%, oxygen O~1.6 wt% and sulfur S~0.2 wt% (main fraction). Surprisingly high amount of chemical impurities was observed in the well- crystallized soot particles (fraction of impurities). They contain a large amount of Fe ~30 wt%, O~10 wt%, K~1.25 wt%, and Mn ~0.22 wt%, which are associated with the increased amount of S~2 wt%. Small amount (less then 0.05 wt%) of other elements like Si, Mg, B, Ca, and Cu was detected by emission spectroscopy. Variation of composition and large amount of impurities allow to suggest the high heterogeneity of the soot particle fractions in respect to its hygroscopoicity. Finding of Fe and S in engine soot is correlated with composition measurements of ice residual particles in contrails (Petsold, et al. 1998).

Infrared spectroscopy allows to analysis the chemical nature of the soot surface and identify the functional groups which may be directly responsible for the interaction with water. FTIR spectra of engine soot is shown in Figure 2. The underlying absorption of the carbon skeleton, -C-C- and –C=C- groups, results in a broad combination of bands between 1000 and 1600 cm^{-1}. Peaks at 1673 and 1583 cm^{-1} due to vibrations of the carbonyl C=O groups in aliphatic and aromatic structures are

known as the most active sites for the water adsorption. Weak bands around 3500 cm^{-1}, the region of hydroxyls O-H, does not allow to suggest the existence of carboxyl groups. Intensive peaks at 700, 753, 834, and 873 cm^{-1} joint with oscillation of C-H groups in substituted aromatics which may act as the most hydrophobic sites on the soot surface. But the most distinctive feature of engine soot is a set of peaks at 1355, 1230, 1050, 878 and 582 cm^{-1} connected to vibrations of HSO_4^- ion. Moreover, the prominent region between 1350 and 1420 cm^{-1} is attributed by organics sulfates. It indicates that sulfur on the engine soot surface appears in derivatives of the sulphuric acid and may produce the strong active sites for the water adsorption. Therefore the assumption about the soot coverage by H_2SO_4 may be considered only as the simplest model of engine soot.

FTIR spectra of washed soot demonstrated the dramatic decrease of ionic and organics sulfur bands with small change of other functional groups. Ion chromatography analysis showed an ionic composition of the extracted water soluble compounds which is dominated by SO_4^{2-} ~3.5 wt% as well as Cl^-, CH_3COO^-,$C_2H_4^-$, and NO_3^-.Total amount of water soluble fraction (WSF) was estimated to be more 5 wt%. Volatile compound fraction (VCF) ~17 wt % was measured after heating at 300C for 30 min , that gives the estimation for the amount of volatile organics following the assumption of Ohta and Okita,1984.

3 HYDRATION OF ENGINE SOOT AND CONTRAIL FORMATION

Gravimetrical measurements of the water adsorption provide a direct demonstration of the engine soot hygroscopicity. Figure 3 shows the amount of water molecules adsorbed per unit surface, $N(H_2O)$, versus the relative pressure, p/p_0, at T=295K and 240K. Engine soot features surprisingly high level of hydrophilicity because it is covered by a statistic water monolayer (1ML ≈ 10 H_2O per nm^2) already at $p/p_0 \cong 10^{-2}$. Such behaviour corresponds to adsorption on initial strong active sites which are connected to the high concentration of ionic and organics sulfates on the soot surface.

Water adsorption on engine soot is increased with decrease of temperature and at the plume saturation conditions T ≅ 240K, soot adsorbs more than 20 ML. Such wettable surface may allow the spherical soot particles to grow water droplets large enough to overcome the Kelvin barrier . Water supersaturations S_w needed for the droplet growth may be obtained using the standard Koehler theory for partially soluble particles. It is found to be ≅ 4.6% and 0.08% for the particles of radius 20 and 50 nm, correspondingly, if to assume the average WSF of 5 wt% over all soot exhaust. It may be less for the most hydrophilic fraction of impurities containing much sulfur and higher for the more hydrophobic main fraction of soot particles. Since the maximum water supersaturations in the plume may reach 60% (Karcher et al,1994) we may be concluded that the hygroscopic aircraft – generated aerosols may easily nucleate water and form ice particles in the cooled plume to fulfil the visibility criteria of the contrail formation.

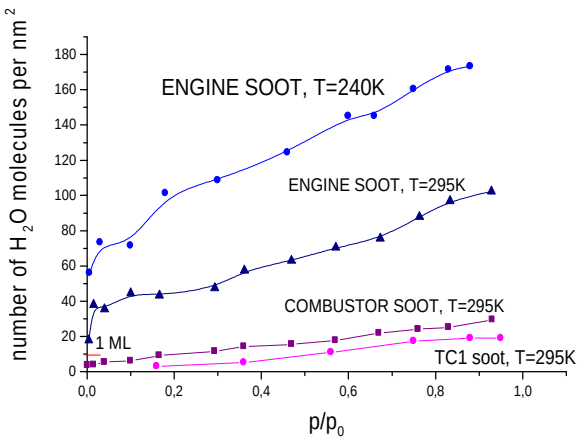

Figure 3. Water adsorption on soots

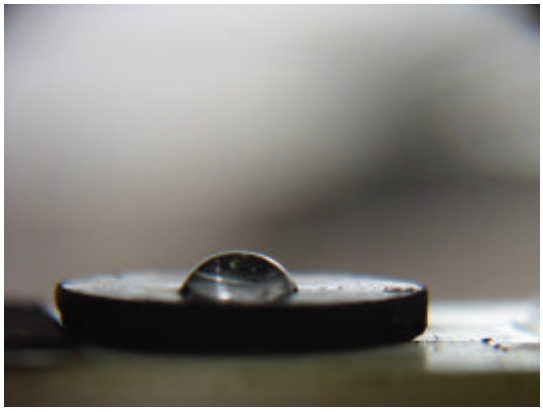

Figure 4. Water droplet on kerosene soot

4 SOOT SURROGATES FOR ATMOSPHERIC BC PARTICLES.

The analysis of the contrail threshold conditions at different fuel sulfur content suggested that soot may take up water even at zero sulfur amount (Karcher et al., 1996). It means that insoluble sulfur – free part of aircraft – generated soot may participate in the contrail formation. Moreover, BC particles coated with sulphuric acid were not found in large ice residual particles from contrails (Twohy and Gandrud, 1998) and sulfur was not observed in the ice residuals of cirrus clouds and interstitial aerosols (Petzold et al.,1998). It means that there is a sulfur-independent pathway of IN formation on the insoluble soot particles which is probably the most widely-distributed in the UT.

To determine the possible mechanism of ice formation on insoluble BC particles, sulfur-free combustor and kerosene flame soots were chosen as available surrogates. Kerosene flame soots were produced by burning the different aviation kerosenes in a lamp burner at the laboratory conditions. TEM analysis showed that there is a remarkable similarity in the roughly spherical shape of the primary particles between combustor, kerosene flame and engine soots. But the typical radius of primary surrogate soot particles was found to be near 20-50 nm (Ferry et al.,2002), no bigger particles were observed. Higher surface area in the range from 40 to 87 m^2/g is appeared as the important characteristics of combustor and kerosene soots beeing in correlation with the significant microporosity of these soots.

The most prominent feature which differentiates laboratory-made surrogates from engine soot are the fractions of water-soluble and volatile compounds. In kerosene soots the WSF was found to be 0.3 wt% and only 0.0015 wt% is related with SO_4^- ion mass . The VCF was found near 1wt% including 0.6% of water. Such insoluble soot particles adsorb water at least one order of magnitude less than engine soot (see Fig.3). In the initial p/p_0 region the amount of water adsorbed is small that is related with reduced concentration the surface oxygen-containing groups that was confirmed by FTIR. Formation of water clusters and micropore filling is a possible mechanism of the increased adsorption at the $p/p_0 > 0.6$. At the highest relative pressures, adsorption may be connected with the capillary condensation in the meso- and macropores which take place in the interparticle cavities and may be filled by water due to the Kelvin effect.

Low hygroscopicity of surrogate soots is correlated with their low wettability. The contact angles for water/ice droplets on the soot surfaces were measured by classic technique of sessile drop measurements. The image of the water droplet on kerosene soot pillet is shown in Figure 4. Contact angles,?, were found in a range from 70 up 80^0 for kerosene soots, and 63 degree for combustor soot. Absence of temperature dependence for contact angles under freezing was obtained.

5 ICE NUCLEATION ON INSOLUBLE BC PARTICLES AND CIRRUS FORMATION

Enhancement of the heterogeneous nucleation rate on the diesel soot in comparison with predicted by the Fletcher theory has been found in Chen et al.,1993. If to follow the Fletcher theory and assume the formation of critical embryous on isolated soot spherical particles, then the results of Chen et al., 1993 may be explained by the perfect wetting of the diesel soot surface (Kelvin activation), in despite of a fact that the water contact angle on this soot was being obtained $\cong 40^0$.

Our finding for kerosene soots as well as the studies of soot aerosols encountered in the UT show that they exist as the typical chain agglomerates of primary particles of radius 20-50 nm. Favorite condensation in the interparticle cavities of such soot agglomerates may arises a lower critical supersaturation in comparison with the Fletcher theory due to formation of water meniscus of the negative curvature as it is shown in Figure 5. QENS studies of water dynamics on kerosene soot (Ferry et al., 2002) showed that at T=220K and subsaturation conditions near 25 % of adsorbed water may exist as liquid – like water in supermicropores of 2 nm and 35 % transform into ice in soot mesopores and on the external surface. It means that ice nucleation will start in the interparticle cavities ˜ 2 nm from a small amount of present liquid water. At the significant filling of mesopores the size of water meniscus is increased, the effect of confined water became to be negligible and water should freeze. With further increasing of the humidity the curvature become to be positive and finally reaches its maximum. This point corresponds the unstable state and means that any further increase in the relative humidity above the critical supersaturation results in the unconstrained condensation growth of particles (Orr et al.,1975).

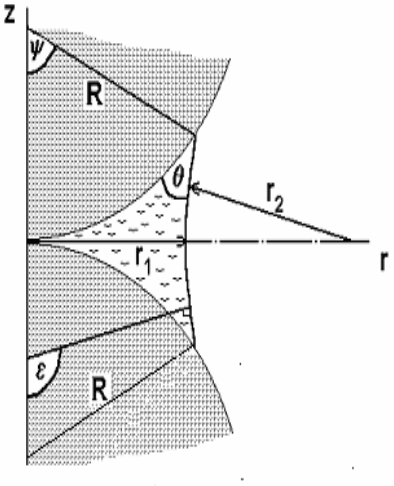

Figure 5. Water condensation between particles

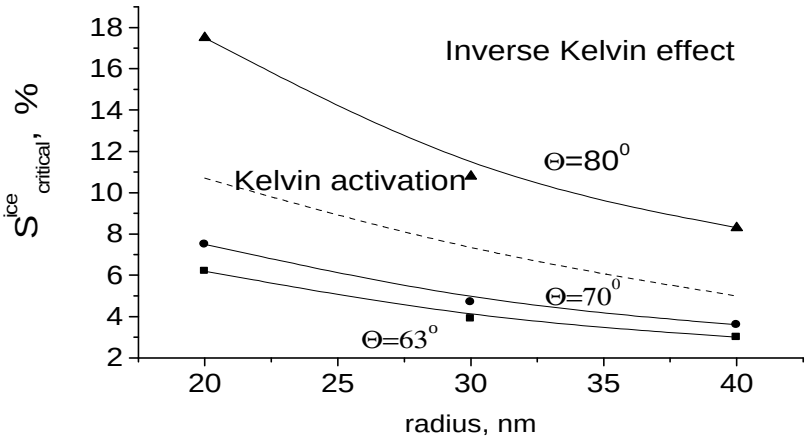

Figure 6. Ice supersaturation on soot particles

Figure 6 presents the critical supersaturation in respect to ice, S_i, at T=220K assuming the inverse Kelvin effect for ice nucleation on soot agglomerates characterised by contact angles $\theta \cong 63^0$, 70^0, and 80^0. Kelvin activation describing the equilibrium supersaturation on totally wettable spherical particles is more efficient than the inverse Kelvin effect on soot of contact angle $\cong 73^0$.

The obtained data demonstrates that if the critical ice supersaturation in the UT may reach ≈ 5%, then the more hydrophilic insoluble soot particles characterized by $\theta \cong 63^0$ may act as cirrus cloud condensation nuclei. At the $S_i \approx 17.5\%$ the most hydrophobic BC particles with $\theta \cong 80^0$ will be activated. In situ observations show that in the UT there is a large supersaturation range in which heterogeneous nuclei may lead to the cirrus formation before atmospheric particles freeze homogeneously. Troposphere water vapor measurements demonstrate that the supersaturation with respect to ice is common in the UT (frequencies of about 30%) , with maximum as high as 73% (Vay et al.,2000). So, insoluble BC particles represented by laboratory soot surrogates in this study may amplify the heterogeneous nucleation in the UT.

6 CONCLUSION

More then 10 experimental techniques were applied to characterized the physico - chemical properties of aircraft engine soot and its surrogates. High level of engine soot hygroscopicity is found to relate to sulfur content originated from the combustion, thus implying a significant role in the contrail formation. Sulfur-free combustor soot and laboratory made kerosene soots are more hydrophobic than engine soot. They are believed to represent the insoluble part of the aircraft-generated soot in the atmosphere. Following their hydration mechanism the inverse Kelvin effect may be assumed for the condensation process into interparticles cavities of the soot agglomerates. In ice supersaturated atmosphere such insoluble BC particles may amplify the heterogeneous ice nucleation process of cirrus clouds. This effect may dominate in the contrail formation process if the water-soluble fraction of the exhaust is relatively small, probably at low sulphur content.

7 ACKNOWLEGEMENTS

Russian authors thanks to INTAS Program, project 00-0460 and CRDF, project RC1-2327-MO-02 for financial support.

REFERENCES

Chen, C.-C., Hung, L-C. and H.-K. Hsu, 1993: Heterogeneous nucleation of water vapor on particles of SiO_2, Al_2O_3, TiO_2, and carbon black. J. *Colloid Interface Sci. 157*,465-477.

Chen, Y., Kreidenweis, S.M. 1998. Single particle analyses of ice nucleating aerosols in the upper troposphere and lower stratosphere. Geophys. Res. Lett. 25,1391.

Diehl,K. and S.K. Mitra ,1998: A laboratory study of the effects of a kerosene-burner exhaust on ice nucleation and the evaporation rate of ice crystals. *Atmosp.Environ. 32*, 3145-3151

Ferry, D., Suzanne, J., Popovicheva, O.B. and N.K. Shonija, 2002: Water adsorption and dynamics on kerosene soot under atmospheric conditions. *J. Geophys. Res. 107*, 4734-4744.

Gysel M., Nyeki,S., Weingartner, E., Baltensperger, U., Giebl H., Hitzenberger, R., Petzold, A., and C.Wilson, 2003: Properties of jet engine combustion particles during the PartEmis experiment; Hygroscopicity at subsaturated conditions. *Geophys. Res. Lett., 30*, 1566-1570.

Hagen, D.E., Trueblood, M.B. and P.D. Whitefield, 1992: A field sampling of jet exhaust aerosols. *Partic. Sci. Tech. 10*, 53-63

Hallet, J., Hudson J.G. and Rogers C.F. ,1989: Characterization of combustion aerosols for haze and cloud formation. *Aeros. Sci. Tech. 10*, 70-83.

Karcher 1994: Transport of exhaust products in the near trail of a jet engine under atmospheric conditions. *J. Geophys. Res.,99*, 14509-14512.

Karcher, B., Peter, Th., Biermann U.M. and U.Schumann, 1996: The initial composition of jet condensation trails. J. *Atmos. Science 53*, 3066-3075

Lamel, S. and P.Novakov, 1995: Water nucleation properties of carbon black and diesel soot particles. *Atmosp. Environ*. 29, 813-823.

Ohta, S. and T. Okita, 1984: Measurements of particulate carbon in urban and marine air in japanese areas. *Atmos. Environ. 18*, 2423-2429.

Orr, F.M., Scriven L.E., and A.P. Rivas, 1975: Pendular rings between solids: meniscus properties and capillary force. *J. Fluid Mech. 67*, 723-733.

Petzold, A., Strom, J., Ohlsson,S. and F.P.Schroder, 1998: Elemental composition and morphology of ice-crystal residual particles in cirrus clouds and contrails. *Atmos. Research*. *49*, 21-34

Popovicheva, O.B., Persiantseva N.M. , Trukhin, M.E. , Shonija, N.K. , Starik, A.M. , Suzanne J. , Ferry D. and B. Demirdjian, 2000: Experimental characterization of aircraft combustion soot : microstructure, surface area, porosity, and adsorption. *Phys. Chem. Chem. Phys*. *2*, 4421-4426.

Popovicheva, O.B., Trukhin M.E., Persiantseva, N.M. and N.K. Shonija, ,2001: Water adsorption on aircraft – combustor soot under young plume conditions. *Atmos. Environ. 35*, 1643-1676.

Twohy, C.H. and B.W. Gandrud, 1998: Electron microscope analysis of residual particles from aircraft contrails. *Geophys. Res. Lett. 25*, 1359-1362

Vay, S.A., Anderson, B.E., Jensen E.J., Sachse, G.W., Ovarlez,J., Gregory,G.L., Nolf, S.R., and C.E. Sorenson, 2000 : Tropospheric water vapor measurements over the North Atlantic during the subsonic assessment ozone and nitrogen oxide experiment (SONEX). *J. Geophys. Res. 105*, D3, 3745-3755.

Microphysics of Cirrus Clouds and its Dependency on Different Types of Aerosols

A. Mangold*, M. Krämer
FZ Jülich (FZJ), Institut für Chemie und Dynamik der Geosphäre (ICG-I): Stratosphäre, Jülich, Germany

O. Möhler, R. Wagner, H. Saathoff, S. Büttner, O. Stetzer, U. Schurath
FZ Karlsruhe (FZK), Institut für Meteorologie und Klimaforschung, IMK-AAF, Karlsruhe, Germany

C. Giesemann, H. Teichert, V. Ebert
Universität Heidelberg, Physikalisch-Chemisches Institut, Heidelberg, Germany

Keywords: cirrus cloud, ice water content, aerosol, cirrus cloud microphysics

ABSTRACT: The ice water content (IWC), ice crystal number concentration and median diameter were investigated during ice cloud formation experiments in the big aerosol chamber AIDA of FZK. Sulphuric acid and ammonium sulphate solution droplets, as well as mineral dust particles and soot, coated with sulphuric acid, served as ice nuclei. The temperature range for the presented experiments was 200 K to 225 K. No clear influence of the aerosol type on the total IWC was found, except for a slight tendency of mineral dust towards a higher IWC compared to the other ice nuclei. Independent of the investigated aerosol types, the ice crystal number concentration increased with decreasing temperature, whereas the median diameter decreased. When using ammonium sulphate solution droplets instead of sulphuric acid solution droplets as ice nuclei (at the same critical cooling rate for ice nucleation), more and smaller ice crystals were formed.

1 INTRODUCTION

As upper tropospheric cirrus clouds play an important role for the earth´s climate, it is essential to understand the formation of such clouds. A key issue remains a reliable parameterisation of the partitioning of the available water into the gas, liquid and solid phase during the process of ice nucleation and ice crystal growth. So far, there are only few experimental data providing direct access to the gas phase and the IWC (e.g. the recent CRYSTAL-FACE campaign of 2002, see http://cloud1.arc.nasa.gov/crystalface/index.html). For a proper parameterisation of the optical properties and the ice cloud microphysics, experimental data which examine the conditions under which different ice crystal number densities and size distributions form, are of major importance.

Measurements of water vapour and ice supersaturations inside cirrus clouds were carried out during the INCA campaign in 2000 (Ovarlez et al., 2002). Kärcher and Ström (2003) found that the dynamical variability during ice formation is a crucial factor for determining the ice crystal properties. Kärcher and Lohmann (2002) stated that in the case of sulphuric acid solution droplets the number of ice crystals formed via homogeneous freezing is rather insensitive to the aerosol size distribution compared to the influence of the updraft velocity. At higher updraft speeds and lower temperatures more ice crystals would nucleate this way. Kärcher (2002) underlined the essential role of updraft velocity and temperature for the microphysical and optical properties of subvisible cirrus clouds.

Here, we present results of laboratory measurements of the water partitioning during cirrus cloud formation, representing upper tropospheric conditions, for different temperatures and types of aerosol particles. The experiments were conducted at the AIDA aerosol chamber of FZK in 2002 at temperatures between 200 K and 225 K. Sulphuric acid and ammonium sulphate solution droplets, soot coated with sulphuric acid and mineral dust (Arizona Test Dust) served as nuclei for ice formation.

* *Corresponding author:* Alexander Mangold, Forschungszentrum Jülich GmbH, ICG-I, D-52425 Jülich, Germany. Email: a.mangold@fz-juelich.de

2 ICE NUCLEATION EXPERIMENTS

2.1 *AIDA Aerosol and cloud chamber facility*

The AIDA aerosol chamber is a large coolable and evacuable vessel of 84 m³ which can be cooled down to 183 K. The pressure range covers 0.1 hPa to 1000 hPa. For details on the instrumentation and on the ice nucleation experiments, see Möhler et al. (2003).

Under constant wall and gas temperatures, ice saturation was maintained by a thin ice layer on the chamber walls. The ice supersaturation necessary for the homogeneous or heterogeneous formation of ice crystals was achieved by 'volume expansion' due to controlled pumping, usually from 1000 hPa to 800 hPa. During pumping the ice supersaturation increased by up to 50 %/min.

The onset of ice formation was detected precisely by measuring the depolarisation of backscattered laser light with high sensitivity and time resolution of 1 Hz. The Lyman-α-fluorescence hygrometer (FISH) of FZJ was used to measure the total water content (gas phase + condensed phase). Simultaneously, the gas phase water concentration was directly measured in situ by absorption at 1370 nm with a tuneable diode laser (TDL). Number concentration and size distribution of the ice particles were obtained using in situ multi-path FTIR extinction spectroscopy.

2.2 *Typical ice nucleation experiment*

Figures 1-4 illustrate the water fluxes and partitioning during the ice formation process in the AIDA chamber. With the beginning of pumping (see Fig. 3 for the time series of the pressure, gas and wall temperature, respectively) the H_2O partial pressure (e) decreased (Fig. 1). When e dropped below the water vapour saturation pressure over ice with regard to the wall ($e_{sat\_ice\_wall}$), a water flux into the chamber started. Due to the expansion cooling, the gas phase water vapour saturation pressure over ice ($e_{sat\_ice\_gas}$) dropped below the actual water vapour pressure. As soon as the critical ice supersaturation (Fig. 4) was reached, ice particles began to form.

The lower water pressure over ice and the gradient between e and $e_{sat\_ice\_wall}$ triggered an ongoing water flux into the chamber and from the gas phase directly to the ice phase. This resulted in an increase in the total water signal. The decrease of the gas phase water (Fig. 2) was caused by the faster water transport from the gas volume to the ice nuclei compared to its transport from the chamber walls into the gas volume. The total water signal increased as long as $e_{sat\_ice\_gas}$ was below $e_{sat\_ice\_wall}$. At the same time the ice crystals grew as long as e was above or equal $e_{sat\_ice\_gas}$ ($rH_{ice} \geq$ 100 %). With the increasing gas temperature after the end of pumping, $e_{sat\_ice\_gas}$ rose first above the actual value in the gas phase, rH_{ice} dropped below 100 % and the ice crystals started to evaporate. As soon as $e_{sat\_ice\_gas}$ also exceeded the respective value for the ice covered walls of the chamber, a water flux back to these walls began. A source of uncertainty for the values of the water vapour saturation pressures remain the errors for the temperature measurements and the temperature inhomogeneities in the great chamber volume and of its walls, due to some hot spots caused e.g. by the heating of the inlet tube for the total water measurements. This uncertainty is ± 0.1 K at constant p and T conditions and rises up to less than ± 0.3 K during expansions, depending on pumping speed.

By subtracting the gas phase water vapour mixing ratio from the total water mixing ratio we are able to derive the ice water content directly from the measurements. The ice water content may be slightly underestimated due to ice particle sedimentation or impaction inside the chamber.

3 RESULTS

3.1 *Ice cloud microphysics for two exemplary cases*

Here we discuss the development of the ice phase for two experiments – one with sulphuric acid as ice nuclei and one with ammonium sulphate. Figures 5 (sulphuric acid) and 6 (ammonium sulphate) show the development of the IWC measured during the experiments – both the total IWC and the parts coming from the initial gas phase or the wall. Both experiments started at the same temperature (200 K), pressure (1000 hPa) and pumping rate. The beginning of the time axis is also the start of pumping.

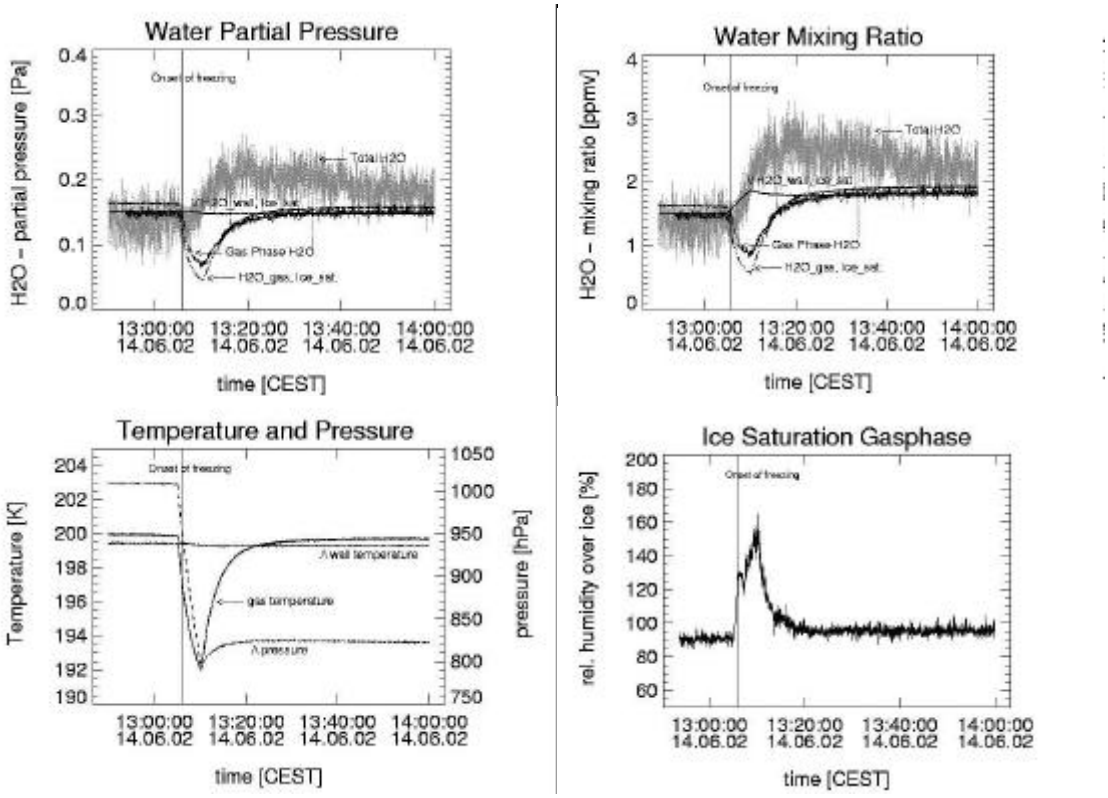

Figures 1-4. Time series of the water partial pressure (Fig. 1, upper left), water mixing ratio (Fig. 2, upper right), gas temperature, wall temperature and pressure in the AIDA chamber (Fig. 3, lower left) and the relative humidity over ice (Fig. 4, lower right), measured by the TDL and calculated after Marti and Mauersberger (1993).

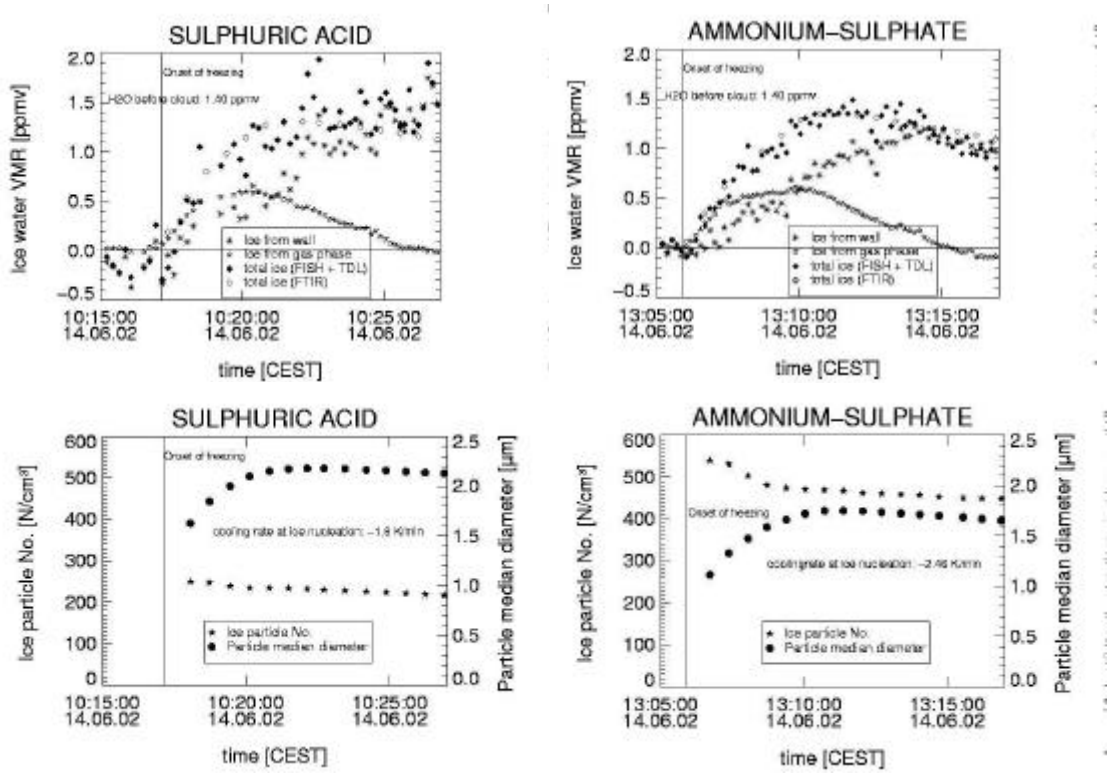

Figures 5-8. Exemplary cases for the development of the IWC. Figure 5 (upper left) shows the evolution of the IWC during an expansion experiment for sulphuric acid solution droplets as ice nuclei, whereas Figure 6 (upper right) displays the comparable experiment for ammonium sulphate solution droplets. The lower graphs show the development of the ice crystal number concentration and median diameter – both for sulphuric acid (lower left) and ammonium sulphate (lower right) solution droplets.

The initial aerosol number concentrations were 10,000 cm^{-3} (sulphuric acid case) and 2850 cm^{-3} (ammonium sulphate case). The median diameter of the aerosol was ~0.3 µm in both cases. We derived the amount of ice water coming from the gas phase from the TDL measurements by calculating the difference between the initial gas phase water content (average over 5 min before start of pumping) and the current value. The respective calculations with the total water measurements of the FISH yielded the part of ice water coming from the wall. The total IWC was given by subtracting the measured gas phase water from the measured total water. The total IWC was also obtained from the FTIR measurements by retrieving the ice crystal size distribution from the measured optical depth, adopting log-normally distributed particle sizes (for details see Wagner et al., 2003). The results presented here were derived by assuming Mie theory approximation to be valid. First test calculations applying the T-matrix method for nonspherical ice particles (finite cylinders, aspect ratio D/L = 0.7) indicate that the influence of particle asphericity on the IWC is well below 10 % for the range of ice crystal sizes covered by this work.

The agreement between both methods for determining the IWC was very good. The maximum value for the IWC was ~1.3 ppmv. There was no clear difference between the two types of aerosols– both in the total ice water content and the ice water content coming either from the gas phase or the wall. In the sulphuric acid case, the FISH values showed greater scatter, caused by problems with the Lyman-α-lamp.

For the same experiments, Figures 7 (sulphuric acid) and 8 (ammonium sulphate) illustrate the evolution of the ice particle number concentration and their median diameter for the same time period as in Figures 5 and 6. Ammonium sulphate as ice nuclei yielded more but smaller ice crystals compared to sulphuric acid. This could be explained by the higher critical cooling rate for the experiment with ammonium sulphate. Note that in our experiments the pumping rates were always the same but that the onset of freezing was distinctly earlier for ammonium sulphate solution droplets. In our experimental set-up the temperature decrease was steepest at the beginning (see Fig. 3). This resulted in a higher critical cooling rate. Kärcher and Ström (2003) concluded that the amount of ice crystals produced depend strongly on the updraft velocity and therefore on the cooling rate. This could be one reason explaining our results of ice crystal number concentrations and median diameters. It also means that the critical ice supersaturation for ice formation was lower for ammonium sulphate solution droplets than for sulphuric acid. This seems to be in contrast to Koop et al. (2000), provided that the aerosol initially contained only aqueous particles but no crystalline ammonium sulphate. Preliminary data analysis revealed no indications that this would have been the case.

As explained in chapter 2.2, the slight decrease in ice crystal number concentration and median diameter could be ascribed to sedimentation or impaction inside the chamber and evaporation which started, when rH_{ice} dropped below 100 %. For the ice crystal parameters, derived from the FTIR measurements, the crystal asphericity causes a greater uncertainty in these parameters than for the IWC. Our preliminary error estimations are therefore ± 10 % for the ice crystal median diameter and up to ± 20 % for the number concentration.

3.2 *Ice cloud microphysics – dependence on temperature and aerosol*

Figure 9 displays the maximum IWC as measured in the AIDA chamber for different types of aerosols and temperatures. All points correspond to experiments with the same pumping rate. It is obvious that with higher temperature the IWC increased. For temperatures of approximately 200 K and 210 K, there was hardly any difference for the investigated aerosols (also if we would zoom up the scale for the points at 200 K). However, at higher temperatures, there was a tendency towards higher IWC with mineral dust aerosol compared to sulphuric acid or ammonium sulphate solution droplets. The values for the IWC derived from the FTIR agreed very well with total water (FISH) and gas phase water (TDL) measurements.

Figure 10 shows the ice particle number concentration and size, obtained from the FTIR measurements, for both sulphuric acid and ammonium sulphate for a set of three different temperatures but identical pumping rates – for the point of time when the IWC reached its maximum. It clearly can be seen that in general, the number concentration increased with lower temperatures while the median diameter decreased. In the temperature range presented below, ammonium sulphate always produced more ice crystals than sulphuric acid, which were also

smaller, except for the case at ~224 K, when both aerosols yielded almost the same size of the ice crystals.

Table 1 summarises the most important values for our presented ice nucleation experiments – both for sulphuric acid and ammonium sulphate solution droplets. The accordance between the ice water measurements of the FISH – TDL and the FITR, respectively, is striking.

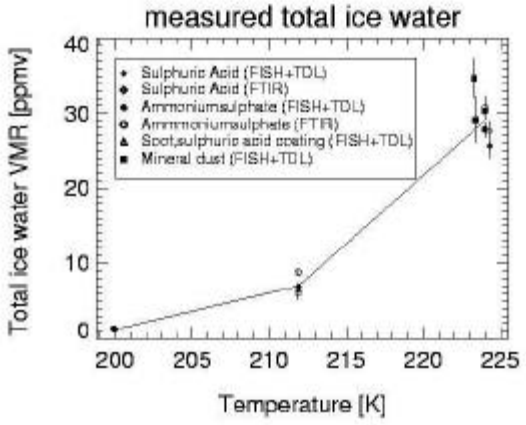

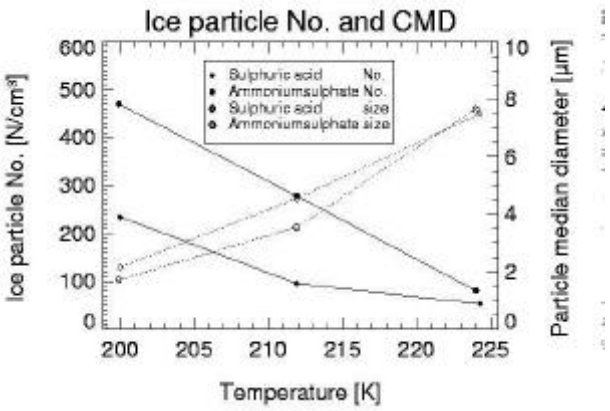

Figures 9 and 10. The left graph (Fig. 9) shows the maximum IWC for different aerosols as ice nuclei for temperatures ranging from 200 K to 225 K. The right graph (Fig. 10) displays the ice particle number concentration and median diameter, derived from the FTIR, for both sulphuric acid and ammonium sulphate solution droplets for the same temperature range and the maximum IWC.

Table 1. Summarised results for sulphuric acid and ammonium sulphate solution droplets as ice nulcei

Temperature at ice nucleation [K]	Type of aerosol	Cooling rate at ice nucleation [K/min]	Ice particle number [N/cm^3]	Ice particle median diameter [µm]	Total IWC by FISH-TDl [ppmv]	Total IWC by FTIR [ppmv]
195.2	Sulph.acid	-1.60	234.4	2.153	1.14 ± 0.39	1.27
210.0	Sulph.acid	-2.66	95.3	4.537	6.84± 0.28	6.92
222.7	Sulph.acid	-3.31	52.7	7.496	25.62 ± 1.60	27.59
197.6	Amm.Sulph.	-2.46	469.8	1.719	1.25 ± 0.28	1.28
210.1	Amm.Sulph.	-2.72	278.5	3.550	6.80 ± 0.30	8.84
222.1	Amm.Sulph.	-3.12	80.5	7.547	27.81 ± 1.00	30.67

The values for the ice crystals and the ice water content correspond to the point of time when the measured ice water content has reached its maximum.

4 CONCLUSIONS

We measured the ice water content and the ice crystal number concentration and median diameter for different types of aerosols at temperatures ranging from 200 K to 225 K. As expected, the IWC generally decreased with decreasing temperature. We observed no clear influence of the aerosol type on the total IWC, except for the one experiment with mineral dust aerosol. That one showed a slight tendency towards a higher IWC compared to sulphuric acid and ammonium sulphate solution droplets. We found no clear difference between sulphuric acid and ammonium sulphate concerning the ice water coming either directly from the gas phase or from the wall.

The values for the total IWC, derived either from the FISH – TDL measurements or from the FTIR measurements, agreed very well. This affirms the possibility to gain information about ice clouds via these techniques.

Looking at the ice particle number concentration and median diameter, we found that with decreasing temperature, the ice crystal number increased and their size decreased – independent of the aerosol type investigated.

Our measurements revealed a difference for the resulting ice cloud microphysics between ammonium sulphate and sulphuric acid as ice nuclei. Ammonium sulphate produced, at the same critical cooling rate, more and smaller ice crystals.

REFERENCES

Kärcher, B., 2002: Properties of subvisible clouds formed by homogeneous freezing. Atmos. Chem. Phys., 2, 161-170.

Kärcher, B. and U. Lohmann, 2002: A parameterization of cirrus cloud formation: Homogeneous freezing of supercooled aerosols. *J. Geophys. Res., 107(D2)*, 4010, doi:10.1029/2001JD000470.

Kärcher, B. and J. Ström, 2003: The roles of dynamical variability and aerosols in cirrus cloud formation. *Atmos. Chem. Phys., 3*, 823-838.

Koop, T., B. Luo, A. Tsias, and T. Peter, 2000: Water acitivity as the determinant for homogeneous ice nucleation in aqueous solutions. *Nature, 406*, 611-614.

Marti, J. and K. Mauersberger, 1993: A survey and new measurements of ice vapour pressure at temperatures between 170 K and 250 K. *Geophys. Res. Lett., 20*, 363-366.

Möhler, O., O. Stetzer, S. Schaefers, C. Linke, M. Schnaiter, R. Tiede, H. Saathoff, M. Krämer, A. Mangold, P. Budz, P. Zink, J. Schreiner, K. Mauersberger, W. Haag, B. Kärcher, and U. Schurath, 2003: Experimental investigation of homogeneous freezing of sulphuric acid particles in the aerosol chamber AIDA. *Atmos. Chem. Phys., 3*, 211-223.

Ovarlez, J., J.-F. Gayet, K. Gierens, J. Ström, H. Ovarlez, F. Auriol, R. Busen, and U. Schumann, 2002: Water vapour measurements inside cirrus clouds in Northern and Southern hemispheres during INCA. *Geophys. Res. Lett., 29(16)*, 1813, doi:10.1029/2001GL014440.

Wagner, R., A. Mangold, O. Möhler, H. Saathoff, M. Schnaiter, and U. Schurath, 2003: A quantitative test of infrared optical constants for supercooled sulphuric acid and nitric acid droplet aerosols. *Atmos. Chem. Phys., 3*, 1147-1164.

3-D Simulation of Contrail to Cirrus Transition - the Onset of Sedimentation

Johannes K. Nielsen*
Danish Meteorological Institute, Lyngbyvej 100, DK-2100 Kbh. Ø, Denmark .

Keywords: Wind shear, size distribution, sedimentation, contrail life time.

ABSTRACT: The processes controlling development of contrails into cirrus are deposition, sublimation, size dependent sedimentation and stretching due to wind shear. The interplay between these processes may be studied in detail with the Microphysical Cirrus (MPC) model. As an example, a specific scenario where contrails were observed over several hours is simulated. The results shows that within 30 minutes a contrail can spread out up to several kilometers horizontally.

1 INTRODUCTION

The increasing concerns about the radiational effects of aged contrails which have turned into cirrus clouds calls for detailed model studies of such processes. The quantities which are needed are specifically lifetime, horizontal and vertical extension and extinction coefficients. In other words, ultimately a contrail parameterization scheme which includes the aging of contrails based on known parameters like humidity, aviation intensity, wind shear etc. is needed. The initial processes in very young contrails has been simulated by Gierens and Jensen (1998), and a 2-D study by Ström and Gierens (2002) followed sedimentation of a cryoplane contrail up to 1.5 h. While the detailed flow dynamics of this study allowed to model the vortices of young contrails, the microphysical particle representation in this model was quite simplified.
This extended abstract focuses on the aging of contrails into cirrus, by employing a detailed microphysical box model embedded in a 3-D fluid simulation which takes into account wind transport and size dependent sedimentation.

2 THE MPC MODEL

The MicroPhysical Cirrus (MPC) model is an integrated model developed at DMI which combines a well tested microphysical box-model with a quite accurate 3-D advection scheme. The microphysical kernel was originately developed for simulations of PSC clouds (Larsen 2000), and as a consequence the MPC-model may be applied on PSC-clouds as well as cirrus clouds. The dynamical variables of the model are gas-phase mixing ratios of water and HNO_3, size-distributions (in these simulations 51 bins) of 4 different particle types, (supercooled ternary solutions, sulphuric acid tetrahydrate, nitric acid trihydrate and ice) and in-particle weight fractions of condensed phase constituents. The model includes nucleation processes and detailed sedimentation calculation on each size bin. Wind transport, sedimentation and parts of the particle growth processes are calculated by the Walcek-algorithm (Walcek 2000). At the present, the model is being combined with optical routines so that extinction coefficients and backscattering ratios can be calculated.

3 SIMULATION DETAILS

The wind pressure and temperature fields are interpolated ECMWF data. The initial humidity was initialized from a local radio sounding launched close to simulation start time (see Figure 1). The sounding shows a region with supersaturation around 11 km altitude. No corrections were applied to this sounding, and it is likely that it underestimates humidity near the tropopause. The simulation box follows the wind field (for 0.5 hour) in order to keep the cloud inside the box. The simulation

* *Corresponding author:* Johannes Nielsen, DMI, Lyngbyvej 100,DK 2100 KBHØ. Denmark, Email: jkn@dmi.dk

was initiated with a 150 seconds old contrail, which has been characterized by Gierens and Jensen (1998). The ice particle density of the contrails were initialized to 500 particles/ccm, with mean radius 1 micrometer. The initial contrail cross section was 250 m (horizontal) and 150 m (vertical). The simulation presented here was carried out on a laptop, during 10 hours. The grid is 36x36 x36, the maximum time step is 15 sec., and the number of logarithmically spaced size bins are 51 ([0.001:200] micrometer).

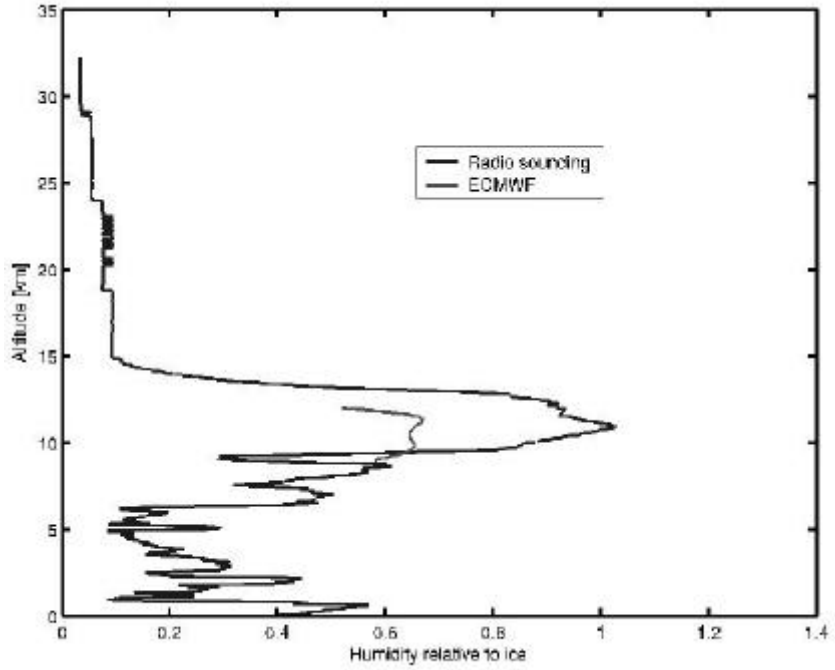

Figure 1. Humidity profile recorded from radiosounding Jægersborg March 16 03 12:00 UTC (DMI).

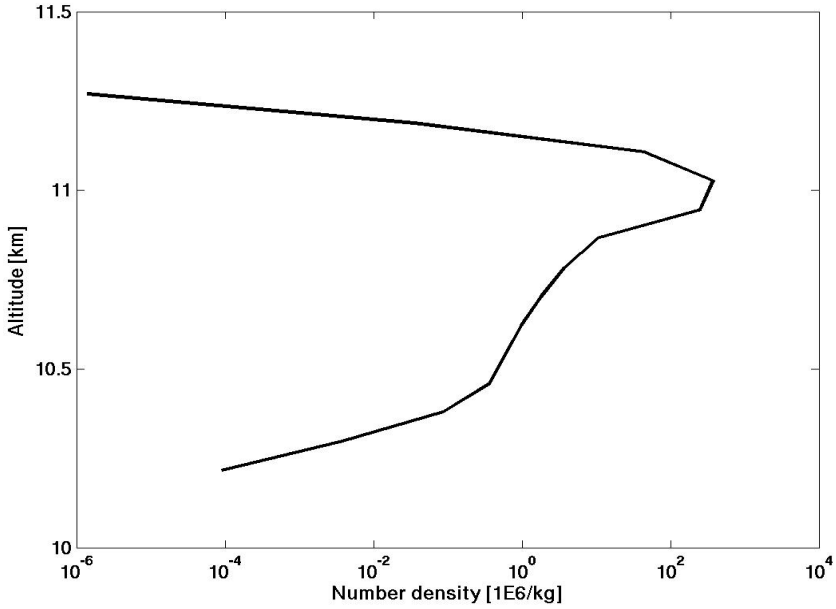

Figure 2. In cloud particle density 0.5 h into simulation.

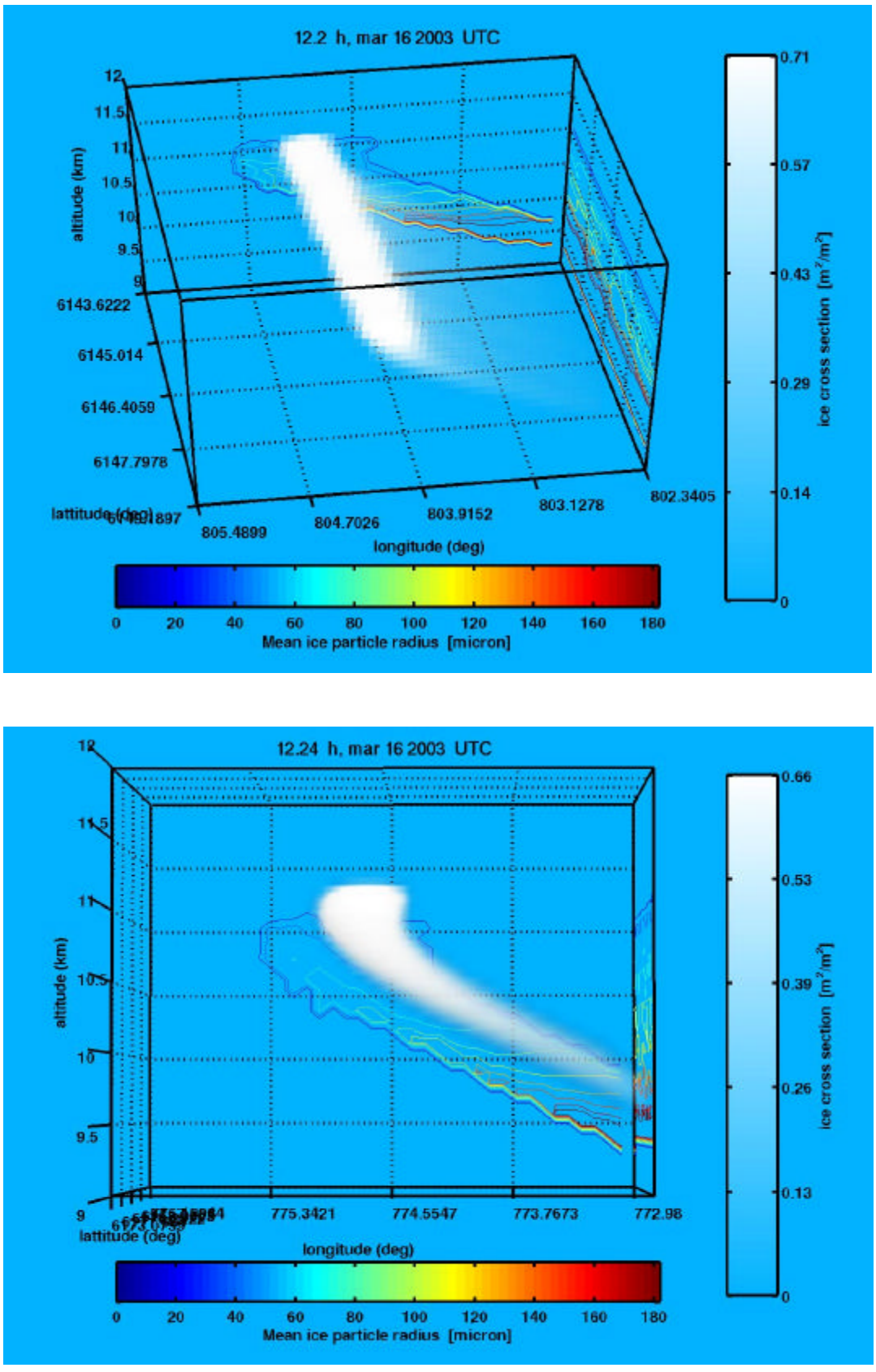

Figure 3: Two simulation snapshots Cloudplots are produced by superimposing layers of opacity proportional to the local cross-section denisity. Looking through the cloud one sees the integrated cross section area, which gives a quite good impression of the physical distribution of the cloud.

4 RESULTS

Sedimentation starts after a few minutes, and is speeded up as particles enter the humid region below the cloud. The largest particles occur in the first fall streak front which enters into a supersaturated region with a thickness of 1 km. Their radius grow up to a 180 micrometer (shown by contours at walls). As this front vanishes into the subsaturated region below 10 km altitude, the mean radius falls to below 50 micrometers in the bulk of the cloud. Even though the lower parts of the cloud appears quite dense, the number density is only about 5-10 particles per ccm. The cloud remains visible because of the larger particle size. Due to shear motion under the tropopause the contrail is spread out significantly. After 0.2 hour it ranges over about 2 km horizontally, and 1 km vertically. It then stays at this size because the lower parts begin to sublimate. The particle density in the upper part decreases of course during the 0.5 h simulation, but only to 65 % of the initial value, thus there is nothing to hinder the cloud from existing much longer (unfortunately it escaped out of the box in this simulation).

5 CONCLUSION

This extended abstract demonstrates that detailed simulations of contrail aging may indeed be performed. The contrail in this simulation persists for at least 0.5 h, - which is the duration of this relatively short simulation. It ranges over approximately 2 kilometers horizontally. In near future statistical analysis of several simulations of this kind spanning over a range of atmospheric conditions may help to parameterize the impact of cirrus clouds origining from airplane traffic in global models.

REFERENCES

Gierens, K. and Jensen, E., 1998: A numerical study of the contrail-to-cirrus transition. *Geophys. Res. Lett., 25* ,4341-4344.

Larsen, N., 2000: Polar Stratospheric Clouds - Microphysical and optical models. *Technical Report, 00-06, Danish Meteorological Institute, Copenhagen.*

Ström, L. and Gierens, 2002 : First simulation of cryoplane contrails. *J. Geophys. Res. 107,* (D18), 4346, doi:10.1029/2001JD000838, 2002.

Walcek, C. J.,2000: Minor flux adjustment near mixing ratio extremes for simplified yet highly accurate monotonic calculation of tracer advection, *J. Geophys. Res. 105*, 9335-9348.

Heterogeneous nucleation effects on cirrus cloud coverage

K. Gierens*, S. Brinkop
DLR-Institut für Physik der Atmosphäre, Oberpfaffenhofen, Germany

Keywords: cirrus, indirect effect of 1st kind, heterogeneous nucleation

ABSTRACT: The indirect effect of 1st kind of aerosols is the effect of additional ice nuclei capable of heterogeneous nucleation on cirrus formation. It is usually thought to lead to enhanced cloud coverage. In this paper we discuss that this view may be too simple. Experiments conducted with a general circulation model and including both homogeneous and heterogeneous cirrus formation paths and a novel cirrus cover parametrisation showed reduced cloud coverage compared to a control run. Unfortunately, the results depend sensitively on a number of uncertain parameters. Thus an assessment of the climatic role of the indirect effect of aircraft aerosol does not seem to be in reach currently.

1 NOVEL PARAMETERISATIONS FOR CIRRUS CLOUD COVERAGE

The current investigation requires that both homogeneous and heterogeneous cirrus formation pathways are represented in the model and that the coverage resulting from both formation paths can be determined separately. In order to achieve this we implemented a switch in ECHAM's cloud physics routines that decides at every time step and in each grid box whether homogeneous or heterogeneous nucleation takes place (if at all). This is decided by means of a critical concentration of heterogeneous freezing nuclei that depends in particular on updraft speed, temperature, and the assumed ice supersaturation at which heterogeneous freezing would commence (for details see Gierens, 2003). Figure 1 gives some examples of the critical concentration.

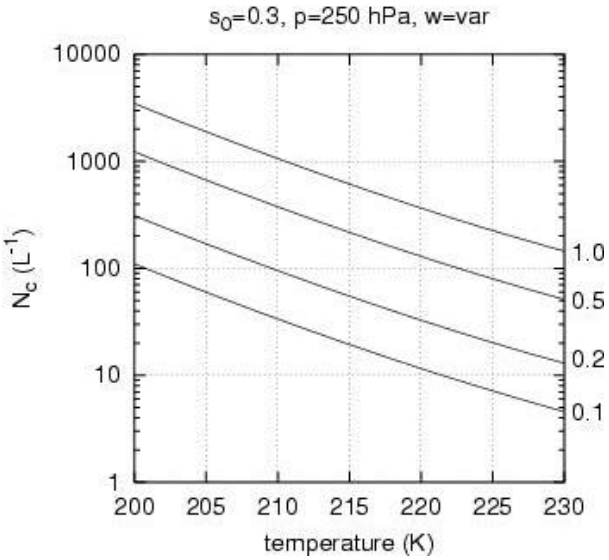

Figure 1. Critical concentration of heterogeneous freezing nuclei as function of temperature and updraft speed (curve parameter on the rhs of the figure). A threshold ice-supersaturation necessary for heterogeneous freezing of 0.3 (i.e. *Rhi*=130%) was assumed for the calculation of the curves.

* *Corresponding author:* Klaus Gierens, DLR-Institut für Physik der Atmosphäre, Oberpfaffenhofen, D-82234 Wessling, Germany. Email: klaus.gierens@dlr.de

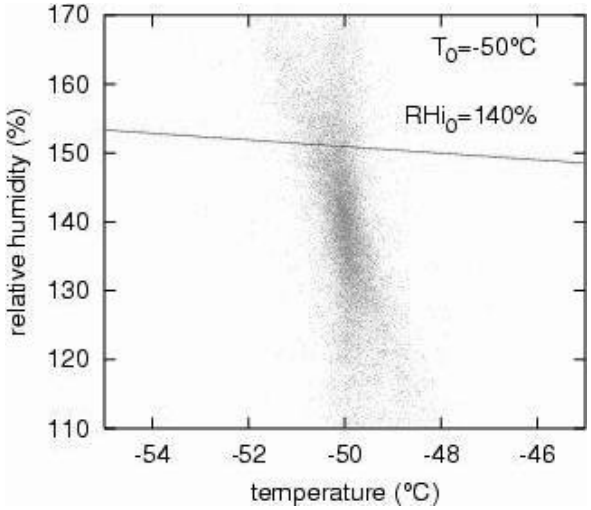

Figure 2. Statistical distribution of instantaneous fluctuations of temperature and relative humidity about grid scale values of T_0=-50°C and Rhi_0=140% for a grid box in T42 resolution. The horizontal line marks the threshold for homogeneous freezing of aqueous solution droplets. All fluctuations (dots) that reach above the threshold imply cirrus formation.

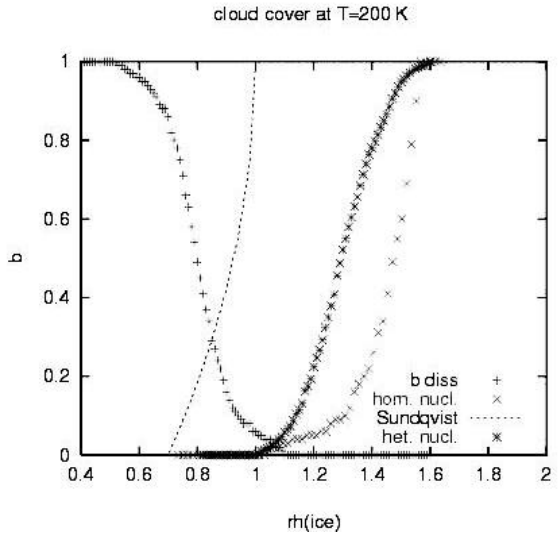

Figure 3. Relation between relative humidity with respect to ice and cirrus cloud cover as it results in ECHAM4 after implementation of the overlap integral method. The dashed line represents the traditional Sundqvist parameterisation, where an overcast sky is assumed already for ice saturation. In contrast the new parameterisations (× and stars for homogeneous and heterogeneous nucleation, resp.) lead to an overcast sky only at high degrees of supersaturation. The curve "b diss" (+) shows the coverage that vanishes in a dissipation situation (i.e. decreasing relative humidity).

If in a certain situation the concentration of heterogeneous freezing nuclei exceeds the critical value, then heterogeneous nucleation occurs, otherwise homogeneous nucleation. A simultaneous action of both freezing processes in the same grid box is not considered. The number of ice crystals forming from a heterogeneous nucleation event equals the critical concentration or a certain fraction thereof (tuning parameter). In an homogeneous nucleation event it is given by the formulations of Kärcher and Lohmann (2002). The updraft speed in a large scale model should be augmented by a measure of the subgrid scale turbulent motions (e.g. TKE). Another currently uncertain parameter is the threshold supersaturation for heterogeneous freezing, for which we chose constant values of 0.3 for soot (if T<−53°C) and 0.1 for mineral dust (if T<−35°C). These values are obtained from recent laboratory measurements (DeMott et al., 1999; Möhler et al., 2003); however, the scatter in the measurement results is large, and thus the chosen thresholds are uncertain.

Cirrus cloud coverage, *b*, is parameterised using the method of overlap integrals. This novel method starts from a division of the state phase space {*T, RH*} into two domains, one in which cirrus can form, and one where this is not the case. The demarcation line between these two domains is the critical supersaturation for (homogeneous or heterogeneous) nucleation. For homogeneous nucleation the critical supersaturation has been obtained from the laboratory results of Koop et al. (2000). For heterogeneous nucleation we use the aforementioned temperature-independent values. Second we use measured distributions of instantaneous random fluctuations of the state phase variables around their grid box mean values. The measured distributions (Gierens et al., 1997) can be fitted with an analytical function formed from two Lorentzian distributions. This 2D-function, centred in the phase space at the respective grid scale value for each box, can overlap partially with the domain where cirrus can be formed. An example of this for is shown in Figure 2 for cirrus coverage due to homogeneous nucleation.

The amount of overlap is the so-called overlap integral. Its value determines the fractional coverage of cirrus clouds. A corresponding formulation can be used for the dissipation of clouds. For this the critical ``supersaturation" is −0.2, i.e. when fluctuations of RH_i (relative humidity with respect to ice) reach below 80%, the cirrus fractional coverage is decreased. As a result, the parameterisation allows for supersaturation, and there is a hysteresis curve in a *RH* vs. *b* diagram (Figure 3).

2 FIRST SIMULATIONS WITH ECHAM

We have used the general circulation model ECHAM4 in T30, L19 resolution, and updated with the parameterisations for homogeneous cirrus formation by Kärcher and Lohmann (2002) to study the effect of a novel consistent cirrus cover parametrisation and heterogeneous freezing on cirrus coverage. Two five year runs have been performed: (1) a control run with homogeneous cirrus formation after Kärcher and Lohmann (2002) and with the traditional coverage parameterisation by Sundqvist (1978), and (2) a test case where the Sundqvist parameterisation has been replaced by our new parameterisation for cirrus coverage and a simple parametrisation for the heterogeneous freezing process.

The results presented here are preliminary since there are a couple of uncertain parameters involved and the model reacts quite sensitively to some of them: background aerosol concentration, freezing thresholds and critical humidities of aerosols. Nevertheless, they made us aware of some potential effects of heterogeneous nucleation on cirrus cloud coverage that we did not see so clearly before.

Figure 4 shows the effect of the new parameterisation on total cloud cover. There is not much of an effect in the lower and middle troposphere, as expected. Generally cirrus cover is reduced compared to the control run due to the higher thresholds to cirrus cover formation (Figure 3). In the control run cirrus cover is already possible if the humidity gets larger than 70% in a grid box. If supersaturation occurs then total overcast conditions are present.

A short sensitivity run with the new cirrus cover parametrisation for homogeneous nucleation only shows a stronger decrease in cirrus coverage compared to the control run and compared to the run with heterogeneous nucleation. For homogeneous cirrus cover development the critical thresholds for humidity and temperature are the most extreme (Figure 3). Thus, heterogeneous nucleation mainly increased cirrus cover in our simulation.

However, as heterogeneous freezing occurs before homogeneous freezing can act, the homogeneous pathway is suppressed to a large degree. Figure 5 shows that in the right panel the homogeneously formed clouds (broken contour) are only present in a shallow region in upper troposphere of the southern hemisphere, otherwise the tropopause region is dominated by heterogeneously formed cirrus (solid contours). In the simulation this is certainly a consequence of the low freezing threshold of s_0=0.1 at T<238K assumed for mineral dust. Sensitivity studies with higher threshold values led to larger cirrus cover in the tropics because then the probability for homogeneous freezing increased which resulted in enhanced cirrus coverage. On the other hand, heterogeneously formed cirrus will usually have lower ice crystal number concentrations than homogeneously formed cirrus. This could lead to larger ice crystals (less competition for the

available water vapour; however, less supersaturation at freezing could balance this), stronger sedimentation, and eventually shorter average life times and hence lower cirrus amount.

In an assessment of the role of the indirect effect of 1st kind of aviation aerosols it is also necessary to compare the average optical thicknesses of both kinds of cirrus clouds, which could also be tested with the current set of simulations. It must be expected that heterogeneously formed cirrus is optically thinner than its counterpart formed homogeneously. This investigation has not yet been done so far.

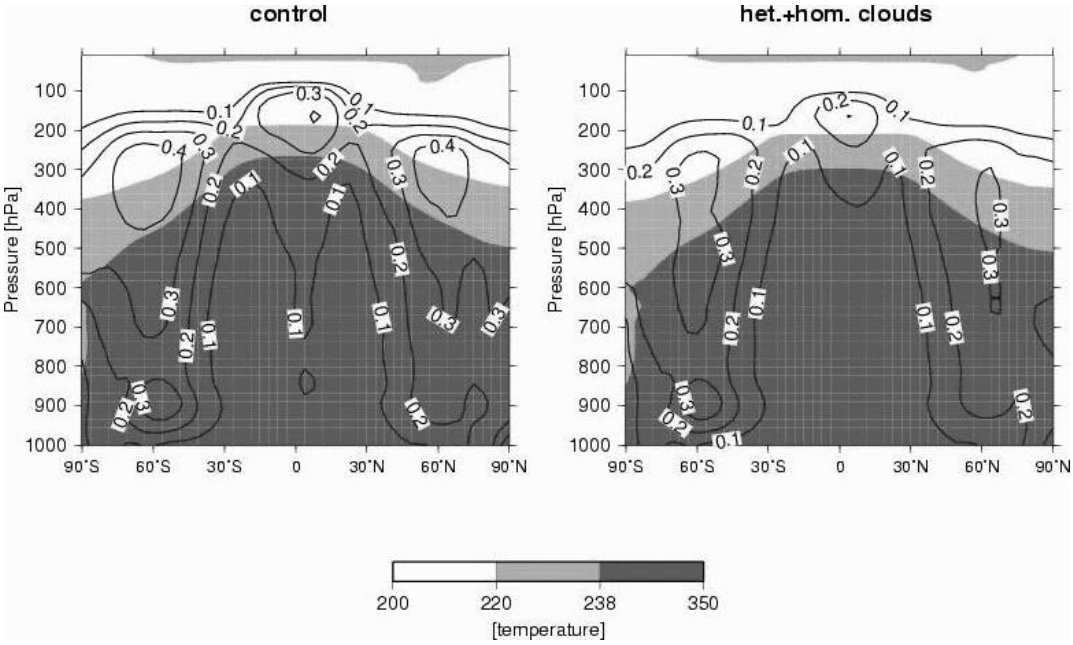

Figure 4. Zonally and annually averaged total cloud cover in a 5-years ECHAM4 simulation with Kärcher and Lohmann (2002) microphysics of homogeneous nucleation. Left panel: control run with Sundqvist (1978) parameterisation of cirrus coverage (without heterogeneous cirrus formation). Right panel: simulation with both homogeneous and heterogeneous freezing and with new parameterisation of cirrus coverage.

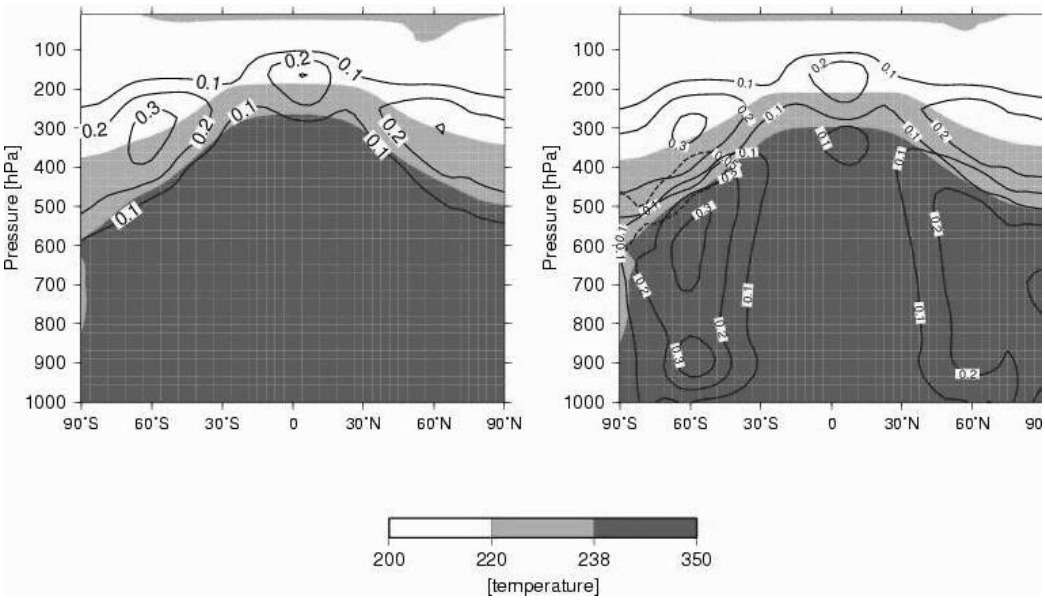

Figure 5. Run with new parameterisation of cirrus coverage. Left panel: Zonally and annually averaged cirrus coverage due to both homogeneous and heterogeneous nucleation. Right panel: Cloud coverage due to different formation pathways, heterogeneously formed cirrus (solid contours in the cold regime, T<238K), homogeneously formed cirrus (dashed contour), and other clouds (solid contours in the warmer regime). It can be noted that due to the assumed low freezing threshold of mineral dust (s_0=0.1 at T<238K) the homogeneous ice formation pathway is almost completely suppressed.

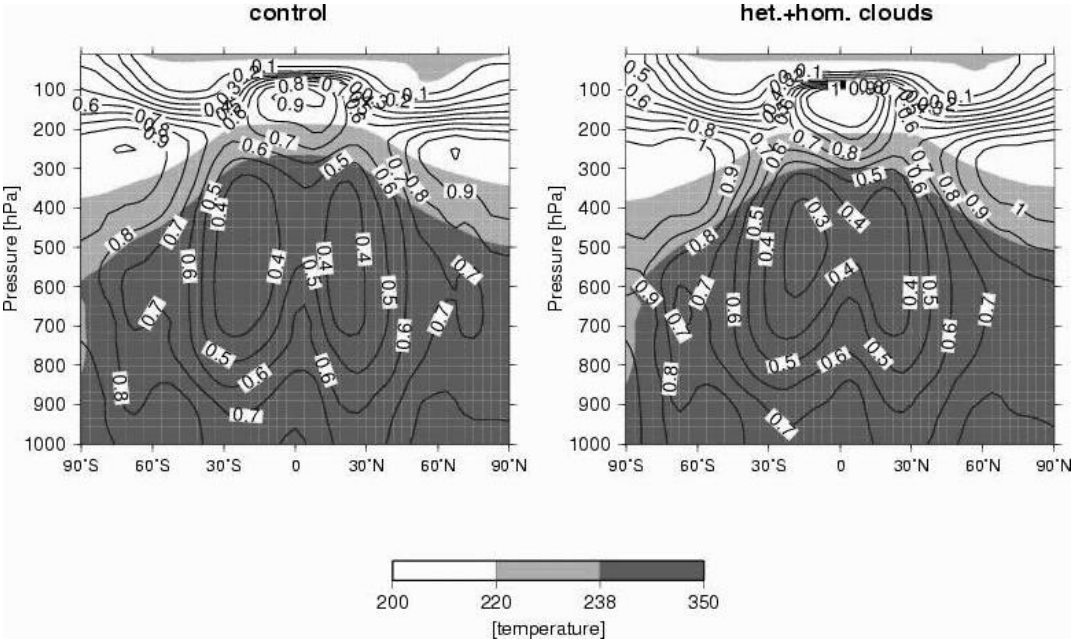

Figure 6. Zonally and annually averaged relative humidity with respect to ice in the control run (left) and the run with new parameterisations (right). It can be seen that the new parameterisations lead to higher average relative humidity values in the upper troposphere of both hemispheres and the tropics. Only in the subtropical subsidence zones there is no effect evident.

Figure 6 shows the effect of the new parameterisation on the average relative humidity field. It can be seen by comparing the left and right panels that the average relative humidity increases almost everywhere in the upper troposphere when the new parameterisation is used. The only exception are the subtropical subsidence zones in both hemispheres where a difference between the control and the sensitivity run is not obvious.

3 SUMMARY AND CONCLUSIONS

The atmosphere is loaded with different kinds of aerosol acting as possible nucleation sites for ice-crystals (black carbon, dust). These aerosol particles may become involved in heterogeneous cirrus formation processes at ice-supersaturations lower than those needed for homogeneous nucleation. Therefore it is generally believed that this so-called indirect effect of aerosol would lead to larger cirrus cloud coverage on average, compared to a hypothetical case with no aerosol emissions. However, this view is too simple. There are competing effects that must be considered in a complete assessment of the indirect effect. First, cirrus formed heterogeneously is probably optically thinner than homogeneously formed cirrus, because crystal numbers are less, and maximum supersaturation during the nucleation event is less. Second, after a heterogeneous cloud has formed the supersaturation is used up for a while, and a homogeneous cloud will not form whereas it would have been formed without the indirect effect. Third, lifetimes of heterogeneously formed clouds may differ systematically from those formed homogeneously. Preliminary results obtained with the ECHAM4 model (involving new parametrisations for cirrus coverage from heterogeneous and homogeneous processes) show indications for these possible effects. The evaluation of the two simulations is not yet complete, hence the causal chain of all these mechanisms is not yet known with sufficient degree of confidence. Unfortunately, there is considerable uncertainty in many of the parameters involved. Thus an assessment of the climatic role of the indirect effect of aircraft aerosols does not seem to be in reach currently.

REFERENCES

DeMott, P.J., Y. Chen, S.M. Kreidenweis, D.C. Rogers and D.E. Sherman, 1999: Ice formation by black carbon particles. *Geophys. Res. Lett. 26*, 2429-2432.

Gierens, K., U. Schumann, H.G.J. Smit, M. Helten and G. Zängl, 1997: Determination of humidity and temperature fluctuations based on MOZAIC data and parameterization of persistent contrail coverage for general circulation models. *Ann. Geophys. 15*, 1057-1066.

Gierens, K., 2003: On the transition between heterogeneous and homogeneous freezing. *Atmos. Chem. Phys. 3*, 437-446.

Kärcher, B. and U. Lohmann, 2002: A parameterization of cirrus cloud formation: Homogeneous freezing including effects of aerosol size. *J. Geophys. Res. 107*, doi: 10.1029./2001JD001429.

Sundqvist, H., 1978: A parameterization scheme for non-convective condensation including prediction of cloud water content. *Quart. J. Roy. Meteor. Soc. 104*, 677-690.

Contrail Coverage over the USA Derived from MODIS and AVHRR Data

R. Palikonda[4], D. N. Phan, V. Chakrapani
Analytical Sciences and Materials, Inc., Hampton, Virginia, USA

Patrick Minnis
Atmospheric Sciences, NASA Langley Research Center, Hampton, Virginia, USA

Keywords: air traffic, contrails, aircraft emission, remote sensing

1 INTRODUCTION

Contrails often lead to the development of additional cirrus clouds that can affect climate via the radiation budget. Evaluation of contrail coverage and optical properties is crucial for assessing the impact of current and future climatic effects of air traffic. Current estimates of contrail coverage over the United States of America (USA) have been based on a single NOAA-16 (N16) afternoon overpass time for recent studies and at four times of day for 1993-94 data from two satellites with different sensitivities and detection errors (Palikonda et al. 1999). Approximately 25,000 flights cross portions of the USA each day at different times of day. The commercial flight activity begins in earnest around 0600 LT and continues with high intensity before fading shortly before local midnight. Because spreading contrail lifetimes are generally less than 4-6 hours, the atmosphere should be cleansed of most contrail coverage by the beginning of the next day (Garber et al. 2003). Assuming that the state of the upper troposphere is, on average, the same during the day, this daily cycle should be reflected in the contrail properties and coverage. However, preliminary studies using NOAA-15 (N15)_morning overpasses suggest that the afternoon analyses may underestimate the contrail coverage because the spreading and saturation of contrails formed during the morning in areas of heavy air traffic might mask or diminish the contrails formed during the afternoon. To obtain a better assessment of the diurnal variation in contrail coverage, this study analyzes data taken during 2001 over the USA from N15 in the early morning period followed by N16 during the afternoon.

2 DATA AND METHODOLOGY

The satellite data used for this study include 1-km radiances from the morning (~0730 LT) N15 and mid-afternoon (~1430 LT) N16 Advanced Very High Resolution Radiometer (AVHRR) overpasses over the continental USA covering the domain between 25°N and 55°N and 65°W and 130°W. The domain is divided into a 30 x 65 1°-region grid. Images from all available overpasses are analyzed to calculate the contrail statistics. Only those regions having more than 90% of the expected number of pixels and having at least ten images each month are used in the monthly statistics. The Monterrey, California receiving station consistently had bad data from the N15 AVHRR resulting in the loss of many western regions in the statistics. In addition, many of the N15 overpasses for January and October yielded corrupted data and were not included in the results. The contrail mask, areal coverage, visible optical depth *OD*, and contrail longwave radiative forcing CLRF are computed as in Palikonda et al. (2002).

[4] *Corresponding author:* Rabindra Palikonda, 1 Enterprise Parkway, Hampton, VA, USA 23666. Email: r.palikonda@larc.nasa.gov

3 RESULTS

Figures 1–4 show the monthly distribution of contrail cover over the domain. During April, for the morning overpass (N15, Fig 1a), maximum contrail coverage occurs over the southeastern states, off the coasts of Texas and Louisiana, and in northern Ohio. In the afternoon (N16, Fig 1b), maximum coverage occurs over North Dakota, Nevada, Washington, northern Mexico, and adjacent Pacific Ocean, areas not available from N15. The N15 maximum over the western Gulf of Mexico is still evident as a relative maximum in the N16 results. The domain averages are 1.29% and 0.71%

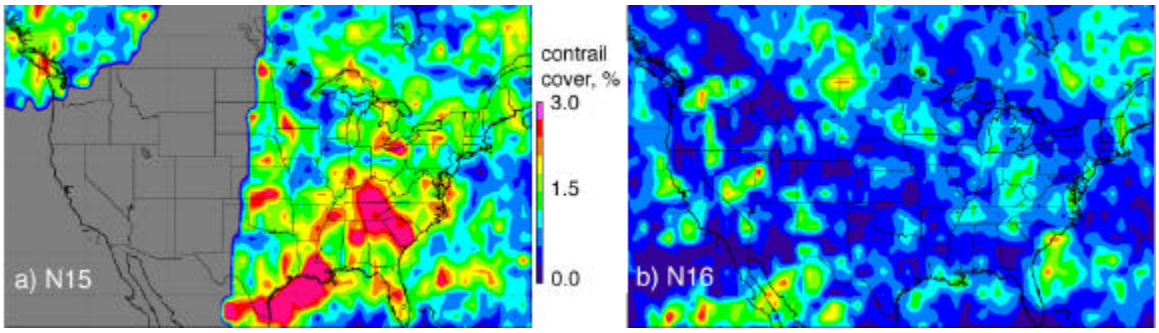

Figure 1. April 2001 daytime contrail coverage

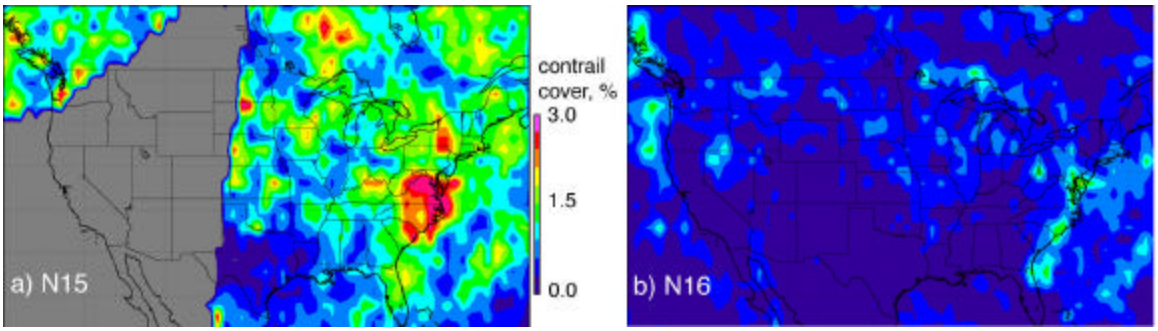

Figure 2. July 2001 daytime contrail coverage

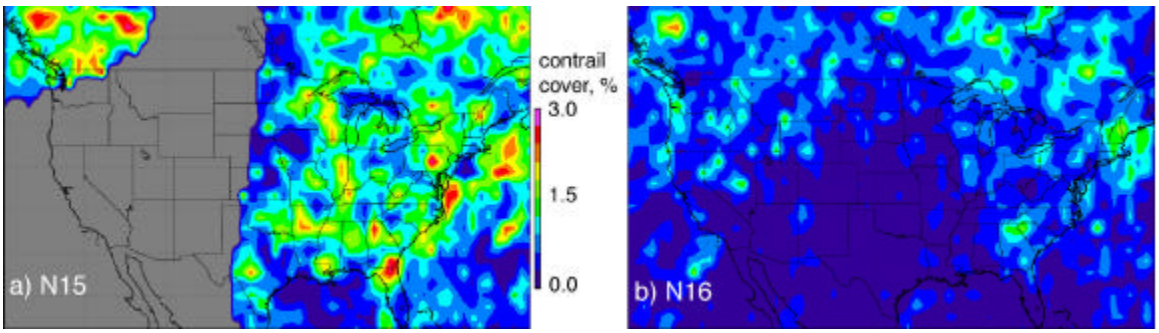

Figure 3. September 2001 daytime contrail coverage.

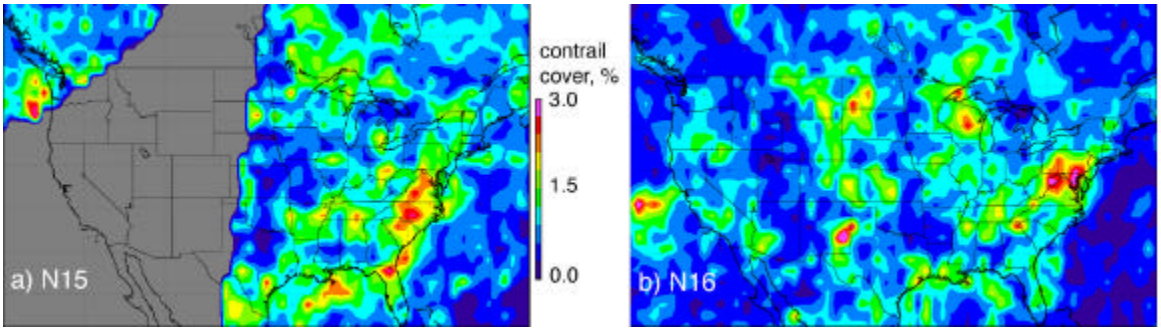

Figure 4. December 2001 daytime contrail coverage.

In the morning and afternoon, respectively. These means include differing numbers of regions. The morning July contrail cover (Fig. 2a) peaks over Virginia, North Carolina, South Carolina, and New York. Minimum coverage occurs over Texas, Louisiana, Alabama, and Minnesota. The areal coverage is almost 70% less during the afternoon (Fig. 2b). A local maximum occurred along the Atlantic coast from Maryland to Florida, and off the coasts of Oregon, Washington, and British Columbia. These areas of maximum coverage are similar to those in the N15 retrievals. The substantial morning-afternoon difference in areal coverage persists in September (Fig. 3). During the morning (Fig. 3a), maximum contrail coverage exceeds 2% over southwestern Canada, Georgia, Pennsylvania, and east of Virginia. The extensive contrail minimum in the afternoon (Fig. 3b) is defined by a triangle extending from southern California to South Dakota and to the tip of Florida. Maximum coverage occurred over British Columbia, Oregon, New England, Quebec, and Lake Winnipeg. During the winter, in the morning (Fig. 4a), contrail cover exceeds 1.5% over the southeastern states and Gulf of Mexico, off the coast of Oregon and Washington. The afternoon coverage during December (Fig. 4b) peaks over northern Virginia, West Virginia, Maryland, and Pennsylvania. Local maxima are seen over New Mexico, Wisconsin, and west of California.

The results, including the mean values for CLRF and *OD*, are summarized in Table 1 for the areas within the domain that are common to both N15 and N16 retrievals. The contrail coverage is greater during the morning than in the afternoon. Perhaps, this variation is a result of the atmosphere being cleaner (fewer flights) during early morning, so contrails are more easily observed and grow more. Also, the upper tropopheric humidity (UTH) is probably greater in the morning from previous day's convection and less in the mid-afternoon prior to convection. The coverage during the afternoon peaks during the winter and is at a minimum during July, differing by a factor of 3. The coverage in the morning is at a maximum during April and minimum during August and September. The most variation between morning and afternoon is seen during summer months, differing by a factor of 2 to 3. The least variation in coverage is during December, when the difference in UTH between morning and afternoon is probably smaller than during the warmer months. Other reasons for the difference include different sensitivities of the N15 and N16 brightness temperature differences (BTD) to the thresholds used for contrail detection and differences in the background temperatures.

The mean contrail optical depths in Table 1 vary with season to some degree. The summer maximum is around 20% greater than the February minimum. Optical depths retrieved from N16 averaged 0.29 compared to 0.26 from N15. This 12% difference is relatively consistent from month to month. The N15 and N16 monthly frequency distributions of contrail optical depth in Figure 5 are remarkably consistent. During all months, $0.2 < OD \leq 0.4$ for more than 30% of the contrails. Thicker contrails were observed more frequently in summer than during the winter and spring.

The contrail radiative forcing (Table 1) in the morning was greatest during the summer months and at a minimum during February. In the afternoon, the maximum and minimum CLRF occurred during April and July, respectively. CLRF depends on both the contrail coverage and its background. Unit CLRF, the ratio of CLRF to the fractional contrail coverage, varies from 8 Wm^{-2} in February to 18 Wm^{-2} during July in the morning. In the afternoon, CLRF varies from 6 Wm^{-2} in February to 27 Wm^{-2} during July indicating that the thermal contrast changed by a factor of 4 between winter and summer compared to a change of less than 50% between morning and afternoon.

On average, the contrail coverage ranges from a minimum of 0.68 during August to a maximum of 1.06 in February. Between February and May, the mean varies by less than 0.08. Similarly, between July and September, it varies by only 0.03. Thus, the periods of minima and maxima are broad and the actual extrema at a given time of day or in a given year could occur in different months than February and August. The mean minimum contrail *OD* (0.235) occurred during February while the maximum average (0.295) was found during July. Mean CLRF ranged from 0.075 Wm^{-2} in March to 0.145 Wm^{-2} during September.

Table 1. NOAA-15 & NOAA16 contrail properties, 2001.

Month	contrail cover (%)		*OD*		CLRF Wm^{-2}	
	N15	N16	N15	N16	N15	N16
January	N/A	0.92	N/A	0.25	N/A	0.11
February	1.19	0.93	0.23	0.24	0.10	0.06
March	1.11	0.86	0.24	0.26	0.10	0.05
April	1.29	0.71	0.25	0.28	0.11	0.14
May	1.40	0.55	0.27	0.31	0.12	0.06
June	1.17	0.44	0.26	0.30	0.15	0.04
July	1.08	0.33	0.28	0.31	0.18	0.09
August	0.97	0.38	0.27	0.30	0.18	0.03
September	0.96	0.45	0.28	0.30	0.18	0.11
October	N/A	0.71	N/A	0.31	N/A	0.09
November	1.04	0.84	0.26	0.28	0.13	0.07
December	0.91	0.80	0.26	0.28	0.14	0.07

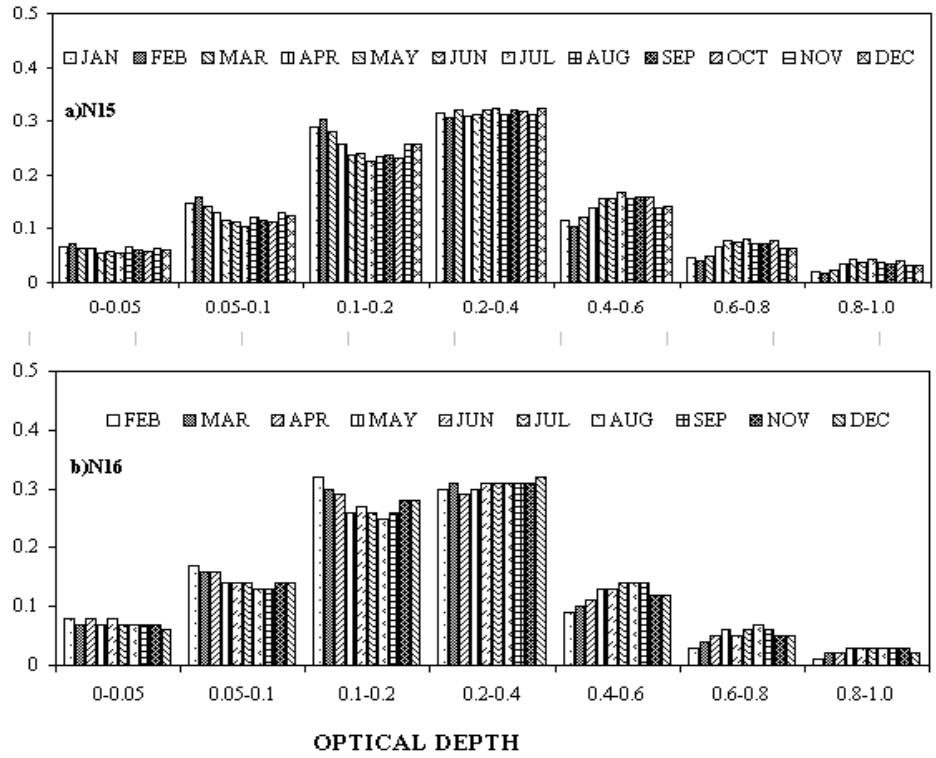

Figure 5. Histogram of daytime contrail optical depths from NOAA-15 and NOAA-16 over USA, 2001.

4 DISCUSSION

As noted earlier, the differences in contrail coverage between the two satellites may be due, in part, to different sensitivities of the 11 and 12-μm channels on the two AVHRRs. Each channel has a slightly different spectral response function and slightly different calibration. Small differences in each channel can translate to large differences in the BTD relative to the pixel-use threshold value. Visually, the BTD images from the two satellites are quite different when constructed using the same temperature range and contrast suggesting that the contrail retrievals would be different using the same methodology. The retrieval error rates have not been established yet. Palikonda et al. (1999) roughly estimated that the error rate for applying the same methodology to AVHRR data from NOAA-11 and 12 resulted in a 25% overestimate of the USA contrail coverage. Meyer et al. (2002) have developed more rigorous correction methods (e.g., false alarm rate, stationary artifacts, detection efficiency) for the NOAA-14 AVHRR contrail analysis that will be constructed for the data used here. Such techniques should account for the cirrus streaks and land forms that can be misinterpreted as contrails.

Table 2. Comparison of estimated USA contrail coverage (%).

Month	Current study 2001	Palikonda et al. (1999) 1993-94	Sausen et al. (1998) Theoretical
April	1.00	2.0	2.0
July	0.70	1.3	0.5
October	~0.85	1.9	1.9
December	0.88	2.1	1.6 (Jan)

Two conditions are necessary for contrail formation: air traffic and suitable atmospheric conditions. The air traffic over the USA is relatively heavy with more than 4000 km of potential contrails (flights above 7 km) every day in a given 1° box (Garber et al. 2003). Thus, the USA contrail coverage can be dominated by formation conditions. Duda et al. (2003) estimated the frequency of potential contrail conditions over the USA using Rapid Update Cycle (RUC) model data. Their Figure 1 showing potential coverage results for September 2001 are very similar to the afternoon contrail coverage in Figure 3. Similar correspondence was also found for November (not shown). Overall, the RUC-based potential USA contrail frequency during 2001 peaked during April at 30% and dropped to a minimum of ~12% during the summer months, nearly reaching a secondary peak in November followed by a decrease during December. The sequence is very similar to the observed contrail variation in Table 1. The contrail coverage is considerably less than the potential because the contrails can only be detected when they are not obscured by existing clouds and air-traffic coincides with the moisture. This consistency with contrail potential and the morning-afternoon optical depth consistencies in Figure 5 lend support to the relative validity of the retrievals.

Table 2 reveals that the contrail coverage is only half of that detected by Palikonda et al. (1999) from 1993-94 NOAA-11 and 12 AVHRR data and calculated by Sausen et al. (1998) using 1992 air traffic densities and multiple years of meteorological data. The relative seasonal variations between 1993-94 and 2001 are nearly identical. Because the air traffic should have increased by more than 30% or more between 1992 and 2001 (e.g., Minnis et al. 2003a), the contrail coverage should have increased. Part of the reduction may be due to missed contrails in the N16 images and to overestimates in the N11 and N12 analyses. Additionally, it should be repeated that the averages in Table 1 and for 2001 in Table 2 do not include a large portion of the western USA (Fig. 1), an area that is likely to account for less contrail coverage than the eastern USA. Minnis et al. (2003a) found a decrease in the frequency of persistent contrails over the USA during 1999 relative to 1993-94 that corresponded to a drop in upper tropospheric humidity (UTH) as indicated by the mean relative humidity (RH) at 300 hPa from the National Center for Environmental Prediction (NCEP) reanalyses data. As seen in Figure 6, the UTH was 45.5% during 1993-94 and dropped to 39.4% during 2001, one of the lowest values during the 30-year period. Since RH is a crucial factor in the formation of contrails, a reduction in RH should result in reduction of contrail cover. From correlations of mean cirrus cloudiness and UTH in areas without heavy air traffic, Minnis et al. 2003b found that cirrus coverage decreases by an average of 0.4%/% UTH. Thus, the cirrus amount would have diminished by ~2.5% over the USA between 1993-94 and 2001 and would likely include a decrease in contrails.

The phasing of the observed seasonal cycles in contrail coverage differs from the theoretical results of Sausen et al. (1998) in Table 2 and Ponater et al. (2002), but is consistent with the contrail frequency observations from surface observations (Minnis et al. 2003a). The observed seasonal range (200%) is only half of that (400%) observed from the surface and computed theoretically. This range difference decreases if only the N16 values are used. This discrepancy and the large N15-N16 contrail coverage difference during summer suggest that the N15 coverage could be overestimated during the summer. Additional analysis is needed to confirm this indication.

The seasonal variation in *OD* is similar to that computed by Ponater et al. (2002) with a maximum during the summer. Similarly, the greater occurrence of optically thick contrails is consistent with the greater maximum contrail optical depth computed by Ponater et al. (2002). However, the theoretical winter minimum relative to the summer maximum is significantly less than the observations. On average, the observed *OD*s are twice the value of those computed theoretically. The CLRF values also are considerably larger than those derived by Ponater et al. (2002). Part of the

difference is due to *OD* discrepancies. The remaining differences are likely a result of differences in the background temperatures and the diurnal cycle in contrail coverage that is not included here.

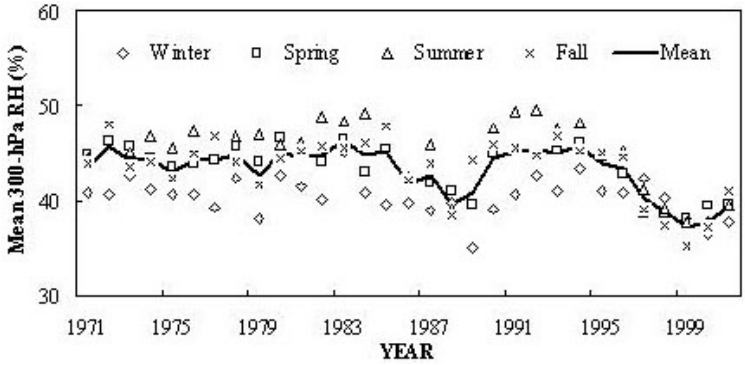

Figure 6. Seasonal and annual mean NCEP RH at 300 hPa over USA.

5 CONCLUSIONS

The preliminary results shown here confirm, for the most part, the relative seasonal variations in contrail coverage and optical depths. Over the USA, contrail coverage peaks during the large winter and early spring and bottoms out during the late summer. Contrail optical depth is greatest during summer. Uncertainties in the magnitudes of contrail coverage, optical depth, and radiative forcing are still large. Refinement of the automated contrail detection methods and detailed error assessments are needed to help resolve some of the remaining large differences between the theoretical calculations and the observations. Until these improvements are implemented, it will not be possible to determine conclusively if the current model estimates are sufficiently accurate for estimating contrail climate effects or whether additional improvements are needed. It is clear that interannual variations in UTH can have a large impact on contrail frequency and coverage. Such variability should be manifest in multi-year modelling results.

REFERENCES

Duda, D. P., P. Minnis, P. K. Costulis, and R. Palikonda, 2003: CONUS contrail frequency from RUC and flight track data. *Proc. European Conf. On Aviation, Atmosphere and Climate*, Friedrichshafen at Lake Constance, Germany, June 30 – July 3.

Garber, D. P., P. Minnis, and P. K. Costulis, 2003: A USA commercial flight track database for upper tropospheric aircraft emission studies. *Proc. European Conf. Aviation, Atmosphere, and Climate*, Friedrichshafen at Lake Constance, Germany, June 30 - July 3.

Meyer, R., H. Mannstein, R. Meerkötter, U. Schumann, and P. Wendling, 2002: Regional radiative forcing by line-shaped contrails derived from satellite data. *J. Geophys. Res. 107*, 10.1029/2001JD000426

Minnis, P. J. K. Ayers, M. L. Nordeen, and S. Weaver, 2003a: Contrail frequency over the United States from surface observations. *J. Climate*, in press.

Minnis, P., J. K. Ayers, R. Palikonda, and D. Phan, 2003b: Contrails, cirrus trends, and climate. *J. Climate*, submitted.

Palikonda, R., P. Minnis, P. K. Costulis, D. P. Duda, 2002: Contrail climatology over the USA from MODIS and AVHRR data. *Proc. 10th Conf. on Aviation, Range, and Aerospace Meteorology*, Portland, OR, May 13-16, J9-J12.

Ponater, M., S. Marquart, and R. Sausen, 2002: Contrails in a comprehensive global climate model: Parameterization and radiative forcing results. *J. Geophys. Res., 107*, 10,1029/2001JD000429.

Sausen, R., K. Gierens, M. Ponater, and U. Schumann, 1998: A diagnostic study of the global distribution of contrails. Part 1: Present day climate. *Theor. Appl. Climatol., 61*, 127-141.

Contrail Coverage Over the North Pacific from AVHRR and MODIS Data

Patrick Minnis[5]
Atmospheric Sciences, NASA Langley Research Center, Hampton, Virginia, USA

Rabindra Palikonda, J. Kirk Ayers
AS&M, Inc., Hampton, Virginia, USA

Keywords: trans-Pacific air traffic, remote sensing, contrails, satellites

ABSTRACT: An increase of air traffic over the North Pacific during the last 30 years has been accompanied by an increase in cirrus coverage. To help alleviate the uncertainty in the contribution of air traffic to the cirrus increase, an analysis of linear contrail coverage over the region has been initiated using afternoon NOAA-16 AVHRR data. Contrail coverage over the domain between 25° and 55°N and between 120° and 150°W was 0.51% and 0.67% in August 2002 and February 2003, respectively. These preliminary values are twice the average expected from theoretical considerations. Contrail optical depths for the 2 months average 0.26 resulting in a mean unit contrail longwave radiative forcing of 15.5 Wm^{-2}, a value that is comparable to that estimated over the USA from daytime analyses. The seasonal variation is smaller than that over land. The contrail optical depths are twice the mean value expected from theoretical estimates. Efforts are underway to estimate the uncertainties in the results and to analyze additional satellite datasets.

1 INTRODUCTION

Cirrus cloud cover has been increasing over the North Pacific since the 1970's. Although part of the increase may be due to a rise in relative humidity, some of the change is likely caused by contrails forming and spreading as a result of transoceanic air traffic. Analysis of high-resolution satellite data is required to determine the contribution by linear contrails to that increase. The air traffic passes through a region where mean cirrus cloud coverage is generally about half that observed over land, while the upper tropospheric humidity, as indicated by the NCEP reanalysis at 300 hPa, is roughly 10% greater than that over land (Minnis et al. 2003). Thus, the atmosphere over pristine oceanic regions should be more susceptible to contrail-cirrus cloud initiation than that over land areas. Additionally, transoceanic flights travel greater lengths at high altitudes than their continental counterparts and, therefore, should tend to produce longer contrails. The expected linear contrail coverage from theoretical considerations (Sausen et al. 1998) varies between 0% in the mid-Pacific and 1% near San Francisco Bay (Fig. 1a). The flight corridors are well defined in Figure 1. Cirrus coverage rose between 0 and 0.6%/year between 1971 and 1996 (Minnis et al. 2003) over the same area with a maximum increase over northern California (Fig. 1b). Over the ocean, a broad area with the greatest trends in cirrus coverage is centered near 45°N at the western edge of the domain in Figure 1. There is no apparent correlation between the cirrus trends and the theoretically derived contrail coverage. Understanding how the contrails relate to the changes in cirrus coverage necessitates the development of some empirical data on the linear contrail coverage. To begin that effort, this paper presents preliminary analyses of contrails as derived from satellite data over the North Pacific. The retrieved properties are compared to similar quantities derived from data over the continental United States of America (USA) to examine the differences between contrails formed over marine and continental areas. They are also compared to the theoretical results. Preliminary statistics are presented.

[5] *Corresponding author:* Patrick Minnis, MS 420, NASA Langley Research Center, Hampton, VA, USA 23681. Email: p.minnis@nasa.gov

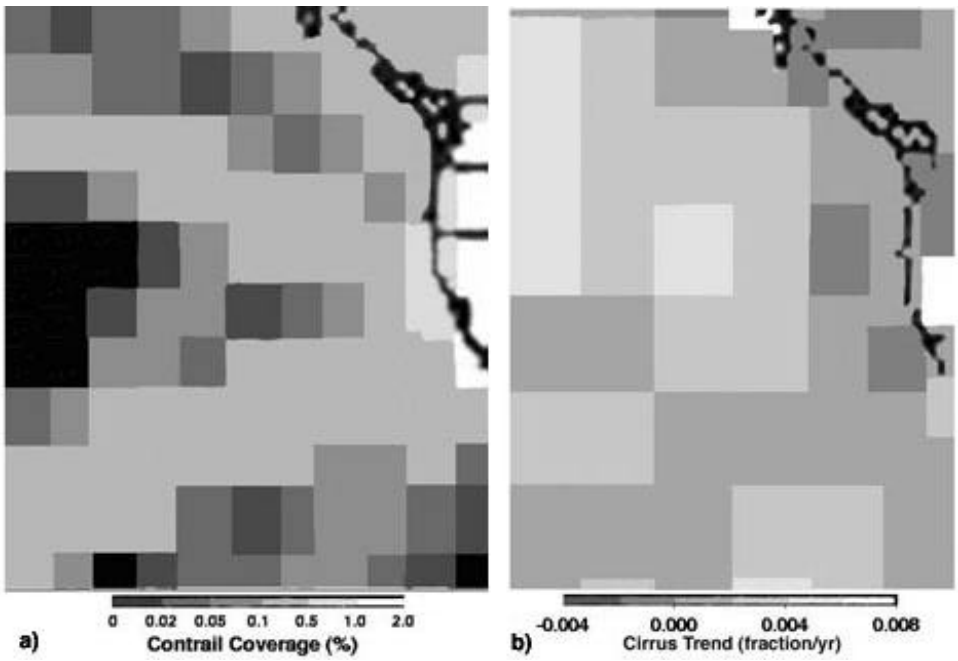

Figure 1: Theoretical linear contrail coverage in 1992 (a) and trend in surface-observed 1971-1996 cirrus coverage (a), and

2 DATA AND ANALYSIS

Advanced Very High Resolution Radiometers (AVHRR) have been taking 1-km multispectral data from the NOAA satellites since the 1980's, but most of the archived and real-time data over the broad ocean areas are for the 4-km Global Area Coverage (GAC) dataset. The NASA Earth Observing System satellites, *Terra* and *Aqua*, have been operating since March 2000 and August 2002, respectively. Each carries the Moderate Resolution Imaging Spectroradiometer (MODIS) that takes and archives multispectral data globally at resolutions from 0.25 to 1 km. Figure 2 shows examples of large contrails evident in the NOAA-16 AVHRR GAC imagery off the coast of California. Some of the trails exceed 1000 km in length and 20 km in width and they are evident in both the channel-4 infrared (IR, 11 μm) image (Fig. 2a) and, in Figure 2a, the 11-12 μm brightness temperature difference (T4-T5), a parameter commonly used to differentiate contrails from cirrus clouds. Such lengthy, fat contrails are not uncommon as seen in Fig. 3. The contrails in the NOAA-15 T4-T5 image (Fig. 3a) are from jets approaching California from the northwest while those in the 1-km MODIS image (Fig. 3b) are from planes approaching southern California from the southwest.

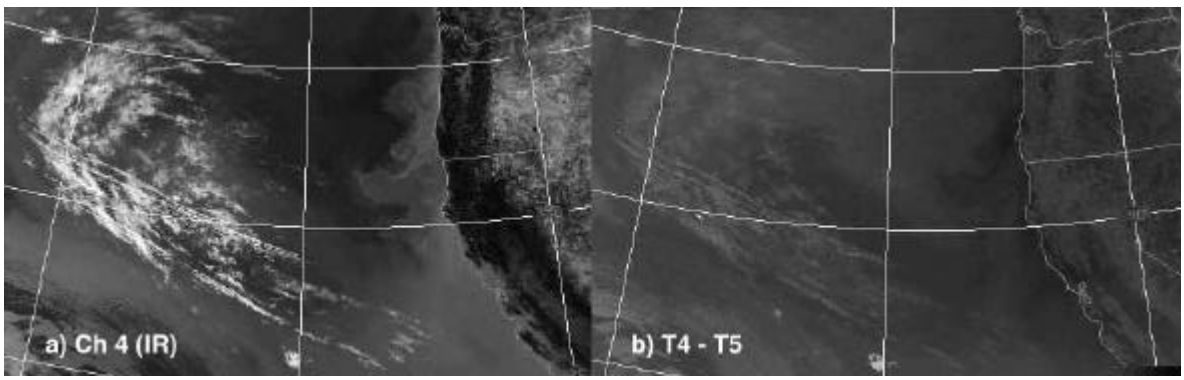

Figure 2: NOAA-16 AVHRR imagery at 1056 UTC, 13 August 2002: Infrared brightness temperature (a) and channel 4-5 brightness temperature difference.

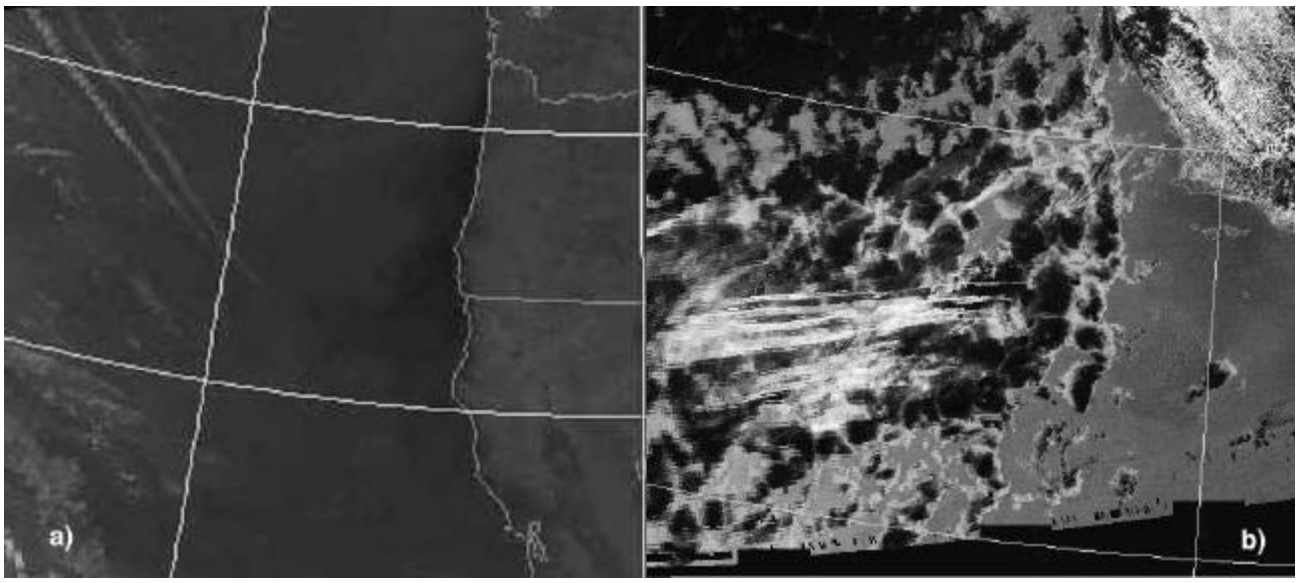

Figure 3: Contrails in the northeastern Pacific. (a) NOAA-15 AVHRR GAC T4-T5, 0230 UTC, 14 August 2002. (b) Aqua MODIS 1-km, 2054 UTC, 3 May 2003, T31-T32.

To quantify the contrail properties over the North Pacific, an automated algorithm (Mannstein et al. 1999) can be applied to 1-km AVHRR data from *NOAA-16* and to MODIS data from *Terra* and *Aqua* to derive contrail areal coverage. Contrail optical depth is computed with the method of Meyer et al. (2002) assuming that the contrail temperature is 224 K and that the contrail emissivity varies with optical depth (*OD*) according to the model of Minnis et al. (1993) for small ice crystals. Contrail longwave radiative forcing (CLRF) and the background temperature were computed using the methods of Palikonda et al. (2002, 2003). The initial analyses are performed on 1-km NOAA-16 AVHRR data taken from afternoon orbits during August 2002 and February 2003. The domain extends from 25°N to 55°N and from 120°W to 150°W corresponding to the plots in Figure 1.

3 RESULTS AND DISCUSSION

Figure 4 shows the distribution of contrail coverage over the domain for the two months. It is obvious that the derived contrail coverage in February (Fig. 4b) exceeds that found in August (Fig. 4a). During August, the greatest contrail coverage occurred around 47°N, 142°W with a secondary maximum near the west-southwest approach to San Francisco. Minimum coverage is seen in the southwestern corner of the domain, off the Oregon coast and inland. A general increase in contrail coverage during February is accompanied by a shift in the areal maximum to 42°N, 147°W. The southwestern corner remained relatively free of contrails. However, the contrail coverage is greatly increased over all of the approaches to the west coast cities. Overall, the mean contrail amounts during August 2002 and February 2003 are 0.51 and 0.67%, respectively.

The corresponding mean contrail optical depths for the domain are 0.27 and 0.26. The mean CLRF for both months is 0.09 Wm^{-2}. However, during February the unit or normalized CLRF (NCLRF) is 13.5 Wm^{-2} compared to 17.4 Wm^{-2} during August. The frequency distributions of *OD* and NCLRF are plotted in Figure 5. Optical depths vary according to a slightly skewed Gaussian distribution with a mode value around 0.20. The NCLRF distribution is highly skewed with a mode near 8 Wm^{-2}. This domain includes inland desert areas in Oregon and Washington that can become very warm during the afternoon even during winter. The large variability in NCLRF arises from the large range in background radiating temperatures. Contrails mixed with other cirrus clouds will tend to have small values of NCLRF while over clear areas NCLRF will be much larger, especially over land during the afternoon.

The contrail coverage values for both months are roughly twice the annual mean (0.30) from the results of Sausen et al. (1998). This difference could be due to a number of factors including the restricted sampling of the NOAA-16 afternoon orbit, a potential bias in the satellite retrievals (e.g.,

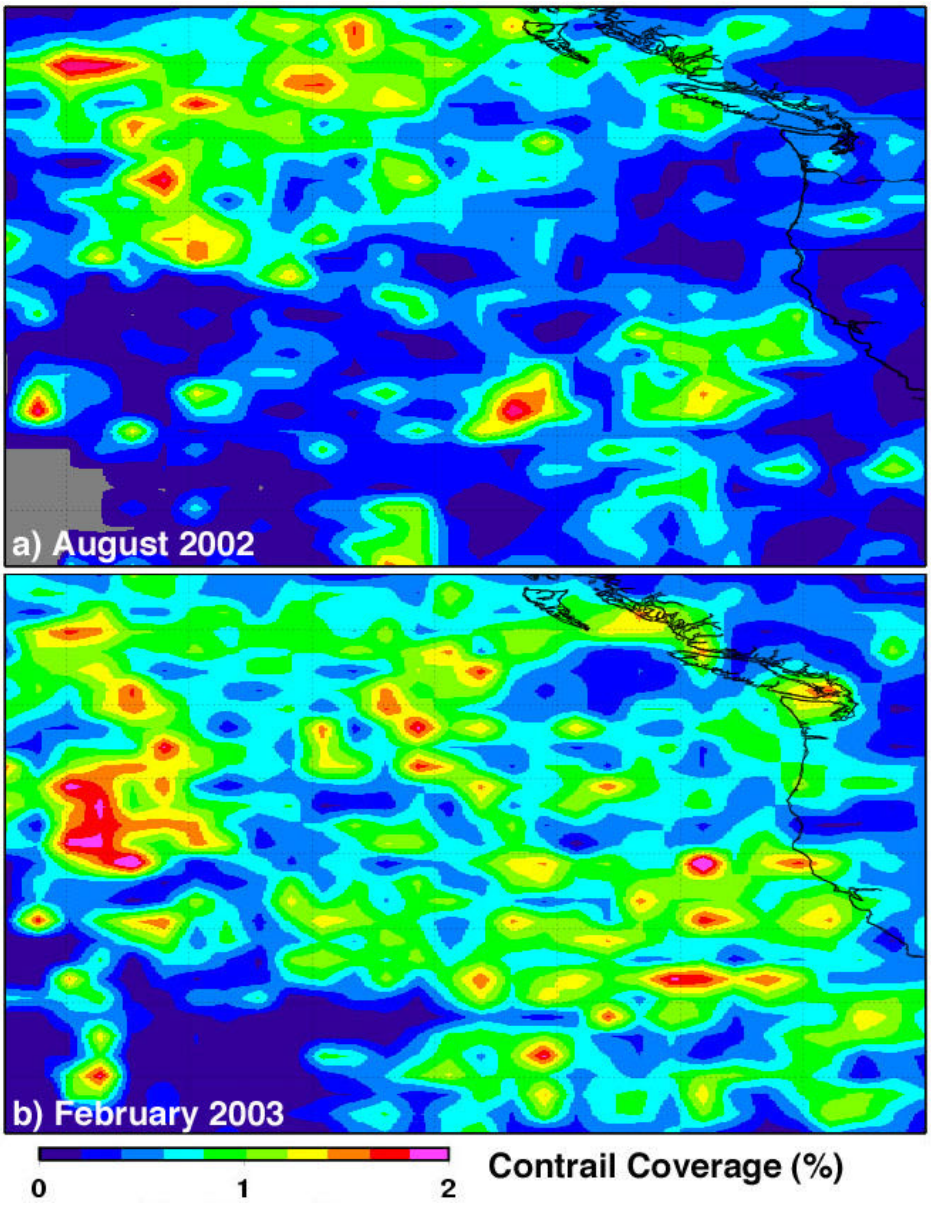

Figure 4. Mean contrail coverage derived from afternoon (1430 LT) NOAA-16 AVHRR data.

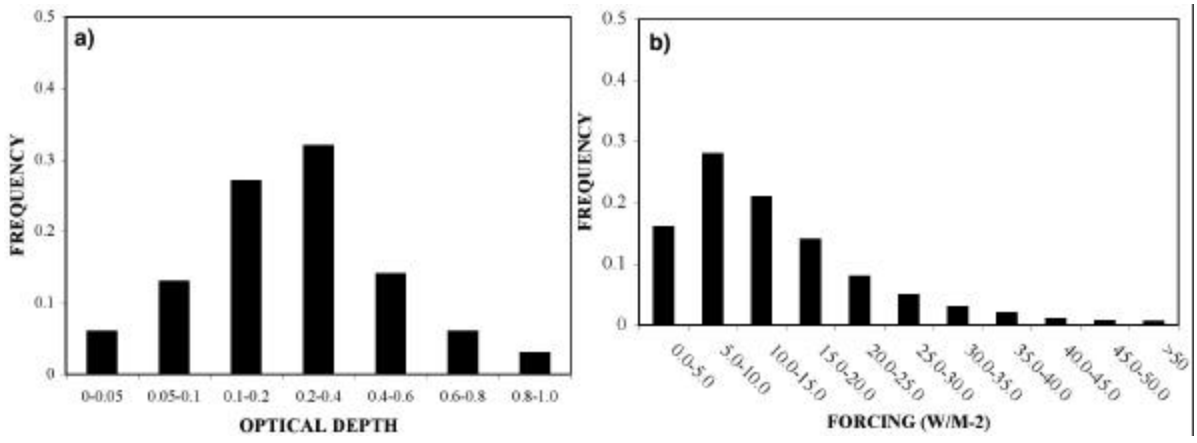

Figure 5. Frequency distributions of (a) contrail optical depth and (b) unit CLRF during February 2003.

Palikonda et al. 2003), an increase in trans-Pacific air traffic since 1992, differences in the upper tropospheric humidity between the model and the actual atmosphere, and a variety of other reasons. From the theoretical calculations of Ponater et al. (2002), it appears that summertime contrail coverage over the area should be larger than that during winter. This discrepancy with the current observations may arise form the same sources causing the differences in absolute contrail coverage. For instance, during winter, cirrus clouds are more abundant over the domain due to the more frequent passage of baroclinic disturbances. The opportunity for mistaking cirrus clouds during winter is enhanced at the same time as the potential for forming contrails. The overall effect may be that the overestimate of contrail coverage from the satellite analysis is greater during winter than during summer.

The afternoon NOAA-16 sampling may not be representative of the air traffic over the Pacific. While the air traffic over the USA is nearly constant for half of the day (Garber et al. 2003), scheduling of transoceanic flights differs from transcontinental traffic. Thus, the number of flights may be greater or less at other hours than at 1430 LT. Additional satellite overpass times should be analyzed.

The wwestern maxima in contrail coverage (Fig. 4) are generally consistent with the maximum in cirrus trend (Fig. 1b) although the theoretical contrail coverage minimum extends into the same area. The flight tracks used in the Sausen et al. (1998) study are highly idealized and may not accurately represent the actual distribution of flight locations during the 2002-2003 period. Given the greater number of contrails in the northwestern part of the domain, it is likely that the conditions for contrail and cirrus formation are most favourable in that area. Thus, the errors in contrail detection may be greater in the same region. This issue requires further study.

The contrail optical depth distributions and mean values are nearly identical to those derived over the USA by Palikonda et al. (2003). The means are almost twice the magnitude found over Europe by Meyer et al. (2002) and estimated by Ponater et al. (2002) from theoretical calculations. The differences again may be related to mistaken cirrus clouds that are deeper than the average contrail or to an underestimate of contrail depth by the theoretical models. The February NCLRF mean is 5 Wm-2 greater than the wintertime mean for NOAA-16 results over the USA while the August NCLRF is 2 Wm-2 less than the corresponding USA summertime mean (Palikonda et al. 2003). This seasonal difference in the CLRF is likely due to the relatively stable background temperatures over the ocean. Over land, the contrast between the contrail and surface temperatures is much greater in summer than in winter.

4 CONCLUDING REMARKS

The results presented here constitute the first objective analysis of linear contrails over the western North Pacific. Both contrail coverage and optical depth are twice the annual average derived from theoretical considerations. Contrail longwave radiative forcing is much greater than computed theoretically. However, the results should be considered preliminary because no error analyses have been performed. Furthermore, the data were taken at only one time of day and may not represent the entire daily cycle.

This study has just begun. In the future, detailed error analyses will be performed to optimize the accuracy of the methodology for each satellite separately. A larger dataset including MODIS data and other NOAA satellites will be analyzed to determine the annual cycle and provide results that include all times of day. Shortwave radiative forcing will also be estimated for each retrieval to determine the net radiative forcing for these contrails. The results will be compared with the model-predicted temperature and humidity conditions to help improve the parameterization of contrails in climate models so that a more accurate assessment of contrail effects can be computed for the northwestern Pacific Ocean.

REFERENCES

Garber, D. P., P. Minnis, and P. K. Costulis, 2003: A USA commercial flight track database for upper tropospheric aircraft emission studies. *Proc. European Conf. Aviation, Atmosphere, and Climate*, Friedrichshafen at Lake Constance, Germany, June 30 - July 3.

Mannstein, H., R. Meyer, and P. Wendling, 1999: Operational detection of contrails from NOAA AVHRR data. *Int. J. Remote Sens.*, 20, 1641-1660.

Meyer, R., H. Mannstein, R. Meerkötter, U. Schumann, and P. Wendling, 2002: Regional radiative forcing by line-shaped contrails derived from satellite data. *J. Geophys. Res.* 107, D10 10.1029/2001JD000426.

Minnis, P., J. K. Ayers, R. Palikonda, and D. Phan, 2003: Contrails, cirrus trends, and climate. *J. Climate*, submitted.

Minnis, P., Y. Takano, and K.-N. Liou, 1993.: Inference of cirrus cloud properties using satellite-observed visible and infrared radiances, Part I: Parameterization of radiance fields. *J. Atmos. Sci*., 50, 1279-1304.

Palikonda, R., P. Minnis, P. K. Costulis, and D. P. Duda, 2002: Contrail climatology over the USA from MODIS and AVHRR data. *Proc. 10th Conf. on Aviation, Range, and Aerospace Meteorology*, Portland, OR, May 13-16, J9-J12.

Palikonda, R., D. N. Phan, and P. Minnis, 2002: Contrail coverage over the USA from MODIS and AVHRR data. *Proc. European Conf. Aviation, Atmosphere, and Climate*, Friedrichshafen at Lake Constance, Germany, June 30 - July 3.

Ponater, M., S. Marquart, and R. Sausen, 2002: Contrails in a comprehensive global climate model: parameterisation and radiative forcing results. *J. Geophys. Res*., 107, 10.1029/2001JD000429.

Sausen, R., K. Gierens, M. Ponater, M. and U. Schumann, 1998: A diagnostic study of the global coverage by contrails, part I, present day climate. *Theor. Appl. Climatol.* 61, 127-141.

Survey of Cirrus Properties from Satellite Retrievals Using TOVS and AVHRR Observations

C. J. Stubenrauch *
C.N.R.S. – IPSL Laboratoire de Météorologie Dynamique (LMD), Ecole Polytechnique, Palaiseau, France

R. Meerkötter
DLR-Institut für Physik der Atmosphäre Oberpfaffenhofen, Germany

Keywords: satellite observations, cirrus, high clouds, time series, AVHRR, TOVS, ISCCP, INCA

ABSTRACT: The TOVS Path-B dataset provides atmospheric temperature and water vapor profiles as well as cloud and surface properties over the globe, at a spatial resolution of 1° latitude x 1° longitude. Their relatively high spectral resolution yields reliable cirrus properties, day and night. Over Europe, observations of the AVHRR instrument have been analysed by the APOLLO Processing scheme to identify cloud types, at a spatial resolution of 1 km. ISCCP offers a global cloud climatology with a good diurnal sampling. We present times series of thin and thick high cloud amount over this area with increasing air traffic. A more detailed study, using TOVS Path-B data, compares cirrus and atmospheric properties in the northern and southern hemisphere midlatitudes to investigate further the impact of anthropogenic influence on cirrus clouds.

1 INTRODUCTION

The increase in anthropogenic aerosols and in air traffic have led to theoretical and observational investigations of the impact on the formation of cirrus clouds. Contrails form when the hot and humid exhaust gases from the combustion of fuels by an aircraft mix with the ambient, cold atmosphere (Schumann, 1996). Their persistence depends on upper tropospheric humidity and temperature (Sausen et al., 1998, Kästner et al., 1999), since the aircraft emissions trigger the formation of additional clouds from natural water vapour present in the atmosphere. Over Europe and the USA, conditions for formation of contrails are less favourable in summer.

Only satellite observations are capable to give a continuous survey of the state of the atmosphere over the whole globe. Long time-series (twenty years) of reflected, scattered and emitted radiation from the earth's surface, atmosphere and clouds are available from imagers, using atmospheric window channels, and from vertical sounders, using CO_2 and H_2O sensitive channels. These measured radiances are transformed into cloud properties by inversion algorithms, relying on radiative transfer models. We use these satellite data to investigate the impact of air traffic and anthropogenic aerosols on the evolution of cirrus clouds, in two example studies: first we compare time series of high cloud amount over Europe, obtained by different satellite instruments and inversion algorithms, and second we analyse correlations between cirrus bulk microphysical properties and relative humidity, contrasting two midlatitude regions, one in the northern hemisphere (polluted) and the other in the southern hemisphere (pristine).

2 DATASETS

2.1 *Atmospheric properties from TOVS Path-B*

The TIROS-N Operational Vertical Sounder (TOVS) instruments aboard the NOAA Polar Orbiting Environmental Satellites consist, in particular, of the High resolution Infrared Radiation Sounder (HIRS/2) with 19 infrared (IR) spectral channels between 3.7 and 15 μm and one visible channel

* *Corresponding author:* Claudia J. Stubenrauch, C.N.R.S. Laboratoire de Météorologie Dynamique, Ecole Polytechnique, 91128 Palaiseau cedex, France. Email: stubenrauch@lmd.polytechnique.fr

and the Microwave Sounding Unit (MSU) with four microwave channels around 5 mm. At present, the TOVS Path-B dataset (Scott et al., 1999) provides eight years (1987-1995) of atmospheric temperature profiles (in 9 layers) and water vapour profiles (in 4 layers) as well as cloud and surface properties at a spatial resolution of 1°. So far, NOAA-10, NOAA-11 and NOAA-12 data have been processed at LMD, and results are being extended from 1979 until now.

Clouds are detected at HIRS spatial resolution (17 km at nadir) by a succession of threshold tests, which depend on the simultaneous MSU radiance measurements that probe through the clouds. To insure more coherence with the MSU spatial resolution, the HIRS radiances are averaged separately over clear pixels and over cloudy pixels over 100 km x 100 km regions. Average cloud-top pressure, p_{cld}, and effective cloud emissivity, $N\varepsilon_{cld}$, over cloudy pixels are obtained from four radiances in the 15 μm CO_2 absorption band (with peak responses from 400 to 900 hPa levels in the atmosphere) and one in the 11 μm IR atmospheric window by minimizing a weighted χ^2 (Stubenrauch et al., 1999).

Table 1 gives an overview of total and high cloud amount over the globe and selected regions, averaged from 1987 to 1995, as obtained from TOVS Path-B and ISCCP (Rossow and Schiffer, 1999). ISCCP D2 data provide monthly averages and cloud type statistics over 2.5 ° latitude x 2.5° longitude, from 3-hourly observations of imagers aboard geostationary and polar satellite imagers. The TOVS Path-B averages shown in Table 1 are from NOAA-10/12 data, with local observation time at 7h30 am and 7h30 pm. High clouds are defined by $p_{cld} < 440$ hPa, and are divided into three types, according to $N\varepsilon_{cld}$ (> 0.95, 0.95-0.5 and < 0.5) by TOVS and visible optical thickness, τ_{cld}, (> 23, 3.6–23 and < 3.6) by ISCCP, as deep convection, cirrus and thin cirrus. About 70% of the Earth's surface is covered by clouds, with about 10% more cloudiness over ocean than over land. The cover of high clouds is about 30%, with a maximum of about 47% in the tropics. Due to their relatively high spectral resolution, IR vertical sounders are more sensitive to cirrus than imagers; therefore TOVS Path-B indicates 8% more cirrus over the globe and up to 20% more cirrus in the tropics than ISCCP.

In the case of clear sky and thin clouds, the TOVS Path-B also provides profiles of atmospheric water vapour (Chaboureau et al., 1998). For the analysis in section 4, we estimate the upper tropospheric relative humidity (RH) from the TOVS Path-B water vapour columns between 500 and 300 hPa, and above 300 hPa, retrieved in the case of clear sky and thin cirrus ($N\varepsilon < 0.5$). Upper tropospheric relative humidity is the ratio of partial water vapour pressure and saturation vapour pressure, with respect to ice. Since the TOVS atmospheric profiles have a rather low vertical resolution and the saturation vapour pressure strongly depends on atmospheric temperature, we use the atmospheric temperature profile (with a vertical resolution of 30 levels in the troposphere) of the Thermodynamic Initial Guess Retrieval (TIGR) data set (Chevallier et al., 1998) closest to the observed atmospheric condition to compute the saturation vapour pressure and integrate it then over the columns. The average relative humidity around 300 hPa is then the mean of the relative humidity of these two columns. This is a rough but nevertheless gives estimate useful information on the state of the atmosphere.Within the frame of the EU project CIRAMOSA, we retrieve mean effective ice crystal diameters, D_e, for large-scale semitransparent cirrus clouds (visible optical thickness between 0.7 and 3.8), using spectral cirrus emissivity differences between 11 and 8 μm (Rädel et al., 2003). This method is sensitive to diameters up to 80 μm. Ice water path (IWP) is then determined from the cirrus emissivity at 11 μm and the retrieved D_e.

Table 1. 8-year average cloud type amounts from TOVS Path-B and ISCCP (italic), over the globe, northern hemisphere and southern hemisphere midlatitudes (30°N-60°N, 30°S-60°S) and tropics (20°N-20°S).

Cloud type amounts (%)	global		ocean		land	
all	*73*	*67*	*74*	*71*	*69*	*58*
Deep convection	*2.4*	*2.8*	*1.9*	*2.8*	*3.5*	*2.7*
Cirrus + thin cirrus	*27.3*	*19.1*	*26.9*	*18.0*	*27.8*	*21.7*
Cloud type amounts (%)	NH midlatitudes		tropics		SH midlatitudes	
Deep convection	*3.0*	*3.3*	*3.5*	*2.5*	*2.4*	*3.0*
Cirrus + thin cirrus	*27.7*	*20.3*	*44.8*	*24.9*	*21.8*	*16.5*

2.2 *Cloud identification over Europe from AVHRR/APOLLO*

AVHRR data were analysed using the AVHRR Processing scheme Over cLouds, Land and Ocean (APOLLO), described by Kriebel et al. (2003). APOLLO makes use of all five spectral channels of the NOAA/AVHRR instrument during daytime and discretizes the data into four groups called cloud-free, fully cloudy, partially cloudy and snow/ice. In a next step, physical properties are derived. Within APOLLO, clouds are assigned to three layers according to their top temperatures. The layer boundaries are set to 700 hPa and 400 hPa and associated temperatures are derived from standard atmospheres. Each fully cloudy pixel is identified as thick or thin cloud, according to its brightness temperatures at 11 and 12 μm and, during daytime, its reflectances at 0.6 and 0.9 μm. Reflectances below a certain threshold identify thin clouds, with τ_{cld} typically less than 5. Thin clouds are taken as ice clouds, i.e. cirrus. Cloud cover of the partially cloudy pixels is derived from reflectances and temperatures of their cloud free and cloudy parts. Assuming horizontal homogeneity, these quantities are taken from the nearest fully cloudy and cloud free pixels. During daytime, cloud optical depth, liquid/ice water path and emissivity are calculated for each fully cloudy pixel by means of parameterization schemes that are based on the reflectance at 0.6 μm.

APOLLO is currently used to generate a high resolution cloud climatology (0.01° x 0.0125° in latitude and longitude) for the entire region of Europe (34°N-72°N, 11°W-32°E). This European cloud climatology (ECC) presently covers a period of 13 years from 1990 to 2002. It should be noted that the cloud products are derived from data of the noon overpasses of the satellites NOAA-11 (1990-1994), NOAA-14 (1995-2001), and NOAA-16 (2002). The generation of ECC products is an ongoing process, but it is also planned to extend the ECC further into the past, i.e. to the years before 1990.

3 HIGH CLOUD AMOUNT AND ITS TEMPORAL VARIABILITY

To study the feasibility of a trend analysis, we compare in Figure 1 the time-series of high thin and thick cloud amount of these different satellite cloud data sets over Europe. ISCCP data cover three-hourly observations, TOVS Path-B data cover observations at 7h30 am and 7h30 pm local time, and AVHRR/APOLLO data are derived from observations around 2h pm local time. A study of six-hourly TOVS Path-B data (from NOAA-10/-12 and NOAA-11 satellites) has shown that high thin cloud amount over Europe increases from about 7% in early morning to 12% in the afternoon. Whereas ISCCP and TOVS Path-B high clouds are defined by $p_{cld} < 440$ hPa, the AVHRR/APOLLO criterion is stricter: $p_{cld} < 400$ hPa. Also, the distinction between thin and thick clouds of these three datasets is not the same: TOVS Path-B separates thin cirrus at $\tau_{cld} < 1.5$, ISCCP at $\tau_{cld} < 3.6$ and AVHRR/APOLLO at $\tau_{cld} < 5$. From Figure 1 we conclude the following:

- The overall high cloud amount over Europe is about 23% / 19% / 13% with about 10% / 10% / 4% thin cirrus, according to TOVS Path-B, ISCCP and AVHRR/APOLLO respectively. Differences between these values can be explained by different sensitivity to thin cirrus, slightly different definitions of cloud types and different observation times.
- Interannual variability is the lowest for TOVS Path-B high clouds. Thin cirrus amount has a minimum of about 7% in winter and a maximum of about 13% in summer, the difference of seasonal minima and maxima is larger for thicker cirrus, with a minimum of about 6% in summer and maxima in early and late winter of about 16%. Exceptions of this behaviour are the winter of 1988/89 with about 5% less thick cirrus and the period from autumn 1989 to autumn 1990 with no seasonal change in thin cirrus. This could be related to the North Atlantic Oscillation (NAO): Before this period the NAO index is for several months negative and then changes to strong positive values again for several months positive. By observing a similar period in behaviour of the NAO index in 1993/94, we discover also a similar pattern of thin cirrus variability in Figure 1.
- Considering the ISCCP times-series, seasonal variations of thick cirrus are also of about 5%, with maxima in winter and minima in summer. The winter peaks are however narrower than those of the TOVS Path-B data set. The time-series of thick cirrus seems to be quite stable, with slightly smaller maxima in winters of 1988/89, 1991/92 and 1998/99. Thin cirrus amount shows a quite different behaviour: It is difficult to observe a systematic seasonal cycle over the whole data period of 20 years. However, one observes three different cycles characterized by a drop and then

a continuous increase of thin cirrus amount and an increase of its seasonal variability. The beginnings of these cycles coincide with changes of the NOAA afternoon satellites in 1984/85, 1988/89 and 1994/95. It is well known that all afternoon satellites continuously drifted during their operation by at least two hours in their observation time (NOAA-11 even four hours) from early afternoon to late afternoon.

- Thick high cloud amount of AVHRR/APOLLO and ISCCP compares on average very well. Seasonal minima and maxima agree well with TOVS Path-B data from NOAA-11 afternoon observations (shown on the poster). Exceptions are the winter minima in 1990/91 and 1991/92. Due to the drifting overpass times of the NOAA afternoon satellites the solar zenith angles increase at the time of cloud probing within the periods of NOAA-11 (1990-1994) and NOAA-14 (1995-2001). The change in the anisotropic bidirectional reflection distribution function of thin clouds causes therefore an increase of the signals in the visible AVHRR channels. Although APOLLO accounts for an anisotropy correction of measured signals to a certain degree, there is still a continuous reduction in the observed coverage of thin clouds during each satellite period. Therefore, thin high cloud amount of AVHRR/APOLLO is only shown for June and July, the months causing minimum anisotropy effects due to smaller solar zenith angles. The abrupt increases in thin cloud amount result during satellites changes.

Another possibility to study the anthropogenic impact on cirrus clouds is to contrast northern and southern hemisphere (NH / SH). Figure 2 presents a time-series of amount of cumulonimbus, cirrus and thin cirrus as obtained from TOVS Path-B, for NH midlatitudes and SH midlatitudes. Both hemispheres, are covered by about 15% cirrus, but the amount of thin cirrus is higher in the NH (10% compared to 7.5% in the SH). It is also interesting to note that in the NH midlatitudes thin cirrus have a pronounced seasonal cycle, whereas in the SH midlatitudes cirrus have a pronounced seasonal cycle. However, during the period of eight years, these high cloud amounts are quite stable. If there is a trend to see, it would be a slight decrease of cirrus, in both hemispheres.

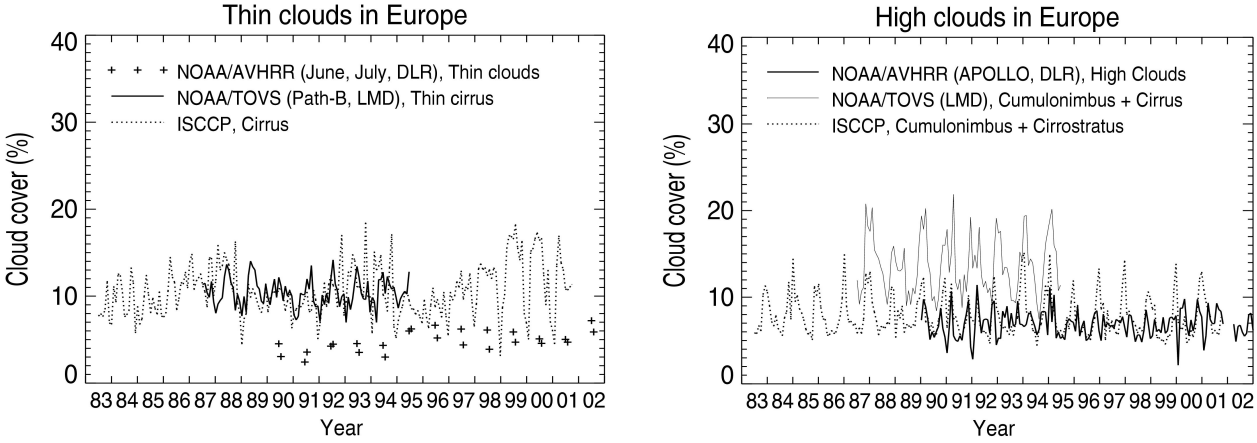

Figure 1. Time series of cloud amount of thin high clouds (left) and thick high clouds (right) over Europe, retrieved from observations of different satellite instruments and by different inversion algorithms.

4 CIRRUS PROPERTIES IN NORTHERN AND SOUTHERN HEMISPHERE (INCA REGIONS)

A second example of using satellite data to study the impact of anthropogenic influence on cirrus clouds is given by an analysis of correlations between cirrus properties and surrounding atmospheric conditions. We have selected the regions which have been thoroughly studied in the frame of the European project INCA (INterhemispheric differences in Cirrus properties from Anthropogenic emission), with measurement campaigns in Apr/May 2000 in the southern hemisphere (53°S) and in Sep/Oct 2000 in the northern hemisphere (55°N).

Figure 3 presents upper tropospheric relative humidity distributions in the case of clear sky, sky with very thin cirrus ($N\varepsilon<0.3$) and sky with thin cirrus ($0.3<N\varepsilon<0.5$), separately for the NH and SH INCA regions, during autumn. In the case of clear sky, all these distributions follow an exponential law as observed in (Gierens et al., 1999). However, one observes a systematic difference in the distributions for very thin cirrus between the NH and SH INCA regions: In the SH INCA region, with few upper tropospheric aerosols, there are more situations with high relative humidity linked to cirrus than in the NH INCA region, chosen for high air traffic. These observations also agree with in-situ measurements of Overlaz et al. (2002).

In Figure 4 we compare correlations between bulk microphysical properties of thin cirrus ($0.3<N\varepsilon<0.4$) and upper tropospheric humidity in the NH and SH INCA regions, again separately during autumn. In general, D_e and IWP are slightly larger in the NH INCA region and their increase with relative humidity is slightly stronger than in the SH INCA region. However, D_e increases with IWP in the same manner in both regions, for situations with RH < 70% and RH > 70%. To understand the differences in cirrus bulk microphysical properties between these two regions, one has to compare further the dynamical situation of the atmosphere in both hemispheres.

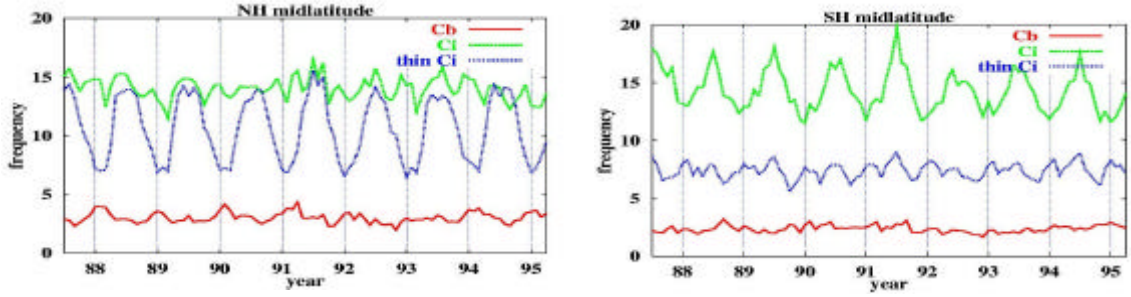

Figure 2. Time series of high cloud amount, separately for opaque, cirrus and thin cirrus, over NH midlatitudes (left) and over SH midlatitudes (right), derived from TOVS Path-B data, with observation time at 7h30 am and 7h30 pm.

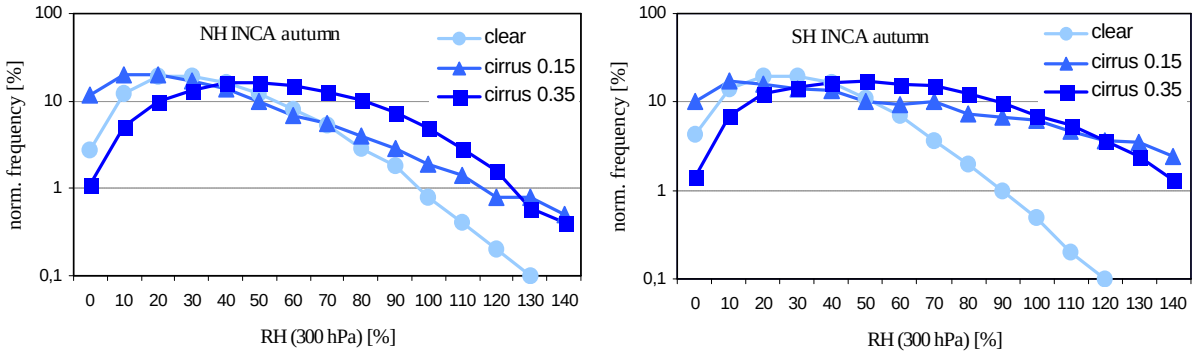

Figure 3: Upper troposphere relative humidity distributions of clear sky, sky with very thin cirrus and sky with thin cirrus, during autumn, in the INCA regions of the northern hemisphere (left) and of the southern hemisphere (right). Data are 8- year averages from TOVS-Path-B.

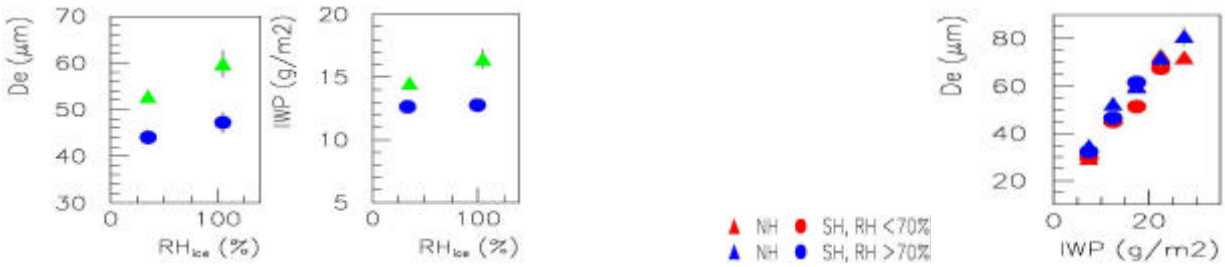

Figure 4: Right: D_e and IWP of thin cirrus for regions with low and high relative humidity, during autumn, in the INCA regions of NH (Δ) and of SH (O). Left: De as function of IWP for all situations. Data are 4-year averages from TOVS-Path-B.

5 CONCLUSIONS

We have investigated the feasibility of a trend analysis of cirrus amount by comparing three different satellite data sets over Europe: TOVS Path-B, ISCCP and AVHRR/APOLLO. These time series of thick and thin cirrus amount do not show any significant trend over Europe. Thin and thick cirrus amounts from TOVS Path-B, which should be the most reliable, are quite stable over an 8-year period, also by comparing NH and SH midlatitudes. Interannual variability of seasonal behaviour is possibly be related to differences in NAO. Cyclic temporal variations in amount and seasonal variability of thin cirrus amount from ISCCP and AVHRR/APOLLO can be possibly explained by satellite drifts over their observation periods (up to four hours). We want to conclude that trend analyses have to be undertaken with great care, especially when seasonal variations are quite large. Only by removing effects related to technical problems such as satellite drifts, missing data, calibration etc. one can investigate very small trends.

By comparing correlations between atmospheric humidity and cirrus properties in NH and SH INCA regions, we observe that very thin cirrus in the SH are related to significantly broader upper troposperic relative humidity distributions than those in the NH. Whereas D_e and IWP of semi-transparent cirrus are slightly larger on average in the NH than in the SH, correlations between them are the same in both hemispheres. In a next step, atmospheric winds have to be analyzed in these regions.

6 ACKNOWLEDGEMENTS

The authors want to thank K. Gierens and A. Chédin for interesting discussions on relative humidity and C. König, H. Mannstein, and G. Gesell for their support in processing the NOAA/AVHRR data.

REFERENCES

Chaboureau, J. P., A. Chédin, and N. A. Scott, 1998: Remote sensing of the vertical distribution of atmospheric water vapor from the TOVS observations: Method and validation. *J. Geophys. Res. 103*, 8743-8752.

Chevallier, F., F. Chéruy, N. A. Scott, and A. Chédin, 1998: A neural network approach for a fast and accurate computation of a longwave radiative budget. *J. Appl. Meteor. 37*, 1385-1397.

Gierens, K., U. Schumann, M. Helten, H. Smit, and A. Marenco, 1999: A distribution law for relative humidity in the upper troposphere and lower stratosphere derived from three years of MOZAIC measurements. *Ann. Geophysicae 17*, 1218-1226.

Kästner, M. R. Meyer, and P. Wendling, 1999: Influence of weather conditions on the distribution of persistent contrails. *Meteorol. Appl. 6*, 261-271.

Kriebel, K.T., G. Gesell, M. Kästner, and H. Mannstein, 2003: The cloud analysis tool APOLLO: improvements and validations. *Int. J. Remote Sensing 24*, 2389-2408.

Ovarlez, J., J.-F. Gayet, K. Gierens, J. Strom, H. Ovarlez, F. Auriol, R. Busen, and UL Schumann, 2002: Water vapour measurements inside cirrus clouds in Northern and Southern hemispheres during INCA. *Geophys. Res. Lett. 29*, 10.1029/2001GL014440.

Rädel, G., C. J. Stubenrauch, R. Holz, and D. L. Mitchell, 2003: Retrieval of Effective Ice Crystal Size in the Infrared : Sensitivity Study and Global Measurements from the TIROS-N Operational Vertical Sounder. *J. Geophys. Res. 108*, 10.1029/2002JD002801.

Rossow, W. B., and R. A. Schiffer, 1999. Advances in understanding clouds from ISCCP. *Bull. Amer. Meteor. Soc. 80*, 2261-2288.

Sausen, R., K. Gierens, M. Ponater, and U. Schumann, 1998: A Diagnostic Study of the Global Distribution of Contrails. Part I: Present Day Climate. *Theor. Appl. Climatol. 61*, 127-141.

Schumann, U., 1996: On conditions for contrail formation from aircraft exhausts. *Meteorol. Z. 5*, 2-23.

Scott, N. A., A. Chédin, R. Armante, J. Francis, C. J. Stubenrauch, J.-P. Chaboureau, F. Chevallier, C. Claud, and F. Chéruy, 1999: Characteristics of the TOVS Pathfinder Path-B Dataset. *Bull. Amer. Meteor. Soc. 80*, 2679-2701.

Stubenrauch, C. J., A. Chédin, R. Armante, and N. A. Scott, 1999: Clouds as seen by Infrared Sounders (3I) and Imagers (ISCCP): Part II) A New Approach for Cloud Parameter Determination in the 3I Algorithms. *J. Climate 12*, 2214-2223.

Comparison of Cirrus Cloud Properties in the Northern and Southern Hemisphere on the Basis of Lidar Measurements.

F. Immler, O. Schrems
Alfred-Wegener-Institut für Polar und Meeresforschung , Bremerhaven, Germany, fimmler@awi-bremerhaven.de

Keywords: Cirrus, Lidar

ABSTRACT: Cirrus cloud measurements have been performed during the INCA field campaigns in Punta Arenas/Chile (53.12°S, 70.88°W) and in Prestwick/Scotland (55.51°N, 4.60°W) in each hemisphere's fall in the year 2000. From lidar backscatter profiles at 532 nm and 355 nm the optical depth (OD) of the clouds is retrieved as well as base and top altitude of the clouds, the color index and the depolarization. Cloud layers with optical depths covering more than 3 orders of magnitude have been detected by the lidar, with a high share (35%) of subvisual cirrus at both sites. Differences in the results from the southern and the northern hemisphere are found in the lidar ratio and the depolarization behavior. While there is a large natural variability in cirrus properties, our results indicate a tendency towards bigger particles and columns in the southern hemisphere compared to smaller particles and small crystal plates in the northern hemisphere.

1 INTRODUCTION

The Mobile Aerosol Raman Lidar (MARL) of the Alfred Wegener Institute is a mobile backscatter lidar which was already operated during several field campaigns at various locations as well as aboard the German research vessel Polarstern to measure aerosol and clouds in the upper troposphere and lower stratosphere. In 2000, two field-experiments have been conducted within the European INCA 2000-project (Interhemispheric differences in cirrus cloud properties by anthropogenic emissions). The first one took place in the midlatitudes of the southern hemisphere (Punta Arenas/Chile, 53.12°S, 70.88°W) and the second campaign followed in September 2000 in Prestwick/Scotland (55.51°N, 4.60°W). The main objective of these investigations was to collect Lidar data of cirrus clouds from clean (Punta Arenas) and polluted (Prestwick) areas and to analyze this data in respect to differences that might be caused by air traffic or other anthropogenic emissions. During the four weeks of the campaigns, about 80 hours of Lidar measurements were gathered at each location, covering different types of cirrus clouds as well as background aerosols. A comparison of the two datasets reveals similarities as well as differences in the measured cirrus cloud properties.

2 CLOUD DETECTION BY LIDAR

MARL (Mobile Aerosol Raman Lidar) is a backscatter Lidar based on a linear polarized Nd:YAG Laser with 30 Hz repetition rate and 200 mJ pulse energy (@532 nm). The detection unit uses a 1.1 m cassegrain telescope and a multichannel polychromator which detects backscattered light at 532 nm and 355 nm, both separated in parallel and perpendicular polarization (with respect to the lasers linear polarisation). Furthermore, the system detects light backscattered from N_2 molecules with a Raman shift (607 and 387nm). The Raman signals allow the direct measurement of cloud and aerosol extinction. The system is capable for day- and nighttime operation, except for the Raman channels.

To detect clouds in the upper troposphere, the backscattered light is analyzed with respect to peaks that result from enhanced backscattering from cloud particles. Every atmospheric feature is included in the analysis, which creates a significant enhancement in the backscatter signal according to the following definition:

$$S(h) = \frac{d}{dh}\frac{P(h)}{P_{Ray}(h)} > 3s \qquad (1)$$

where P(h) is the measured lidar backscatter signal and $P_{Ray}(h)$ is a simulated lidar signal from a purely molecular atmosphere. σ is the standard deviation of S(h) calculated from Poisson-statistics of the signal count rates. The cloud base is the first altitude starting from 4 km that satisfies criterion (1). The cloud top height is defined as the altitude where S(h) is back to zero and the integral of S(h) is greater than zero. Whether every feature that creates such a signal is a cloud in the traditional meaning of this word needs to be discussed, however, here we call these atmospheric features clouds. Since our definition is based on the increasing slope of the backscatter signal instead of the total cloud backscatter, there is no lower detection limit in terms of the optical depth. In fact, this method is very sensitive and thin cloud with an optical depth of 10^{-3} can easily be detected in simulations. When using the perpendicular channel as P(h) in eq. (1), the sensitivity of this method is even increased by about a factor of 10 in the case of depolarizing clouds like cirrus.

Besides cloud base and top height the optical depth, the depolarization and wavelengths dependence of the backscatter coefficient (color index) of the cloud can be inferred from the lidar data. Our analysis is based on the mean value of these quantities taken over one cloud layer as defined by the definition given above.

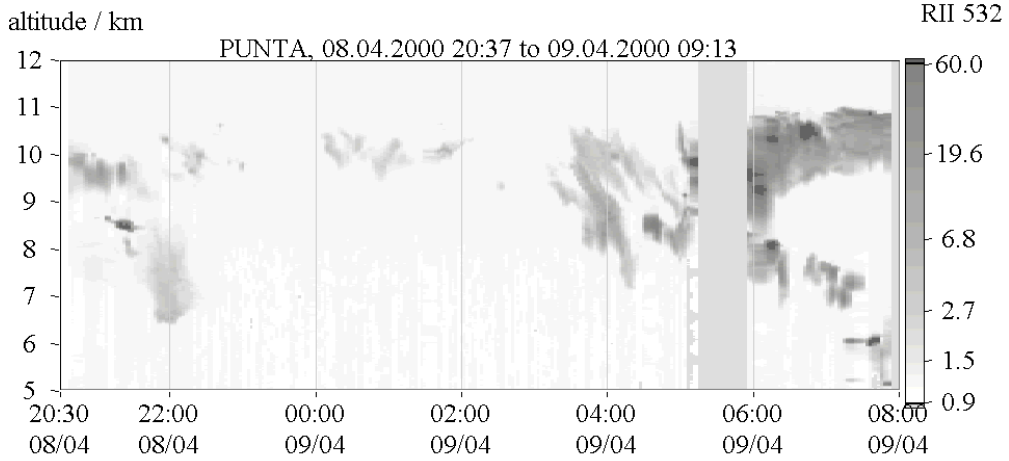

Figure 1. Lidar measurements of cirrus clouds in Punta Arenas on April 4th 2000. Plotted is the backscatter ratio as a function of time (UT) and altitude. Between 00:00 and 02:00 thin, subvisual cirrus were detected, at an altitude of around 10 km.

3 RESULTS

The ability of our lidar system to detect very thin clouds allow to study the properties of these so-called subvisual cirrus (Sassen et al., 1989) in comparison with visible cirrus clouds. It has been reported earlier (Immler and Schrems, 2002), that during both campaigns a considerable part of subvisual cirrus have been detected. In both, northern (NH) and the southern hemispheric (SH) campaigns, about 35% of the total detected clouds were subvisual.
The 'color' in terms of the color index

$$CI = \frac{\ln(b_{532})}{\ln(b_{355})} \cdot \frac{\ln(355)}{\ln(532)} \qquad (2)$$

of this thin clouds is predominantly close to zero independent of the optical depth and the location of the campaign (Fig.2). This indicates that the particles of the detected cloud layers are rather large ($r_{eff} > 3$ µm) and give the cloud a white color. This could be understood as a good definition for cirrus clouds from the lidar perspective, since most aerosol types have a color index greater than 0.5

with the exception of Saharan dust, which exhibits a color index clearly below zero (Sasano and Browell, 1989). Together with the depolarization data (Fig. 2b) our data suggest that the great majority of the particle layers detected by the lidar in the upper troposphere are ice clouds, including those with an optical depth in the subvisual range.

The tendency towards higher values of the color index in the SH data (Punta Arenas) of Fig. 2a might be caused by the orography of the site where a mountain range to the west regularly induced lee waves in which cirrus were formed. The larger vertical wind speed within the lee-waves generates smaller cirrus particles (Gayet et al., 2002).

The depolarization that was measured in Punta Arenas tended to be larger than the one measured in Prestwick. This discrepancy between the NH and the SH data of the depolarization behavior is higher in the subvisual range. Since the color index and the depolarization are in general anti-correlated the highly depolarizing clouds refer to another fraction of the observed clouds than the ones with the large color index discussed above. These clouds have zero or slightly negative color indices.

For clouds in the visible range, the optical depth can be calculated directly from the lidar signals. Provided that the lidar ratio, i.e. the ratio between the extinction and the backscatter coefficient is constant throughout the cloud, this measurement allows the determination of the lidar ratio. The results are shown in Figure 3. In the NH the measured lidar ratios at 532 nm form a rather narrow distribution around 21 sr with a standard deviation of 7 sr. Values above 30 sr are rarely measured. This is different in the southern hemispheric where about 50% of the data are values above 30 sr.

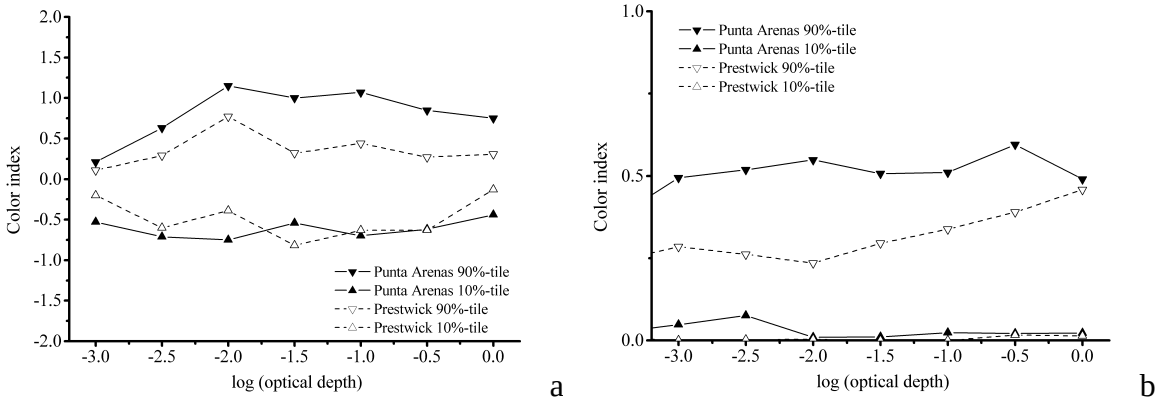

Figure 2. 10% and 90% quantiles of the color index and the depolarization (right) as a function of the optical depth

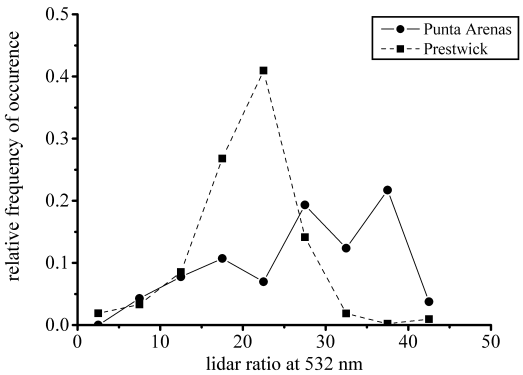

Figure 3. Relative frequency of occurrence of the lidar ratio of cirrus clouds determined with the lidar at the NH and SH locations.

4 CONCLUSIONS

The interpretation of lidar data of cirrus clouds in terms of properties of the cloud particles is not a straight forward task. Not only is the theoretical treatment of the scattering process difficult and time consuming, it is furthermore complicated by the fact that cirrus can contain particles of various sizes and shapes. However, an interesting approach has recently been developed by Reichardt et al. (2002) who uses the ray tracing technique to interpret the correlations of the depolarization and lidar ratio that were found in their measurements. It is shown that hexagonal columns depolarize more than plates while the lidar ratio is primarily a function of the aspect ratio (= length divided by width of the particle), particles with a stronger asphericity show a higher lidar ratio. While small particles tend to have an aspect ratio close to one, the aspect ratio will commonly differ significantly from unity for large particles. Thus, the lidar ratio is associated with particle size.

Based on this considerations, one may conclude from the lidar ratios measured in our study (Fig.3) that the particles of the clouds in the SH, visible and subvisible, tend to be larger and therefore have a higher lidar ratio, than the ones measured in the NH. Furthermore, the depolarization indicates a higher share of column-like particles in the southern hemisphere, while the northern hemispheric cirrus seem to be dominated by plates. This is most clearly the case for subvisual cirrus since in the SH, where a significantly larger fraction of subvisual clouds show high depolarization than in the NH (Fig. 2b).

However, it has to be noted that the extraction of microphysical information from lidar data is an underdetermined problem and that other explanations based on different types of particles are conceivable and could lead to different conclusions. Also, the limited size of our data base restricts our ability to draw general conclusions for cirrus properties in the northern and the southern hemisphere. One thing however that is save to conclude is, that there is a large natural variability in cirrus properties in both, northern and southern hemisphere, which is expressed by the wide range of optical depth and depolarization ratios of cirrus clouds determined by the lidar.

A detailed study of contrails and cirrus in the midlatitudes is currently being conducted with our lidar in Lindenberg (near Berlin/Germany), where radiosondes and sky cameras allow for a detailed characterization of the clouds and the meteorological condition under which they appear.

ACKNOWLEDGEMENT

Financial support by the Helmholtz Association through the “HGF Strategiefondsprojekt PAZI” is gratefully acknowledged.

REFERENCES

Gayet J.-F., F. Auriol, F. Immler, O. Schrems, A. Minikin, A. Petzold, J. Ovarlez, J. Ström, 2002, Microphysical and optical properties of wave cirrus cloud sampled during the INCA experiment., AMS Proceedings of the 11th conference on cloud physics

Immler F. and O. Schrems, 2002: Lidar measurements of cirrus clouds in the northern and southern hemisphere during INCA (55°N, 53°S): A comparative study Geophys. Res. Lett., 29, 16, 10.1029/2002GL015077, pp. 56-1 to 56-4

Reichardt J., Reichardt S., Hess M., McGee T.J., 2002: Correlations among the optical properties fo cirrus-cloud particels: Microphysical interpretation J. Geophys. Res., 107, D21, 10.1029/2002JD002589, pp. 4562-4574

Sasano Y., Browell E.V., 1989, Light scattering chracteristics of varoius aerosol types derived from multiple wavelength lidar observations., Appl. Opt., 28(9), pp. 1670-1674

Sassen K., M.K. Griffin, G.C. Dodd, 1989: Optical scattering and microphysical properties of subvisual cirrus clouds, and climatic implications J. Appl. Meteor., pp. 91-98

A Fast Stratospheric Aerosol Microphysical Model

S. Tripathi*, X. Vancassel, R. Grainger
Atmospheric, Oceanic and Planetary Physics, Department of Physics, University of Oxford, United Kingdom

H. Rogers
Department of Chemistry, Cambridge University, United Kingdom

Keywords: stratospheric aerosol, modelling, particles

ABSTRACT: A fast Stratospheric Aerosol Microphysical Model (SAMM) has been developed to study aerosol behaviour in the lower stratosphere. This model simulates homogeneous binary nucleation, condensational growth, coagulation and sedimentation of sulphuric acid-water particles, in order to predict the composition and the size-distribution of stratospheric aerosols. The principal advantage of SAMM is that it is non-iterative. This feature allows high computational efficiency, which is essential as SAMM will be included in the global chemical transport model SLIMCAT. SAMM has been used to simulate background stratospheric aerosols and volcanically disturbed aerosol (not presented here), and has been shown to be in good agreement with observations and other modelling studies.

1 INTRODUCTION

Stratospheric aerosols can affect the global climate system in a variety of ways. These aerosols play a significant role in the Earth's radiative balance (Lacis et al., 1992) and in the attenuation of UV radiation (Michaelangeli et al., 1992). They also provide a surface for heterogeneous chemical reactions, which are important for ozone loss in the middle atmosphere (Hoffman and Solomon, 1989; Rodriguez et al., 1991). The magnitude of these effects is significantly enhanced when the background aerosol layer is perturbed by strong volcanic eruptions, or possibly by high-speed civil transport aircraft (Tie et al., 1994; Weisentein et al., 1997; Bekki and Pyle, 1992; Pitari et al, 1993). Stratospheric aerosols are mainly composed of supercooled sulphuric acid droplets (Steele and Hamill, 1981). The sulphuric acid fraction of the droplets, which is in the range of 50-80 %, is a strong function of the relative humidity and the ambient temperature (Steele and Hamill, 1981), and therefore varies with latitude and season. Several models have been developed to understand the role of stratospheric aerosols in the atmospheric system (e.g. Turco et al., 1979; Toon et al., 1988). In recent years, studies have been performed where aerosol microphysics has been added to the existing 2-D and 3-D models. One of the rare studies of 3-D simulations of the formation and development of stratospheric aerosols is for instance reported by Timmreck (2001) who the emphasized the evolution and seasonal variation of stratospheric aerosols using the Hamburg climate model ECHAM4. There is a need for 3-D simulations of the effects of aircraft emissions on background stratospheric aerosols, including radiative and chemistry effects. Global studies are important because of the complex interactions between radiation, transport, chemistry and aerosol microphysics. This paper briefly describes SAMM, a box model of sulphuric acid-water aerosols.

Many microphysical models are based on iterative solutions. Computer processing time and memory use is an important issue in global simulations of atmospheric processes. Keeping this in mind, non-iterative solutions to growth and coagulation equations have been used in SAMM. These techniques have been developed by Jacobson et al. (1994, 1995, 1999, 2002).

* *Corresponding author:* Sachchida Tripathi, Department of Civil Engineering, Indian Institute of Technology, Kanpur 208016, India. Email: snt@iitk.ac.in

2 MODEL DESCRIPTION

2.1 *Model overview*

A size bin structure has been used to distribute particles as a function of their acid content (e.g. Sorokin et al., 2001). In a given bin the evolution of particle concentration, N, is described by the following equation

$$\frac{dN}{dt} = \left[\frac{dN}{dt}\right]_{nuc} + \left[\frac{dN}{dt}\right]_{coag} + \left[\frac{dN}{dt}\right]_{cond} + \left[\frac{dN}{dt}\right]_{sed} \quad (1)$$

where the subscripts nuc, coag, and cond mean respectively nucleation, coagulation, condensation and evaporation of H_2O and H_2SO_4, and sed refers to sedimentation removal.

Particle formation has been achieved by a classical nucleation parameterization (Vehkamaki et al., 2002), which provides the rate of nucleation as well as the particle size and composition for a large range of temperature, sulphuric acid and water vapour concentrations.

Following Jacobson (2002), sulphuric acid condensation and nucleation have been treated as two competing mechanisms. This scheme provides, at each time step, the atmospheric concentration of the gas after condensation and the final H_2SO_4 concentration in the particles for any size bin, without using any iterative method. Particles have been assumed to achieve instantaneous equilibrium with water, as the rate of collision of water molecules is much higher than that of sulphuric acid (e.g. Steele and Hamill, 1981). Coagulation calculations have been carried out using the work of Jacobson et al.(1994), whose semi-implicit expression is computationally fast and numerically reliable, provided that the volume ratio between two adjacent bins remains rather small (e.g. Sorokin et al., 2001). Finally, particles have been removed from the system by sedimentation, using a very simple scheme. Particles fall velocities are calculated using expressions given by Pruppacher and Klett (1997). The main thermodynamic data (surface tension, density, activity) used to calculate fall velocities have been taken from Vehkamaki et al. (2002) in order to remain consistent with the nucleation scheme.

2.2 *Selection of Model Parameters*

We have performed several sensitivity studies to see the effects of the choice of number of size bins on predicted size distribution, and on the aerosol surface area. The aerosol surface area is an important parameter used to assess the impact of heterogeneous chemistry on the composition of the atmosphere. The lower and upper size particle radius limits adopted for SAMM are roughly 0.3 nm and 5 μm respectively. The upper size limit is based on the fact that in typical stratospheric conditions very few water-sulphuric acid particles become bigger than this size: those that do rapidly sediment from the atmosphere. The criterion for the lower size limit is set by the size of the newly formed particles due to nucleation. Figure 1 plots the background aerosol surface area as a function of the number of size bins used and the integration time-step for conditions typical of an altitude of 20 km. The calculated aerosol surface areas lie between 0.65 and 0.50 $\mu m^2/cm^3$. These values are comparable to those recommended for heterogeneous chemical reactions of atmospheric importance. Tie et al. (1994) reported a value of 0.6 $\mu m^2/cm^3$ for aerosol surface area at 20 km from their 2-D model calculations. It can be seen that little accuracy is gained by decreasing the model time step below about 2000 s. Therefore all the standard model runs used an 1800 s time-step (Figure 2) which generally corresponds to the integration time steps for dynamical processes used in global models. The influence of the size bins number on the aerosol surface area is not very high since using 20 or 70 bins leads only to a difference of approximately 10 %. However, the impact on the size distribution is larger, as already pointed out. A time step of 1800 s and a bin number of 44 was adopted for SAMM. Based on this evaluation, we expect computational errors < 0.005 %, 5 % and 40 % in the volume, surface area and number density respectively. These results should be kept in mind while examining results involving number densities or size ratios, as SAMM could overestimate the density of larger particles. However, using 44 bins provides reliable surface areas results.

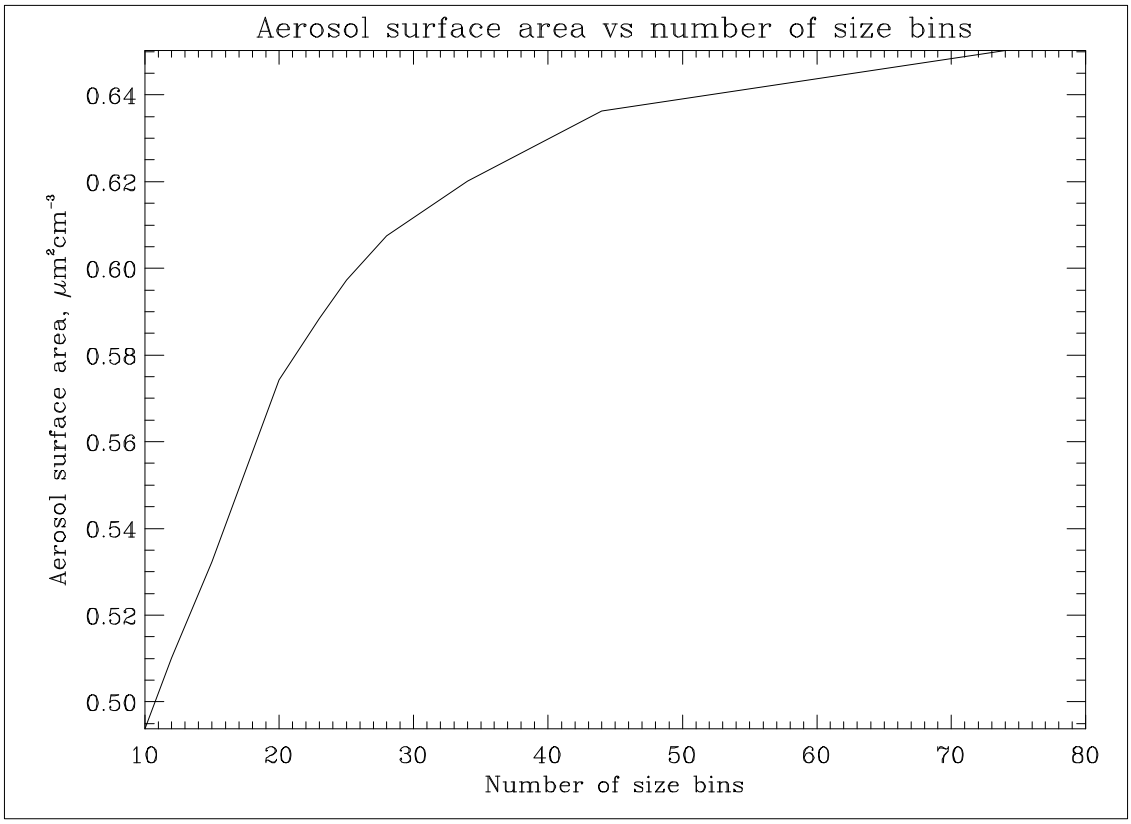

Figure 1. Aerosol surface area plotted as a function of the number of size bins used and the integration time step.

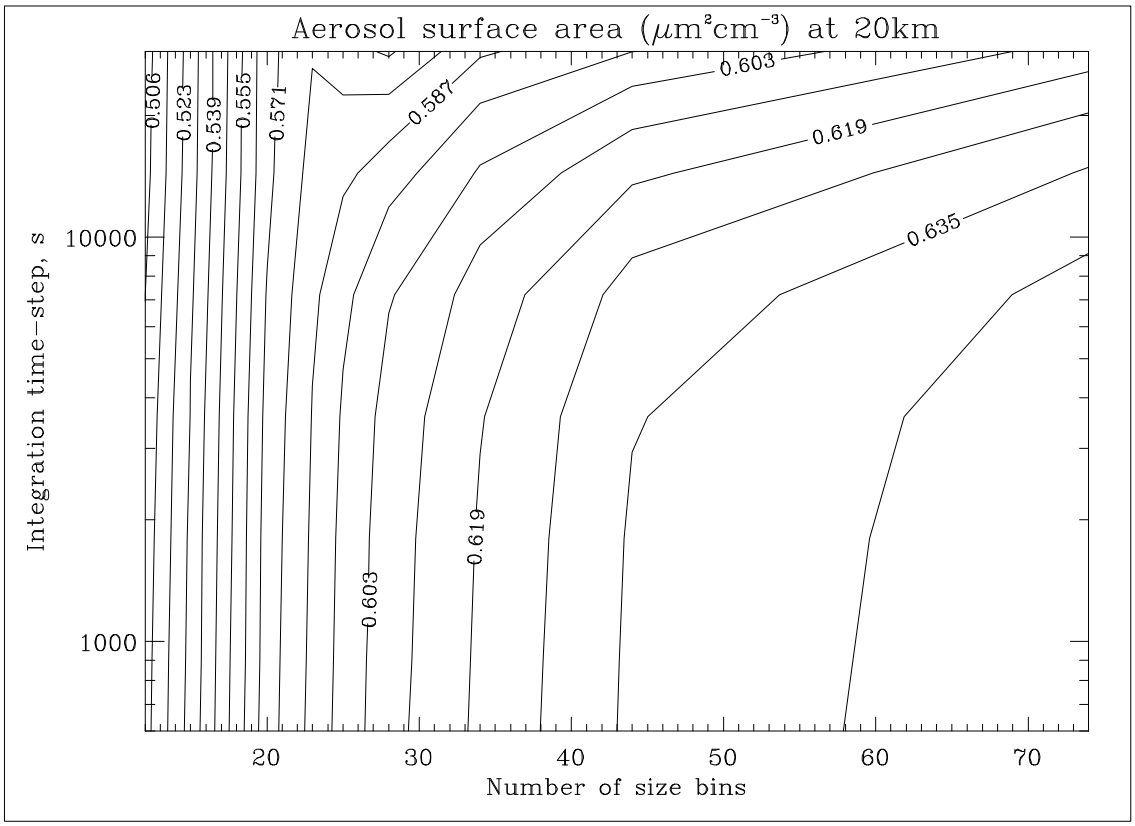

Figure 2. Aerosol surface area as a function of the number size bins used for an 1800 s time step.

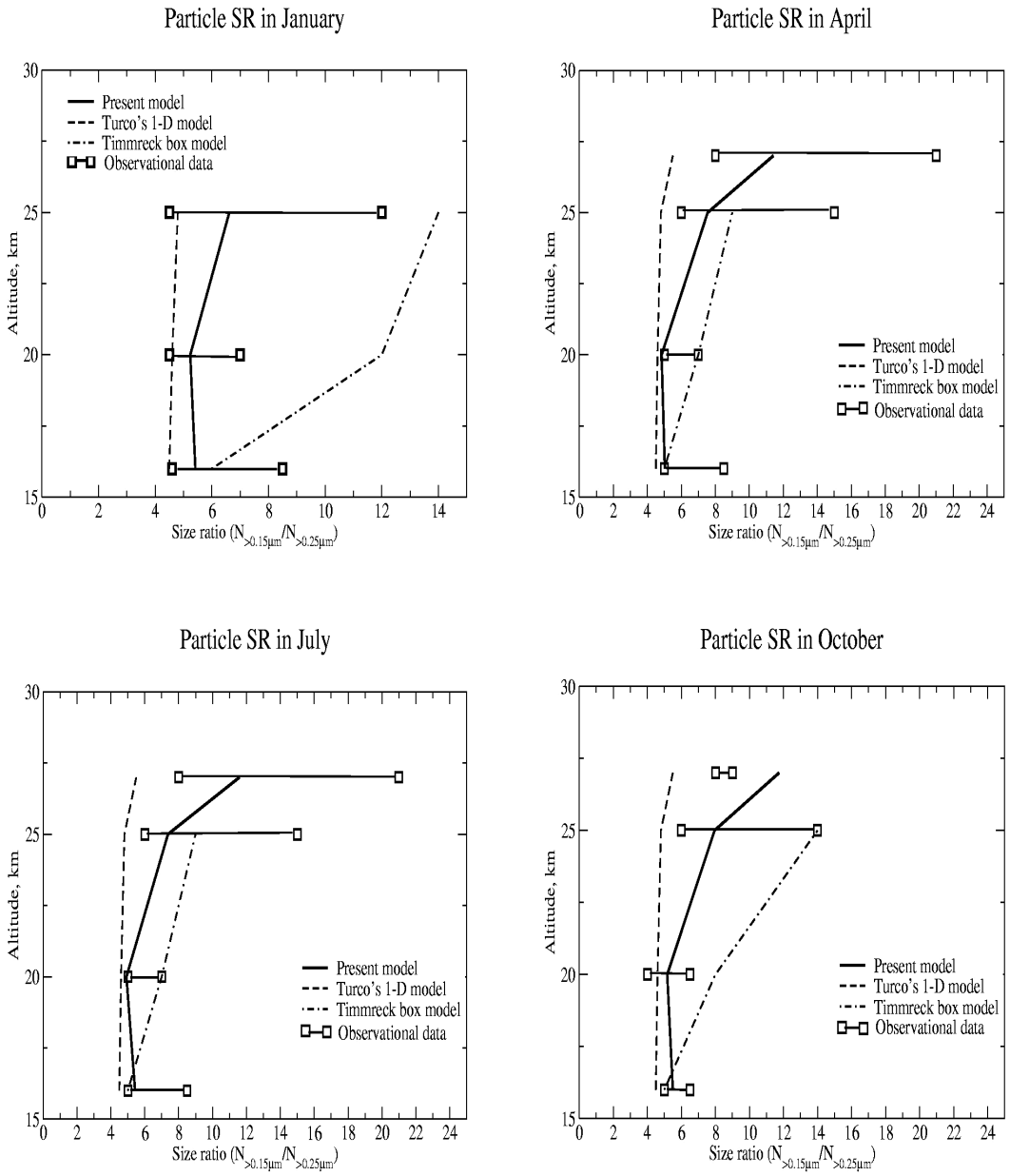

Figure 3. Numerical values of particle size ratio (SR) as a function of altitude for different seasonal conditions.

3 RESULTS

Figure 3 shows model-simulated aerosol mixing ratios together with observed values from Hofmann and Rosen (1981). SAMM compares well with observations and especially, it is able to reproduce the trends of particles size ratios as a function of altitude.

However, in January the altitude at which the maximum occurs is different from that predicted by Turco's model. Errors on number densities are high due to the effect of numerical diffusion and also to the absence of diffusion. This last process is, with sedimentation, responsible for the vertical transport of particles and was not included in these box model simulations Comparing the plots in Figure 3, we do not see large seasonal variations in the aerosol mixing ratio; this is consistent with the earlier 1-D (Toon et al., 1979) and 0-D (Timmreck and Graph, 2000) model predictions. Furthermore, the total number concentration of particles is always between 4 and 8 cm^{-3}, which falls within the range reported by Weisenstein et al. (1997) who studied the stratospheric aerosols using a two-dimensional model.

4 CONCLUSION

A fast stratosphere aerosol microphysical model (SAMM) has been developed suitable for use in large 3-D global models. SAMM is able to provide accurate estimates of aerosol surface area using a small number of particle size bins. Besides the total surface area, the model is able to reproduce aerosol number concentration trends observed in the stratosphere. Future work will include extending SAMM to include processes involving ions and extend the treatment of aerosol composition to include multicomponent solutions. The inclusion of SAMM in a global model (SLIMCAT) will be the first step in assessing the impact of aircraft aerosol emissions in the lower stratosphere using the 3D model.

5 ACKNOWLEDGEMENTS

The authors acknowledge funding of this work by a NERC UTLS Ozone Grant. The authors would also like to thank H. Vehkamaki for providing them her nucleation scheme and for helpful discussions.

REFERENCES

Bekki, S., and J. A. Pyle, 1992: Two-dimensional assessment of the impact of aircraft sulphur emissions on the stratospheric sulphate aerosol layer. *J. Geophys. Res.* 97, 15839-15847.

Hofmann, D.J., and J.M. Rosen, 1981: On the background aerosol layer. *J. Atmos. Sci.* 32, 1446-1456.

Hofmann, D. J., and S. Solomon, 1989: Ozone destruction through heterogeneous chemistry following the eruptions of El Chichón. *J. Geophys. Res.* 94, 5029-5041.

Jacobson, M. Z., R. P. Turco, E. J. Jensen, and O. B. Toon, 1994: Modelling coagulation among particles of different composition and size. *Atmos. Environ.* 28, 1327-1328.

Jacobson, M. Z., 1995: Numerical techniques to solve condensational and dissolutional growth equations when growth is coupled to reversible reactions, *Aerosol Sci. Technol.* 27, 491-498.

Jacobson, M.Z., and R. C. Turco, 1995: Simulating condensational growth, evaporation, and coagulation of aerosols using moving and stationary size grid. *Aerosol Sci Technol.* 22, 73-92.

Jacobson, M. Z., 1999: *Fundamentals of Atmospheric Modelling*, Cambridge University Press, Cambridge, UK.

Jacobson, M. Z., 2002: Analysis of aerosol interactions with numerical techniques for solving coagulation, nucleation, condensation, dissolution, and reversible chemistry among multiple size distributions. *J. Geophys. Res.* vol. 107, 4366, doi: 10.1029/2001JD002044.

Lacis, A., J. Hansen, and M. Sato, 1992: Climate forcing by stratospheric aerosols. *Geophys. Res. Lett.* 19, 1607-1610.

Michaelangeli, D., M. Allen, Y. L. Yung, R. L. Shia, D. Crisp, and J. Eluszkiewicz, 1992: Enhancement of atmospheric radiation by an aerosol layer. *J. Geophys. Res.* 97, 865-974.

Pitari, G., V. Rizi, L. Ricciardulli, and G. Visconti, 1993: High-speed civil transport impact: Role of sulphate, nitric acid trihydrate, and ice aerosols studied with a two-dimensional model including aerosol physics. *J. Geophys. Res.* 98, 23141-23164.

Pruppacher, H. R., and J. D. Klett, 1997: *Microphysics of clouds and precipitation*, 2nd rev. and enl. ed. Kluwer Academic Publishers, Dordrecht.

Rodriguez, J. M., M. K. W. Ko, and N. D. Sze, 1991: Role of heterogeneous conversion of N_2O_5 on sulphate aerosols in global ozone losses, *Nature*, 352, 134-137.

Rosen, J. M., D. J. Hofmann, and J. Laby, 1975: Stratospheric aerosol measurements II. The worldwide distribution. *J. Atmos. Sci.* 32, 1457-1462.

Russell, P. B., and P. Hamill, 1984: Spatial variation of stratospheric aerosol acidity and model refractive-index-implications of recent results. *J. Atmos. Sci.* 41, 1781-1984.

Sorokin A., X. Vancassel, and P. Mirabel, 2001: On volatile particle formation in aircraft exhaust plumes. *Phys. Chem. Earth* 26, 557-561.

Steele, H. M., and P Hamill, 1981: Effects of temperature and humidity on the growth and optical properties of sulphuric acid-water droplets in the stratosphere. *J. Aerosol Sci.* 12, 517-528.

Tie, X., L. Lin, and G. Brasseur, 1994: Two-dimensional coupled dynamical/chemical/microphysical simulations of global distribution of El Chichón volcanic aerosols. *J. Geophys. Res.* 99, 16779-16792.

Timmreck, C., and H. F. Graph, 2000: A microphysical model for simulation of stratospheric aerosol in a climate model. *Meteorologische Zeitschrift* 9, 263-282.

Timmreck, C, 2001: Three-dimensional simulations of stratospheric background aerosol: First results of a multiannual GCM simulation. *J. Geophys. Res.* 106, 28313-28332.

Toon, O. B., R. P. Turco, P. Hamill, C. S. Kiang, and R. C. Whitten, 1979: A one-dimensional model describing aerosol formation and evolution in the stratosphere: II, Sensitivity studies and comparison with observations. *J. Atmos Sci.* 36,718-736.

Toon, O. B., R. P. Turco, D. Westphal, R. Malone, and M. S. Liu, 1988: A multidimensional model for aerosols: Description of computational analogs. *J. Atmos. Sci.* 45, 2123-2143.

Toon, O.B., R. P. Turco, J. Jordon, J. Goodman, and G. Ferry, 1989: Physical processes in Polar Stratospheric Clouds. *J. Geophys. Res.* 94, 11359-11380.

Turco, R. P., P. Hamill, O. B. Toon, R. C. Whitten, and C. S. Kiang, 1979: A one-dimensional model describing aerosol formation and evolution in the stratosphere. Physical processes and mathematical analogs. *J. Atmos Sci.* 36, 699-717.

Vehkamaki, H., M. Kulmala, I. Napari, K.E.J Lehtinen, C. Timmreck, M.Noppel, and A. Laaksonen, 2002: An improved parameterisation for sulphuric acid/water nucleation rates for tropospheric and stratospheric conditions. *J. Geophys. Res*. 107, doi: 10.1029/2001GL013813.

Weisenstein, D. K., P. K. Yue, G. K. W. Ko, N. D. Sze, J. M. Rodriguez, and C. J. Scott, 1997: Two-dimensional model of sulphur species and aerosol. *J. Geophys. Res.* 102, 13019-13053.